



SAPIENZA
UNIVERSITÀ DI ROMA

Structural vibration energy harvesting via bistable nonlinear attachments

Sandra Chiacchiari

March, 2018

Dissertation submitted in partial fulfillment of the requirements for the degree of

Doctor of Philosophy

in

Engineering of Structures

XXX cycle

Advisor

Prof. Francesco Romeo

Co-advisor

Prof. Alexander Vakakis

Doctoral Coordinator

Prof. Franco Bontempi



Structural vibration energy harvesting via bistable nonlinear attachments

Sandra Chiacchiari

Rome, March 2018

Keywords: energy harvesting; bistability; negative stiffness; nonlinear dynamics;
low-energy impacts

Dissertation submitted in partial fulfilment of the requirements for the degree of
Doctor of Philosophy in Engineering of Structures

Dottorato di ricerca in Ingegneria delle Strutture XXX ciclo

Dipartimento di Ingegneria Strutturale e Geotecnica

Facoltà di Ingegneria Civile e Industriale

© Sapienza Università di Roma

Via Eudossiana 18, 00184 Roma, Italy

To my family

Abstract

A vibration-based bistable electromagnetic energy harvester coupled to a directly excited host structure is theoretically and experimentally examined. The primary goal of the study is to investigate the potential benefit of the bistable element for harvesting broadband and low-amplitude vibration energy. The considered system consists of a grounded, weakly damped, linear oscillator (LO) coupled to a light-weight, damped oscillator by means of an element which provides for both cubic nonlinear and negative linear stiffness components and electromechanical coupling elements. Single and repeated impulses with varying amplitude applied to the LO are the vibration energy sources considered. A thorough sensitivity analysis of the system's key parameters provides design insights for a bistable nonlinear energy harvesting (BNEH) device able to attain robust harvesting efficiency. Energy localization into the bistable attachment is achieved through the exploitation of three BNEH main dynamical regimes; namely, periodic cross-well, aperiodic (chaotic) cross-well, and in-well oscillations.

For the experimental investigation on the performance of the bistable device, nonlinear and negative linear terms in the mechanical coupling are physically realized by exploiting the transverse displacement of a buckled slender steel beam; the electromechanical coupling is accomplished by an electromagnetic transducer.

Sommario

La tesi presenta lo studio teorico e sperimentale di un sistema di recupero di energia di tipo bistabile, accoppiato a una struttura ospitante direttamente sollecitata da eccitazione di tipo impulsivo. Il principale obiettivo è indagare il potenziale beneficio offerto dall'elemento bistabile nel recuperare energia vibrazionale su un'ampia banda di intensità dell'eccitazione, ivi compresi bassi livelli energetici, per i quali analoghi sistemi monostabili perdono la loro efficienza. Il sistema oggetto di studio è composto da un sistema primario lineare debolmente smorzato e una massa ausiliaria accoppiata meccanicamente e elettricamente al primo. L'accoppiamento meccanico, fisicamente realizzato mediante una trave in buckling, dà origine a un termine di rigidità cubica e un termine di rigidità lineare negativa; l'accoppiamento elettromeccanico assume un meccanismo di trasduzione ad induzione elettromagnetica. L'esame di un sistema ottimale, risultato da un'estesa analisi di sensitività, ha permesso di individuare i principali regimi dinamici favorevoli alla localizzazione dell'energia nel sistema ausiliario e conseguente efficiente racimolazione dell'energia stessa.

Acknowledgments

I would like to express my sincere gratitude to my advisor, Prof. Francesco Romeo, for having been an insightful guidance in this research work, for his continuous support, motivation and professional advice, for widening my view from various perspectives and giving me the key for the correct interpretation of physical phenomena. I could not have wished for a better mentor.

A special thanks goes to Prof. Achille Paolone, who has believed in me since the beginning of this path, for giving always priceless and wise advices.

I am extremely grateful to Profs. Alexander Vakakis, Lawrence Bergman and Michael McFarland, for having welcomed me at the University of Urbana-Champaign and having given to me their precious help. Besides, I will not forget laughs and time spent in the Mechanical Engineering Laboratory trying to fix things up.

A "thank you" will never be enough to express the gratitude to my beautiful family, for being always my strength, for encouraging me and for helping me in directing my steps in the right direction. And to the Zullo's, for being part of my life as a second family. I love you all to the moon and back.

Last but not least, to all my friends, near and distant, and colleagues, who offered me, each in his own way, everlasting smiles, uncontrollable laughter, infinite support and confidence, when times got rough, and critiques, to force me to challenge my own thinking. For these reasons and more, thank you.

Sandra

Contents

Sommario - Abstract	I
Acknowledgments	III
Table of contents	V
List of figures	IX
List of tables	XXI
1 Introduction	1
1.1 Research framework	1
1.2 Aim and scope	5
1.3 Thesis outline	7
2 State of the art	9
2.1 General overview on vibration energy harvesting	9
2.2 Suitable dynamic regimes	17
2.2.1 Energy harvesting via linear resonators	17
2.2.2 Adoption of nonlinear devices for energy harvesting purpose	23
2.2.3 Bistable solutions	27
2.3 Exploiting targeted energy transfer (TET)	33
2.4 Transduction mechanisms	40
2.4.1 Electrostatic energy harvesting	41

2.4.2	Piezoelectric energy harvesting	43
2.4.3	Electromagnetic energy harvesting	47
3	Model of the electromechanically coupled system	55
3.1	System modeling	55
3.2	Mechanical coupling modeling	57
3.2.1	Problem formulation and analytical solution of the clamped-clamped buckled beam	57
3.2.2	Single-mode approximation of the harvester's dynamics	64
3.3	Electromechanical coupling modeling	68
3.4	Governing equations and harvesting measures	71
4	Numerical investigation	79
4.1	Parametric analysis and optimization	79
4.2	Dynamic response of the optimal BNEH	85
4.3	Energy harvesting efficiency under repeated impulses	90
4.3.1	Periodic impulses scenario	90
4.3.2	Random impulses scenario	102
5	Experimental study	111
5.1	Experimental setup	111
5.2	Design and system identification	118
5.3	Results	126
5.3.1	Single impulse scenario	127
5.3.2	Repeated impulses scenario	132
6	Conclusion	137
6.1	Research summary and concluding remarks	137
6.2	Novel contributions	140
6.3	Future research	141

A Static analysis of the straight beam	143
B System response under repeated impacts	147
Bibliography	151

List of Figures

1.1	Block diagram of the energy harvesting process.	2
2.1	Example of wireless sensor network on a bridge.	11
2.2	Flux of information among the sensors grid and up to the end user.	12
2.3	A typical power consumption scenario of a sensor node. Since the consumption does not equally match the harvester output, an energy buffer and power management IC in between is necessary [1].	12
2.4	Power spectra of vibrations in three different environments [2, 3].	14
2.5	Time histories and spectra of different types of vibrations: (a) response to walking of a high-frequency floor bay [4]; (b) vibration of the slabs of a box-shaped deck due to train-induced noise in the cavity arising from vibrating bridge components [5]; (c) vertical displacement response to traffic flow of the deck of a cable-stayed bridge [6].	15
2.6	Pulse-like vibration profiles of railroad tracks [7].	17
2.7	Schematic of a linear inertial generator (a); piezoelectric linear cantilever beam (b).	18
2.8	Frequency spectrum of power generation around the resonance frequency of the generator for various damping factors. The arrows indicate the trend of the curves for increasing values of damping.	20

2.9	Ensemble of cantilever beams with proof masses at their tips (a) and transfer functions corresponding to the beam–mass systems (a) when the device functions as a band-pass filter (b).	22
2.10	Hardening behaviour of a nonlinear system.	25
2.11	Sketch of the NEH proposed by [8] (a); Experimental (markers) and theoretical (black line) of the velocity response for low (top) and high (bottom) excitation level (b).	26
2.12	Sketch of the NEH proposed by [9] (a); displacement and voltage response for a low (lighter line) and high (thicker line) excitation level for different values of d (b).	27
2.13	Double-well potential of a bistable oscillator showing example trajectories for in-well, chaotic cross-well and periodic cross-well oscillations.	28
2.14	Example of displacement response trajectories (top row) and phase plots with an overlaid Poincaré map as black circles (bottom row) for the three dynamic regimes of a BNEH: in-well oscillations (a), chaotic in-well and cross-well vibrations (b) and periodic cross-well oscillations (c) [10].	29
2.15	The von Mises structure, restoring force and potential function (left-hand side) and configurations at limit points (LPs) and equilibrium points (EPs) (right-hand side). EP1 and EP3 are stable, EP2 is unstable.	30
2.16	Drawing of a piezoelectric bistable cantilever beam with a tip magnet and one (a) or two (b) fixed magnets; experimental fixture of an electromagnetic cantilever beam with tip magnet by [11] (c).	31
2.17	FEP of the periodic orbits of the Hamiltonian system (impulsive orbits: (●), bifurcation points: (+) when four Floquet multipliers are equal to +1 and (○) when two Floquet multipliers are equal to +1 and two to −1) [12].	35

2.18	Close-ups of particular branches in the frequency index–logarithm of energy plane [12].	36
2.19	Percentage of impulsive energy eventually dissipated in the NES as a function of the magnitude of the impulse [13].	37
2.20	Percentage of impulsive energy dissipated in the NES as a function of the magnitude of the impulse, for varying negative stiffness (from [14]) Dashed line represents the monostable (purely cubic) system, whereas the thick solid line refers to the optimal value of the negative linear stiffness.	38
2.21	Poincaré sections of the bistable system investigated by [14]. Insets depict the displacement of the LO (blue) and BNES (red) of selected points on the Poincaré map.	40
2.22	Schematic of an electrostatic energy harvester.	42
2.23	Three types of electrostatic energy harvesters: In-Plane Overlap (a); In-Plane Gap Closing (b); Out-of-Plane Gap Closing (c).	42
2.24	Schematic of direct piezoelectric effect; (a) piezoelectric material, (b) voltage generation under tension, (c) voltage generation under compression [15].	44
2.25	Direct piezoelectric effect with 33 and 31 strain-charge coupling.	45
2.26	Schematic of bimorph piezoelectric cantilever beam.	46
2.27	Piezoelectric energy harvesting systems: (a) [16] substrate layer 0.26 cm^3 ; (b) [17] cantilever beam mass 0.20 g , tip mass 0.97 g ; (c) [18] mass 0.011 kg ; (d) [19] size $100 \times 40 \times 12 \text{ mm}$	48
2.28	Scheme of an electromagnetic energy harvester (a) and of the electromagnetic induction(b).	49
2.29	Two types of electromagnetic energy harvesters.	49
2.30	Normalized power density of some existing electromagnetic vibration energy harvesters [20].	51

2.31	Power versus scaling length L (solid line corresponds to the line of best fit for upper limit of power) [21].	51
2.32	Micro-fabricated square spiral coil.	52
2.33	Electromagnetic energy harvesting systems: (a) [22] mass 35.6 g; (b) [23] acceleration approx. 200 mg. (c) [24], maximum stay cable acceleration 100 – 200 mg.	53
3.1	Model of the two coupled oscillators.	56
3.2	Bifurcation diagram for the static deflection of the fixed–fixed beam at $x = 0.25$ with the axial load. P_1, P_2, P_3 are the first three critical loads.	60
3.3	Variation of the first four natural frequencies around the lowest three buckling shapes with the axial load (a) and around the first buckled configuration with the nondimensional buckling level . . .	63
3.4	Sketch of the buckled beam.	65
3.5	Potential energy surface of the coupled system.	73
3.6	Single impulse (a) and train of impulses of inter-arrival times Δt_p (b).	74
4.1	Contour plots for efficiency measure $\eta\%$ resulting from the application of a single impulse to the primary linear system, evaluated at $\tau = 60$ as a function of ξ and \tilde{I}_0 . Parameters are $\beta = 0.1$, $\lambda = 0.001$, $\zeta = 0.02$: (a) $\mu = 0.2$; (b) $\mu = 0.05$; regions I, II and III refer to different dynamic behaviours as discussed in the text.	80
4.2	Contour plots for the efficiency measure $\eta\%$ resulting from the application of a single impulse to the primary linear system, evaluated at $\tau = 60$ as a function of the negative stiffness parameter ξ and the mass ratio μ . Parameters are $\beta = 0.1$, $\lambda = 0.001$, $\zeta = 0.02$: (a) $\tilde{I}_0 = 0.45$; (b) $\tilde{I}_0 = 0.25$; (c) $\tilde{I}_0 = 0.09$	82

4.3	Contour plots of the efficiency measure $\eta\%$ resulting from the application of a single impulse to the primary linear system, harvested up to time $\tau = 60$, as a function of the inherent viscous damping of the coupling ζ and the amplitude of the initial velocity \tilde{I}_0 . Parameters are $\beta = 0.1$, $\lambda = 0.001$, $\mu = 0.04$: (a) monostable configuration ($\xi = 0.0$); (b) bistable configuration ($\xi = -0.6$); regions I, II and III refer to the same regions of Figure 4.1.	83
4.4	Contour plots of the efficiency measure $\eta\%$ resulting from the application of a single impulse to the primary linear system, evaluated at $\tau = 60$ as a function of the electromechanical coupling parameter ζ and the amplitude of the initial velocity I_0 . Parameters are $\lambda = 0.001$, $\zeta = 0.02$, $\mu = 0.04$: (a) monostable configuration ($\xi = 0.0$); (b) bistable configuration ($\xi = -0.6$); regions I, II and III refer to the same regions of Figure 4.1.	85
4.5	Transient dynamics of the two-DOF system for the high input energy level ($I_0 = 0.16$ m/s): time histories of the linear oscillator (a) and harvester (b) responses (dashed lines represent the two equilibrium positions); (d) and (e) corresponding wavelet transform spectra; (c) percentage of instantaneous total energy in the BNEH; (f) percentage of total energy harvested by the BNEH (the dotted-dashed line represents the same quantity for the analogous monostable NEH).	87
4.6	Transient dynamics of the two-DOF system for the intermediate input energy level ($I_0 = 0.09$ m/s): time histories of linear oscillator (a) and harvester (b) responses (dashed lines represent the two equilibrium positions); (d) and (e) corresponding wavelet transform spectra; (c) percentage of instantaneous total energy in the BNEH; (f) percentage of total energy harvested by the BNEH (the dotted-dashed line represents the same quantity for the analogous monostable NEH).	88

4.7	Transient dynamics of the two-DOF system for the low input energy level ($I_0 = 0.03 \text{ m/s}$): time histories of linear oscillator (a) and harvester (b) responses (dashed lines represent the two equilibrium positions); (d) and (e) corresponding wavelet transform spectra; (c) percentage of instantaneous total energy in the BNEH; (f) percentage of total energy harvested by the BNEH (the dotted-dashed line represents the same quantity for the analogous monostable NEH).	89
4.8	Transient dynamics of the two-DOF system in its monostable configuration, for the intermediate input energy level ($I_0 = 0.09 \text{ m/s}$): time-histories of linear oscillator (a) and harvester (b) responses; (d) and (e) corresponding wavelet transform spectra; (c) percentage of instantaneous total energy in the NEH; (f) percentage of total energy harvested by the NEH	90
4.9	Contour plots of the total energy harvested E_h as a function of the impulse period μ_T and the amplitude of the initial velocity I_0 , measured after (a) 1, (b) 3, (c) 10 and (d) 20 impulses.	91
4.10	Contour plots of the efficiency $\eta_{\%}$ as a function of the impulse period μ_T and the amplitude of the initial velocity I_0 , measured after measured after (a) 1, (b) 3, (c) 10 and (d) 20 impulses.	93
4.11	Average energy harvested \bar{E}_h in mJ and energy harvesting efficiency $\bar{\eta}_{\%}$ as a function of the impulse period μ_T , computed for 600 impulses. (a),(b) $I_0 = 0.16 \text{ m/s}$; (c),(d) $I_0 = 0.09 \text{ m/s}$; (e),(f) $I_0 = 0.03 \text{ m/s}$. Comparison with the monostable configuration (dashed lines).	94
4.12	Displacement time history of LO (a) and BNEH (b); percentage of instantaneous total energy in the BNEH (c) and total energy harvested (d) for $I_0 = 0.09 \text{ m/s}$ and $\mu_T = 32$. Number of impulses: 10. Dashed lines represent the two equilibrium positions.	96

4.13	Bistable system response for $I_0 = 0.03 \text{ m/s}$ and $\mu_T = 2$: displacement time history of LO (a) and BNEH (b); percentage of instantaneous total energy in the BNEH (c) and total energy harvested (d). Number of impulses: 25. Dashed lines represent the two equilibrium positions.	98
4.14	Monostable system response for $I_0 = 0.03 \text{ m/s}$ and $\mu_T = 2$: displacement time history of LO (a) and monostable NEH (b); percentage of instantaneous total energy in the NEH (c) and total energy harvested (d). Number of impulses: 25.	99
4.15	Bistable system response for $I_0 = 0.03 \text{ m/s}$ and $\mu_T = 3.7$: displacement time history of LO (a) and NEH (b); percentage of instantaneous total energy in the BNEH (c) and total energy harvested (d). Number of impulses: 25. Dashed lines represent the two equilibrium positions.	100
4.16	Monostable system response for $I_0 = 0.03 \text{ m/s}$ and $\mu_T = 3.7$: displacement time history of LO (a) and NEH (b); percentage of instantaneous total energy in the NEH (c) and total energy harvested (d). Number of impulses: 25.	101
4.17	Bistable system response for $I_0 = 0.03 \text{ m/s}$ and $\mu_T = 4$: displacement time history of LO (a) and BNEH (b); percentage of instantaneous total energy in the BNEH (c) and total energy harvested (d). Number of impulses: 25. Dashed lines represent the two equilibrium positions.	103
4.18	Monostable system response for $I_0 = 0.03 \text{ m/s}$ and $\mu_T = 4$: displacement time history of LO (a) and NEH (b); percentage of instantaneous total energy in the NEH (c) and total energy harvested (d). Number of impulses: 25.	104

4.19	Exponential distribution for the waiting times $\mu_T = 6$, $\mu_X = \sigma_X = 0.07$ (a) and Rayleigh distribution for the impulse amplitudes: $N = 1000$, $\mu_R = 0.07$, $b = 0.06$ (b).	106
4.20	Random pulse train as Poisson process, with Rayleigh distributed magnitudes: $\bar{I}_0 = 0.07$ m/s, $\mu_T = 6$	106
4.21	Average energy harvested \bar{E}_h in mJ and energy harvesting efficiency $\bar{\eta}\%$ as a function of the impulse period μ_T , computed for 600 impulses. (a),(b) $\bar{I}_0 = 0.16$ m/s; (c),(d) $\bar{I}_0 = 0.09$ m/s; (e),(f) $\bar{I}_0 = 0.03$ m/s. Comparison with the monostable configuration (dashed lines) and with the periodic case for the bistable configuration (blue lines). . .	108
4.22	Average energy harvested \bar{E}_h in mJ and energy harvesting efficiency $\bar{\eta}\%$ as a function of the average impulse period $\bar{\mu}_T$, computed for 600 impulses. (a),(b) $I_0 = 0.16$ m/s; (c),(d) $I_0 = 0.09$ m/s; (e),(f) $I_0 = 0.03$ m/s. Comparison with the monostable configuration (dashed lines).	110
5.1	Photograph of the experimental apparatus of the energy harvesting system (top view in (b)).	112
5.2	Photograph of the beam support (a) and sketch of the coupled harvesting device (b).	113
5.3	Photographs of the electrical circuit.	114
5.4	Change of magnetic flux concatenated to the circuit.	115
5.5	Output voltage as a function of the position of the coil relative to the magnet.	116
5.6	Block diagram of the instrumentation.	116
5.7	Set-up of the experimental test.	117
5.8	Linear oscillator design and subsequent identification.	119
5.9	RFS approximation \tilde{G}_{RF} to the experimental data (blue dots) for the linear system.	120

5.10	State-variable plot for the linear system. Blue line: experimental data, red line: computed restoring force.	120
5.11	Technical drawing of the support.	122
5.12	Fitting of experimental response time-histories and corresponding FFTs. Black line: experiment, red line: numerical model	123
5.13	Configuration of the beam at the end of the first step (i.e. second step starting configuration).	124
5.14	Bifurcation curve for the beam with imperfection.	124
5.15	Polynomial fitting (blue line) of the force-displacement curve (red dotted line) of the buckled beam (Abaqus)	124
5.16	Series of deformed shapes during snap-through	125
5.17	Total energy harvested as a function of the electro-mechanically induced damping, with $k_e = 11 \text{ T m}$ and $R_c = 32.1 \Omega$	125
5.18	Total energy harvested by single impulse as a function of the input energy magnitude (solid line: numerical simulation, markers: experiments), a) modeling with b_2 as from Table 5.1; b) b_2 varying according to the energy level: I) $b_2 = 11 \text{ Ns/m}$ for $I_0 < 0.12 \text{ m/s}$, II) $b_2 = 5.4 \text{ Ns/m}$ for $I_0 \in [0.12, 0.18) \text{ m/s}$, III) $b_2 = 4.4 \text{ Ns/m}$ for $I_0 \in [0.18, 0.24) \text{ m/s}$, IV) $b_2 = 3.4 \text{ Ns/m}$ for $I_0 > 0.24 \text{ m/s}$	128
5.19	Dynamics of the two-DOF system for the very low input energy level ($I_0 = 0.10 \text{ m/s}$): time histories of the LO velocity (a) and BNEH relative velocity (b); (d) and (e) corresponding wavelet transform spectra; (c) measured voltage; (f) total energy harvested by the BNEH. — experimental trial, — corresponding numerical simulation.	129

5.20	Dynamics of the two-DOF system for the low input energy level ($I_0 = 0.14$ m/s): time histories of the LO velocity (a) and BNEH relative velocity (b); (d) and (e) corresponding wavelet transform spectra; (c) measured voltage; (f) total energy harvested by the BNEH. — experimental trial, — corresponding numerical simulation. . .	130
5.21	Dynamics of the two-DOF system for the high input energy level ($I_0 = 0.25$ m/s): time histories of the LO velocity (a) and BNEH relative velocity (b); (d) and (e) corresponding wavelet transform spectra; (c) measured voltage; (f) total energy harvested by the BNEH. — experimental trial, — corresponding numerical simulation.	131
5.22	Comparison of the total energy harvested by single impulse by different types of Energy Harvesters (EH): — current bistable EH, — — — current monostable EH, — optimal bistable EH, — — — optimal cubic EH, — · — linear EH with optimal linear stiffness coefficient.	132
5.23	Total energy harvested after 15 impulses as a function of the input magnitude and period of application of the pulse train: a) contour plot: numerical model, markers: experiments; b) red markers: numerical simulation, blue markers: experimental trials (the vertical dashed lines recall the position of the high-performance ribs). . . .	133
5.24	Numerical mean energy harvested over 100 impulses, $I_0 = 0.25$ m/s: — bistable EH, — — — monostable EH, • experimental trials. . .	135
A.1	Polynomial fitting of the force-displacement curve of the straight beam (red dotted line).	145

B.1	Numerical system response for $I_0 = 0.1$ m/s and $\mu_T = 3.06$ (on a rib): velocity time history of LO (a) and BNEH (b); (d) and (e) corresponding wavelet transform spectra; (c) measured voltage; (f) total energy harvested by the BNEH	148
B.2	Pseudo-experimental system response for $I_0 = 0.1$ m/s and $\mu_T = 3.06$ (on a rib): velocity time history of LO (a) and BNEH (b); (d) and (e) corresponding wavelet transform spectra; (c) measured voltage; (f) total energy harvested by the BNEH	148
B.3	Experimental system response for $I_0 = 0.1$ m/s and $\mu_T = 3.06$ (on a rib): velocity time history of LO (a) and BNEH (b); (d) and (e) corresponding wavelet transform spectra; (c) measured voltage; (f) total energy harvested by the BNEH	149
B.4	Experimental system response for $I_0 = 0.19$ m/s and $\mu_T = 4.34$ (outside the ribs): velocity time history of LO (a) and BNEH (b); (d) and (e) corresponding wavelet transform spectra; (c) measured voltage; (f) total energy harvested by the BNEH	150
B.5	Numerical system response for $I_0 = 0.19$ m/s and $\mu_T = 4.34$ (outside the ribs): velocity time history of LO (a) and BNEH (b); (d) and (e) corresponding wavelet transform spectra; (c) measured voltage; (f) total energy harvested by the BNEH	150

List of Tables

2.1	Power consumption of some common devices	10
2.2	Example of some vibration sources	14
4.1	Non-dimensional parameters of the system (3.53).	85
4.2	Dimensional parameters for the system (3.51).	86
5.1	Mechanical parameters	126
5.2	Electromagnetic parameters	126

Chapter 1

Introduction

In this chapter a general introduction to the topic of the thesis is presented, with particular reference to the motivation and objectives of this research work. The research framework is intentionally minimal, referring to the next chapter for an extended state of the art.

1.1 Research framework

Taking advantage of readily available, autonomous and durable energy sources is becoming an essential requirement for sustainable engineering systems. Pervasive mechatronic systems characterizing smart structures lead designers to consider renewable energy sources specifically targeted to feed the increasing number of embedded sensing and actuation devices. Wireless sensor networks for structural health monitoring applications are a valid example in which a self-sustaining power supply is required for the (often numerous) wireless components in order to guarantee a prolonged operational life. The possibility of harvesting energy from ambient sources to power application devices or energy storage elements is, thus, a critical problem, since it may enable small-scale wireless and portable electronic devices to be completely self-reliant. This is significant especially for

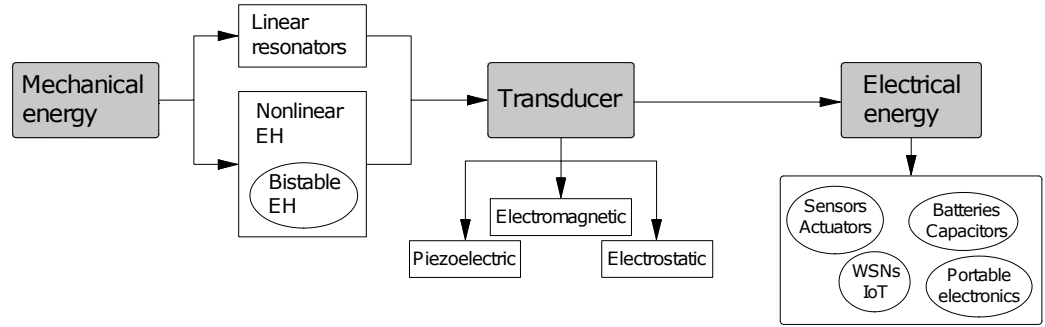


Figure 1.1: Block diagram of the energy harvesting process.

those cases in which battery maintenance or replacement can be complicated or even prohibited by the location of the device. Extracting power from ambient sources is generally known as energy harvesting, or energy scavenging. This approach has recently attracted a great deal of interest within both the academic community and industry, as a potential inexhaustible source for low-power devices. Using typical energy sources which are present in the natural environment, several hundred microwatts up to some milliwatts of electrical energy can be converted from one cubic centimeter size of an energy harvesting transducer. Among all the energy sources available for small-scale power generation, such as kinetic, solar, thermal, chemical, radio frequency etc., kinetic energy represents an attractive approach, because of its versatility and abundance. Vibratory energy harvesters exploit the ability of active materials (e.g., piezoelectric, magnetostrictive, and ferroelectric) and/or electromechanical coupling mechanisms (e.g., electrostatic and electromagnetic) to generate an electric potential in response to mechanical stimuli and external vibrations (see the block diagram of Figure 1.1). The sources of mechanical energy can be any vibrating structure, a moving human body or air/water flow induced motion, to name a few.

Most of the initial research focused on linear resonant vibration harvesters, which, operate based on the principle of linear resonance. However, they clearly possess some drawbacks that limit their applicability and effectiveness. The first limitation comes from their very narrow bandwidth, due to the fact that they are usually

designed to be very lightly damped such that the steady-state peak amplitude is maximized. In order to achieve acceptable performance, conventional vibration-based energy harvesting devices based on linear elements must be specifically tuned to match the frequency of the external vibration. Therefore, manufacturing tolerances, variations in the design parameters around their nominal values and/or variations in the nature of the excitation source can easily detune the harvester from the excitation frequency, drastically reducing the energy output. The bandwidth issue becomes fundamental for the performance of the harvesting device realizing that most realistic excitations present in the environment are not harmonic but have, instead, broadband or nonstationary (time-varying) characteristics, in which either the energy is distributed over a wide spectrum of frequencies or the dominant frequency varies with time. For example, environmental excitations to which a bridge is subjected are generally random, resulting from the wind loading, in which frequency and intensity vary depending on the atmospheric conditions, and moving vehicles in which number, speed, weight and so forth vary at different times during a given day. Impulsive excitations are also abundant in the mechanical and civil field: human activities, as walking or running on a pedestrian bridge, a train wheel moving on a railroad track, a motor car traveling along a road with a few of potholes or passing on a speed bump or an airplane encountering a local air turbulence are examples of a pulse-like vibration usable for energy harvesting purpose.

Various strategies have been investigated to overcome this practical inconvenient and increase the bandwidth of vibration-based harvesters. On one side, passive or active frequency tuning or oscillator arrays/multi-modal generators have been proposed. As for the former, tuning mechanisms can be realised mechanically using springs or screws, with magnets or using a piezoelectric material; as for the latter, different modes of a single oscillator or a series of resonators (commonly cantilevers) with properly designed properties integrated in one single device can be exploited to broaden the bandwidth of the harvester.

Alternatively, significant bandwidth improvement can be achieved through the introduction of nonlinearity into the design of an energy harvester. In principle, these type of harvesting devices possess a potential function $U(z) \neq 1/2kz^2$, denoting by k the linear stiffness and z the displacement. In practice, a nonlinearity of the third order is commonly exploited (it is easily achievable, by the transverse displacement of an elastic wire or thin beam for example), the potential function of which is written as $U(z) = 1/2kz^2 + 1/4k_{nl}z^4$, being k_{nl} the cubic stiffness coefficient. In particular, adding a strong (non linearizable) nonlinearity provides for frequency robustness, related to the bend of the response curve, that enables large amplitudes to persist over a much wider frequency range. The bandwidth of the nonlinear system depends on the damping ratio, the nonlinearity and the input excitation. If the system possesses a linear stiffness component negligible with respect to the cubic component (the system is, in this case, referred to as "essentially", or "purely", nonlinear), the lack of a preferential resonance frequency of the attachment theoretically enables it to engage in nonlinear resonances at arbitrary frequency ranges. Nevertheless, monostable nonlinear configuration have shown to possess a critical input energy threshold, resulting in ineffective harvesting of energy from low-amplitude vibration sources. In fact, under small excitation levels, the influence of the nonlinearity decreases and a monostable Duffing harvester loses its broadband properties, effectively acting as a linear resonator.

The strategy to efficiently harvest energy also from low-level, intermittent ambient vibration, proposed herein, relies on the unique properties of a particular class of strongly nonlinear vibrating systems that possess a multi-stable potential, instead of monostable, like the linear and purely cubic configurations. In particular, a bistable energy harvester, for which $U(z) = 1/2kz^2 + 1/4k_{nl}z^4$, $k < 0$, has two stable equilibrium states separated by a potential barrier (an unstable saddle). This enables the system to exhibit three different dynamic operating regimes depending on the depth of the potential barrier and the level of the input energy: in-well

oscillations (oscillations in the neighborhood of one of the two stable equilibrium positions) if the input energy is lower than the height of the potential barrier, a chaotic motion with alternating cross- and in-well oscillations for excitation energy sufficiently high to overcome the potential barrier, or large-amplitude periodic cross-well responses for further increase of the energy level. Among the several structures that can be conceived to attain the bistable mechanism, besides the simplest snap-through truss (or von Mises structure), buckled beams are commonly used in energy harvesting applications.

Since energy harvesting systems are commonly applied to vibrating structures, including civil structures, like bridges, or industrial machines, it is more interesting to investigate the integrated system composed of the nonlinear harvester coupled to a directly loaded host structure, rather than the harvester device by itself, in order to evaluate the dynamic interaction and energy exchanges between the two subsystems. Prior studies, mainly focused on essentially cubic nonlinear energy sinks coupled to a linear oscillator, have demonstrated how the nonlinear attachment can significantly alter the dynamics of the integrated system and, in particular, under certain conditions, can generate a number of nonlinear resonances, through which vigorous energy exchanges occur between the two oscillators and, possibly, energy localization into the attachment by means of resonance captures. Energy localization to the nonlinear attachment is pursued in order to attain efficient energy harvesting.

1.2 Aim and scope

Although incorporating bistable nonlinear harvesting systems into linear primary systems has not been explored in the literature, recent analytical and numerical studies restricted to the targeted energy transfer (TET) context highlighted that the use of bistability in the coupling between primary and auxiliary mass can break through the limit of the input energy threshold typical of the monostable nonlinear devices, producing an enhancement in the rapid passive energy absorption and

local dissipation of broadband input energies. The reason lies in the capability of engaging in the three distinct mechanisms, mentioned before, for energy localization in the nonlinear device, depending on the energy level initially input into the system. These results suggest the possibility of exploiting these energy transfer mechanisms to efficiently harvest power from ambient vibrations, usually characterized by very low amplitudes.

In this regard, this thesis seeks to expand the use of bistability in systems for enhanced vibration energy harvesting capability. The research work aimed to explore the potential benefit of adding a bistable element in the coupling for harvesting broadband and low-amplitude vibration energy. To this end, the present study is concerned with the theoretical and experimental investigation of a lightweight vibration-based energy harvesting device coupled to a weakly damped, primary linear oscillator (LO). It is pointed out that the resulting integrated system represents the main novelty of the present work, since energy harvesting systems are rarely studied in the literature in combination with the main structure on which they are supposed to operate. However, by doing so the dynamic interaction between the two sub-structures can be taken into account.

The mechanical coupling consists of an element which provides for both cubic nonlinear and negative linear stiffness components. The performance of the resulting bistable nonlinear energy harvester (BNEH) is studied under both isolated and repeated low-magnitude impulsive excitations directly imparted to the hosting linear structure. It is worth noting that impulsive excitation is not commonly considered as the vibration energy source, although it is pervasive in the structural environment.

Electromagnetic coupling elements are used for energy conversion. Among the current vibration-to-electricity transduction mechanisms (mainly electromagnetic, piezoelectric and electrostatic), the electromagnetic technique has the advantage of being relatively easily tunable to produce the desired electromechanical coupling, by varying the permanent magnet and the induction coil features and size, and allowing

low- to high-frequency applications based on a variety of system configurations. On the other hand, piezoelectric harvesting elements out-perform the electromagnetic harvesting elements in a small-scale apparatus, but the piezoelectric parameters are inherent to the material selected, making them not easily tunable or designable. Numerical simulations allowed to predict the favorable dynamic regimes for harvesting purposes. In particular, a thorough sensitivity analysis of the system's key parameters has been carried out to attain design insights for a BNEH able to achieve robust harvesting efficiency over a broad range of excitation magnitudes. This is achieved through the exploitation of the aforementioned main dynamical regimes explored by the BNEH. As a result, the benefit provided by the bistability for low energy level input into the linear oscillator, for which the essential cubic nonlinear harvester loses its effectiveness, has been demonstrated.

The design of a physical system with integrated energy harvester has been developed, guided by the preliminary numerical study, and the resulting experimental rig has been built, in order to validate the numerical findings.

1.3 Thesis outline

The thesis is organized as follows.

Chapter 2 lays the groundwork for framing the relevant issues around the problem of energy harvesting in a low-energy vibratory environment. In particular, the contextualization of the problem, background of the main types of energy harvesters existing in the literature and possible solutions to their limitations are discussed, together with the main electromechanical transduction techniques. Some considerations on the study of the dynamics of the energy harvesting system integrated to the hosting structure are emphasised and effective mechanisms for targeted energy transfer (TET) from the primary system to a nonlinear bistable attachment are described.

In Chapter 3, the derivation of the mathematical model of a coupled system composed of a linear primary system and a bistable nonlinear energy harvester is

presented and discussed.

Chapter 4 deals with the numerical study of the LO-BNEH coupled system. In particular, numerical simulations are carried out to analyze the effect of the most sensitive parameters on the energy harvesting efficiency. The role of key design parameters, such as mass ratio, BNEH damping and negative stiffness, on the coupled system response and the ensuing harvesting performance is examined and an optimal set of parameters for efficient energy harvesting from a broad range of excitation magnitudes is identified. The three efficient mechanisms for energy transfer are detected and the advantage over the monostable counterpart is demonstrated. The first two sections of Chapter 5 present the experimental fixture of the integrated system and set-up, together with a brief description of the system design and dynamic identification steps. Section 5.3 analyses the results of the experimental campaign, in terms of the system dynamics and performance under isolated and repeated impacts, and compares them to the monostable case. Finally, the main results are summarized in the last section and the novel contribution of this work are highlighted.

Chapter 2

State of the art

The work presented in this chapter lays the groundwork for the contextualization of the problem of energy harvesting in a low energy vibration environment. The main types of energy harvesters present in literature and possible solutions to their limitations are discussed, unto the description of the bistable solution, which is the subject matter of this dissertation. The importance of studying the dynamics of the energy harvesting system integrated to the hosting structure is emphasised and effective mechanisms for targeted energy transfer (TET) from the primary system to a nonlinear bistable attachment are described. Finally, the main technologies available for vibration-to-electricity conversion are briefly examined.

2.1 General overview on vibration energy harvesting

Self-powered ("fit-and-forget") systems have become a research hotspot over the last fifteen years, the main advantage being their minimum maintenance requirement. Autonomous and durable energy sources are of great interest to structural monitoring applications with wireless devices, such as sensors and actuators, but also to many other applications in all the engineering fields, including military monitoring devices, structure-embedded instrumentation, remote weather station,

Device type	Power consumption
Mobile phone calling	1 W
MP3 player	50 mW
Functioning of a LED light	10 mW
2-axis accelerometer sensor	2 – 3 mW
Temperature sensor (active mode)	3 mW
Functioning of a wireless sensor node	100 μ W
Cardiac pacemaker	50 μ W
Temperature sensor (sleep mode)	10 μ W
Quartz wristwatch	5 μ W
Sleep mode of a microcontroller	10 nW

Table 2.1: Power consumption of some common devices

calculators, watches, Bluetooth headsets, biomedical implants (a pacemaker or a spinal stimulator for example), which traditionally have relied on batteries that need periodical replacement. Wireless solution demand for sensors, actuators and the other embedded electronic devices, together with the trend of decreasing their power consumption and increasing efficiency, opened novel lines of research on sustainable, long-term and low-maintenance power supply. Energy harvesting systems, through the conversion of energy available from the environment from the primary form into suitable secondary form (usable electric energy), can be used either to charge batteries or supercapacitors or as independent power sources. This reduces the reliance of wireless systems upon batteries and is particularly relevant for devices located in areas that are inhospitable or difficult to reach for maintenance and battery replacement.

Energy harvesting implementation field is typically confined to low power applications, including sensors, data transmitters, controllers or portable electronics. Currently, the power consumption of these devices ranges from tens of μ W for wristwatches or MEMS sensors up to few hundreds of mW for mobile phones or GPS applications [25, 26] (Table 2.1). Generally energy harvesting suffers from low, variable and unpredictable levels of available power. Level and fluctuation of electrical output depend on the design of the transducer and properties of the ambient energy source. Hence, energy management is required to adapt the

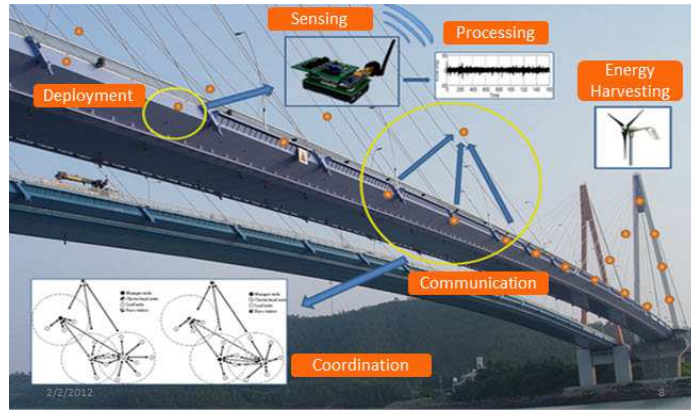


Figure 2.1: Example of wireless sensor network on a bridge.

electrical energy obtained to the requirements of the application device or the energy storage element. This often means converting the voltage level or rectifying and filtering pulse currents, controlling the peaks and adopting energy buffers. Special care must be taken in matching the internal resistance of the transducer and the power management or the load to maximize the harvested energy.

Wireless sensor networks (WSNs), among the most effective technologies in the structural health monitoring (SHM) field, are continuously developed and enhanced; they are specifically designed for very low power operation. The technology of a WSN consists of a grid of spatially-distributed autonomous devices, using smart sensors to monitor and communicate information about physical or environmental conditions, like acceleration, temperature, pressure, magnetic field, concentration of a given particle in the air and so on. A schematic view of a WSN is depicted in Figure 2.1. A WSN system incorporates a gateway that provides wireless connectivity back to the wired world and distributed nodes (Figure 2.2).

Currently, WSNs have characteristics of ubiquity, self-healing and self-organizing; feeding them through scavenged energy would increase their operational life, which strongly depends on the balance between power consumption and energy storage, and guarantee the possibility of continuous automated SHM. To give an example, structural health of buildings and bridges monitoring and control would require up to thousands of integrated sensors. The current consumption of a WSN (Wireless

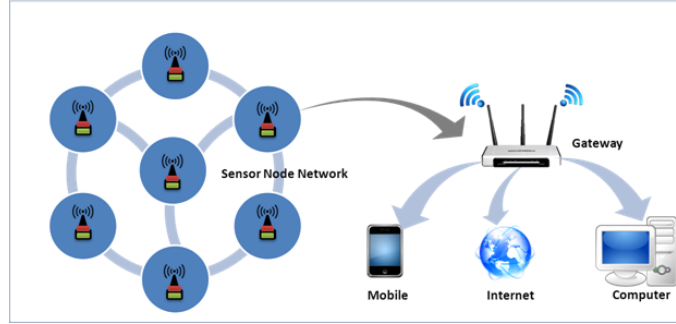


Figure 2.2: Flux of information among the sensors grid and up to the end user.

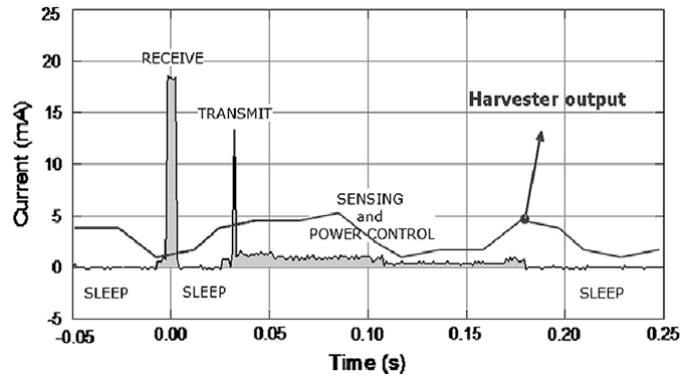


Figure 2.3: A typical power consumption scenario of a sensor node. Since the consumption does not equally match the harvester output, an energy buffer and power management IC in between is necessary [1].

Sensor Network) node during operation can be estimated to be less than 30 m A [27, 28, 29], with power consumption of the communication module reduced to 1 to 3 m W depending on number of state transitions, communication modulation and strategies adopted for power consumption minimization [30]. They are usually in a sleep mode for 99.9% of their lifetime, waking up for few milliseconds during the communication operation (Figure 2.3). Consequently, the average power consumption is reduced to tens of μW . Ultimately, harvesting energy is the only way for the development and integration of the so-called "Internet-of-Things" (IoT), defined as "an interconnection of uniquely identifiable embedded computing devices within the existing Internet infrastructure, offering advanced connectivity of devices, systems, and services that goes beyond machine-to-machine communications and covers a variety of protocols, domains, and applications" [31].

A variety of ambient energy sources are available for small scale power harvesting:

- natural energy: wind, water flow, ocean waves, solar energy;
- mechanical energy: vibrations from machines, mechanical stress, object's movement, strain from high-pressure motors, to name a few;
- thermal energy: wasted heat from furnaces, heaters or friction sources; thermal gradients in the environment are directly converted to electrical energy through the Seebeck (thermoelectric) effect;
- light energy: indoor room light and outdoor sunlight energy; it can be captured via photo sensors, photo diodes, and solar photovoltaic (pv) panels;
- electromagnetic energy (RF): base stations, wireless internet, satellite communication, radio, TV, digital multimedia broadcasting, etc.;
- chemical and biological sources.

Given that vibration sources are pervasive in the environment, kinetic energy generators are one of the most attractive solutions for powering autonomous small-scale systems, on which several studies have focused over the last years. Ambient mechanical vibrations, including vibrations from industrial machinery and civil structures, fluid flow, as air movements or ocean waves, wind and aeroelastic vibrations, rotational kinetic energy are some of the most frequently exploited energy sources. Because of the heterogeneity of the kinetic energy sources, the amount and form of the available energy can vary significantly. Focusing on relatively low-level vibrations that occur in common environments, some measured data obtained from several vibration sources are summarized in Table 2.2. All these different sources produce vibrations that can vary considerably in amplitude and spectral characteristics. Figure 2.4 shows, as an example, three different frequency spectra of vibrations coming from three different environments: a car hood in motion, an operating microwave oven and a surge induced sloshing in a LNG carrier

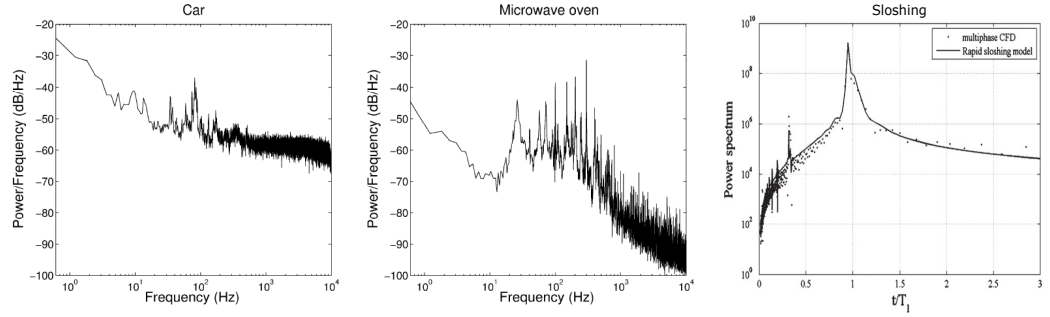


Figure 2.4: Power spectra of vibrations in three different environments [2, 3].

Vibration source	Peak acceleration (m/s^2)	Frequency (Hz)
External windows next to a busy street	0.7	100
Notebook computer during CD reading	0.6	75
Door frame as door closes	3	125
Base of 3-axis machine tool	10	70
Washing machine	0.5	109
Small microwave oven	2.25	121

Table 2.2: Example of some vibration sources

membrane tank. In Figure 2.5 some examples of vibration which civil structures undergo in operational conditions are also shown. These very distinct behaviours in the vibration energy sources available in the environment reflect the difficulty of providing a general viable solution to the problem of vibration energy harvesting. In the literature it is very common to consider a very special vibration signal represented by a sinusoidal signal of a given frequency and amplitude. Perfectly sinusoidal vibration, however, is able to represent only a narrow class of vibrations available in the real environment. It can be found, for instance, in rotating machines. For such vibrations, linear resonators, operating at their resonant frequency, are suitable for harvesting power efficiently, as will be discussed in Section 2.2.1. Hassaan's study in [32], for example, focused on machinery systems driven by sinusoidal excitation and proposed the adoption of a mass-spring absorber as a energy harvester, tuned so to achieve both machinery vibration reduction and maximum energy production.

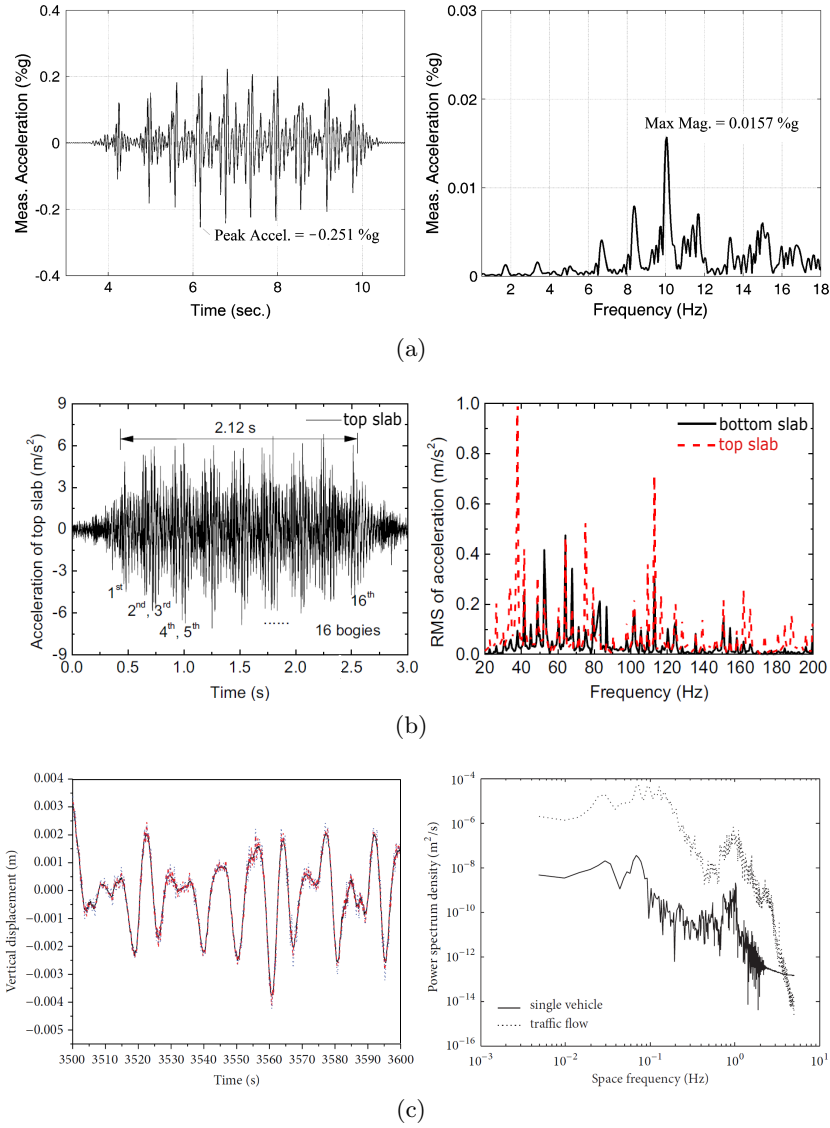


Figure 2.5: Time histories and spectra of different types of vibrations: (a) response to walking of a high-frequency floor bay [4]; (b) vibration of the slabs of a box-shaped deck due to train-induced noise in the cavity arising from vibrating bridge components [5]; (c) vertical displacement response to traffic flow of the deck of a cable-stayed bridge [6].

Most realistic excitations seen in the environment are often not harmonic but have broadband or nonstationary (time-varying) characteristics, in which either the energy is distributed over a wide spectrum of frequencies or the dominant frequency varies with time. For instance, environmental excitations to which a bridge is subjected are generally random, resulting from wind loadings in which frequency and intensity vary depending on the atmospheric conditions and moving vehicles in which number, speed, weight, etc. vary at different times during a given day. Common sources for oscillations in microsystems have white noise characteristics due to non-equilibrium thermal fluctuations, shot, and low-frequency noise. For random vibrations, exploiting the energy content within any of the different frequencies of which their frequency spectrum is composed is challenging and requires specific technologies for the harvesting device, as will be discussed in the next section.

Another peculiar class of vibration is represented by impulses, denoted by a big amount of energy in a short time interval. Impulsive excitation is not normally considered in literature as a vibration source for energy harvesting studies, although it is ubiquitous in the structural environment, and, for this reason, adopted in the present research work. Human activities, such as running or jumping on a pedestrian bridge, or a train wheel moving on a railroad track (see Figure 2.6), or a car wheel passing on a speed bump are only a few representative cases of a pulse-like vibration usable for energy harvesting purpose. For example, Shenck and Paradiso [33] described shoe inserts capable of generating an average power of 8.4 mW in a $500 \text{ k}\Omega$ load under normal walking pace. Power of the order of some micro-Watt can be scavenged by the impact of a water drop falling with velocity from 1 to 3 m/s on a piezoelectric flexible structure [34, 35]. Impulsive vibrations can be nearly periodic or random. Perhaps the most typical example of a random pulse train is the vehicle traffic load on a highway bridge, but excitations of that kind are encountered in different problems of engineering, for example a non-stationary earthquake excitation regarded as a sequence of shocks which first

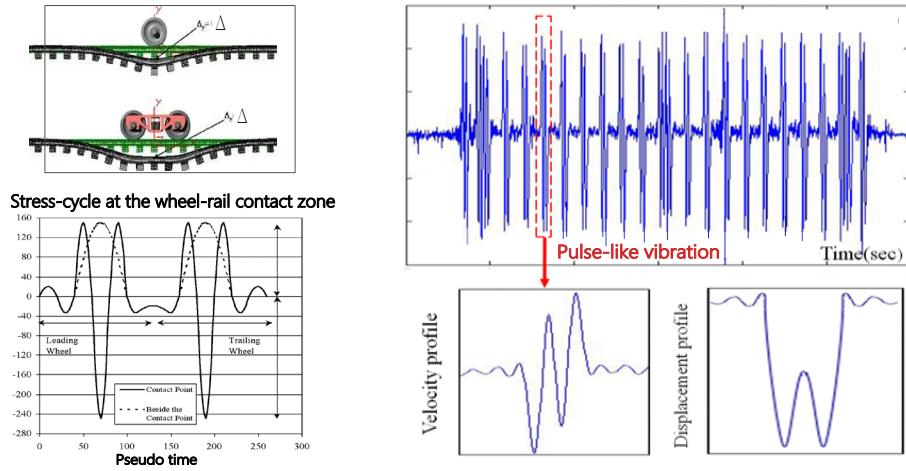


Figure 2.6: Pulse-like vibration profiles of railroad tracks [7].

build up and next die out with time, randomly arriving wind gusts associated with eddies, intermittent excitation of an airplane tail, or the behaviour of a vehicle travelling over rough ground, where the vehicle structure is subjected to shocks produced by sudden bumps in the ground surface. Also dynamic loading due to wave slamming which acts on a ship hull structure or on some members of an off-shore structure may be modelled as a train of randomly arriving loading pulses. Impulsive excitation are well suited for energy harvesting purpose, since they permit one of the most efficient mechanisms for energy transfer from the excited structure to an attached (nonlinear) device to occur. This mechanism relies on the excitation of so-called impulsive periodic and quasi-periodic orbits and will be discussed in Section 2.3.

2.2 Suitable dynamic regimes

2.2.1 Energy harvesting via linear resonators

In the last fifteen years, the field of vibration-based energy harvesting has received growing attention, as shown by the rising number of publications covering a wide variety of mechanisms and techniques. Most of the initial research focused on linear resonant vibration harvesters [36, 37, 38]. Vibration energy is best suited to

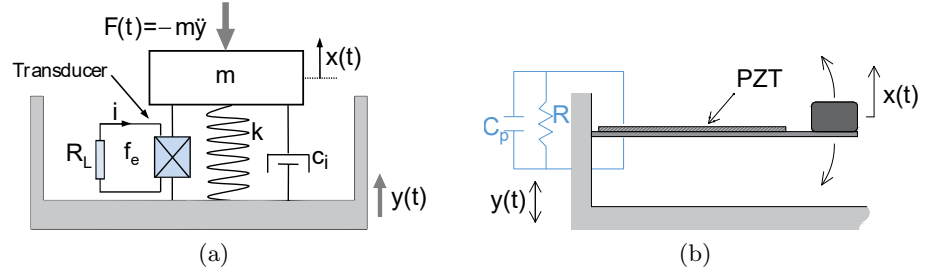


Figure 2.7: Schematic of a linear inertial generator (a); piezoelectric linear cantilever beam (b).

inertial generators, rather than directly excited generator, because they require only one point of attachment to a moving structure, allowing a greater degree of miniaturization. Figure 2.7(a) depicts the schematic of an inertial generator, based on a seismic mass m and a spring of stiffness k . Energy is converted when work is done against the damping force $c\dot{z}$, which opposes the relative motion $z(t) = x(t) - y(t)$. In order to generate power, the damper must be equipped with a transduction mechanism, which extract the energy in the form of electrical energy. The damping coefficient c includes, in general, both inherent and/or parasitic damping c_i and a damping-like coefficient related to the transducer c_T . One of the most common configuration of a linear energy harvester is depicted in Figure 2.7(b): a base-excited cantilever beam with a proof mass at the tip, performing small oscillations, most widely used for piezoelectric generators. The linear energy harvester possesses a quadratic potential energy $U(z) = 1/2kz^2$, with k the linear stiffness. For the case of a cantilever beam, k is given by $k = 3EI/L^3$, where E is the modulus of elasticity, I is the moment of inertia and L the length of the beam.

The functioning principle simply follows the general theory of a single degree of freedom lumped spring mass system. Hence, assuming a sinusoidal displacement of amplitude Y and frequency ω , $y(t) = Y \sin \omega t$, as the base excitation, the governing

equation of motion is described by ¹:

$$m\ddot{z}(t) + c\dot{z}(t) + kz(t) = -m\ddot{y}(t) \quad (2.1)$$

the steady-state solution of which can be written in terms of damping constant and natural frequency as:

$$z(t) = \frac{\left(\frac{\omega}{\omega_n}\right)^2}{\sqrt{\left[1 - \left(\frac{\omega}{\omega_n}\right)^2\right]^2 + \left(2\xi\frac{\omega}{\omega_n}\right)^2}} Y \sin(\omega t - \phi), \quad \phi = \arctan \frac{2\xi\omega_n\omega}{\omega_n^2 - \omega^2} \quad (2.2)$$

where $\xi = c/(2m\omega_n)$ is the damping ratio, $\omega_n = \sqrt{k/m}$ is the natural frequency and ϕ the phase angle. The power dissipated within the damper (i.e. extracted by the transduction mechanism and parasitic damping mechanisms) is given by [39]:

$$P = \frac{m\xi Y^2 \left(\frac{\omega}{\omega_n}\right)^3 \omega^3}{\left[1 - \left(\frac{\omega}{\omega_n}\right)^2\right]^2 + \left(2\xi\frac{\omega}{\omega_n}\right)^2} \quad (2.3)$$

It is well known that that maximum power is generated at the resonance frequency of the linear oscillator and that the damping has the effect of broaden the bandwidth of the device, as shown in Figure 2.8, in which power is plotted as a function of the frequency ratio for various damping factors.

The damping factor controls the selectivity of the device. For applications where the frequencies of vibration are well defined and stable in time, a low damping factor would give a more peaked response and increase power generation. Conversely, if the fundamental vibration frequency varies over time, a higher damping factor would be necessary to widen the bandwidth of the generator; nevertheless, the amount

¹Strictly speaking, Equation (3.18) is valid for an electromagnetic generator, where the damping coefficient includes the damping caused by electromagnetic coupling. Damping arising from piezoelectricity cannot be modeled as a viscous damping and Equation (3.18) should be modified by adding a coupling term, i.e.

$$m\ddot{z}(t) + c\dot{z}(t) + \kappa V + kz(t) = -m\ddot{y}(t)$$

where κ is the electromechanical coupling coefficient and V is the output voltage on the electrical load.

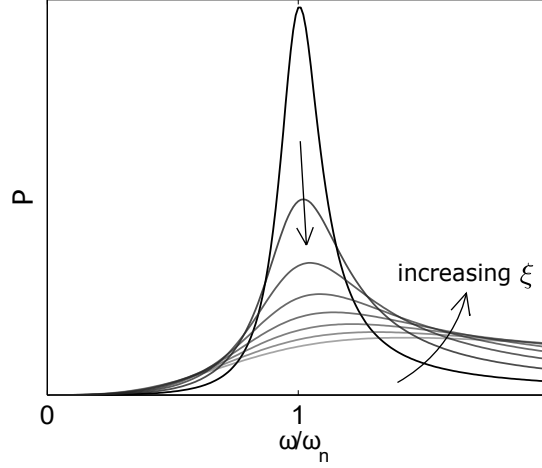


Figure 2.8: Frequency spectrum of power generation around the resonance frequency of the generator for various damping factors. The arrows indicate the trend of the curves for increasing values of damping.

of power deliverable, even at resonance, would drastically decrease. Moreover, from Equation (2.3), the amount of power generated is proportional to the cube of the vibration frequency. This means that the generator is likely to produce much more power in applications with a fairly high frequency of vibration and is likely to perform poorly at low frequencies (1-100 Hz), which is where most ambient vibration exists.

When the generator operates at resonance, the maximum power can be obtained. In this case, Equation (2.3) gives:

$$P = \frac{mY^2\omega_n^3}{4\xi} \quad (2.4)$$

Infinite power at zero damping, coming from (2.4) is only theoretical. In practice, since reducing the damping factor increases the displacement of the mass, which is limited by the size and geometry of the device, the damping factor must be large enough to prevent the mass displacement exceeding its maximum, Z_{max} . The maximum power that can be generated is, in fact, $P_{max} = m\xi\omega_n^3 Z_{max}^2$. Equation (2.4) should be modified if the inherent/parasitic damping (ξ_i) is of the same order of

magnitude as the transducer damping (ξ_T), as:

$$P = \frac{m\xi_T Y^2 \omega_n^3}{4(\xi_i + \xi_T)^2} \quad (2.5)$$

Ultimately, linear harvesters have demonstrated some critical drawbacks that limit their effectiveness in many field of application. Specifically, they work optimally only when their natural frequency is tuned to the excitation frequency (resonance condition). This presupposes a priori knowledge of the excitation frequency and its persistency in time. Indeed, any variations in the excitation frequency around the harvester's fundamental frequency decreases the coupling between the source and the harvesting device and reduces the output power significantly. Hence, the narrow bandwidth of the linear harvesters limits their applications in practical scenarios where the ambient vibration source has a broadband, time-varying or even random frequency spectrum.

Many methods have been explored to increase the operational frequency range of a vibration energy-harvesting device, by both tuning the resonant frequency and broadening the bandwidth of the harvester. Recent examples include active frequency-tuning techniques (which, however, are rarely applicable in practice, since they require a certain amount of power input that, generally, outweighs the power generated), multi-modal oscillators, cantilever arrays and amplitude limiters [40, 41, 42]. Shahruz in [43] studied the design of an ensemble of cantilever beams with proof masses at the tips, as in Figure 2.9(a), that can function as a band-pass filter exploitable for energy harvesting purpose, by properly choosing the dimensions of beams and masses. It was also shown that the maximal frequency band of the band-pass filter is limited and independent of dimensions of the beams and masses of the proof masses, thus it cannot be chosen arbitrarily large.

Optimizing strategies for excitations with time-varying frequency were formulated theoretically in [18] for a linear single degree-of-freedom harvester, consisting of a piezoelectric (PZT) stack and a proof mass and found the dependence of the average output power on the frequency sweep rate, center frequency and range of excitation.

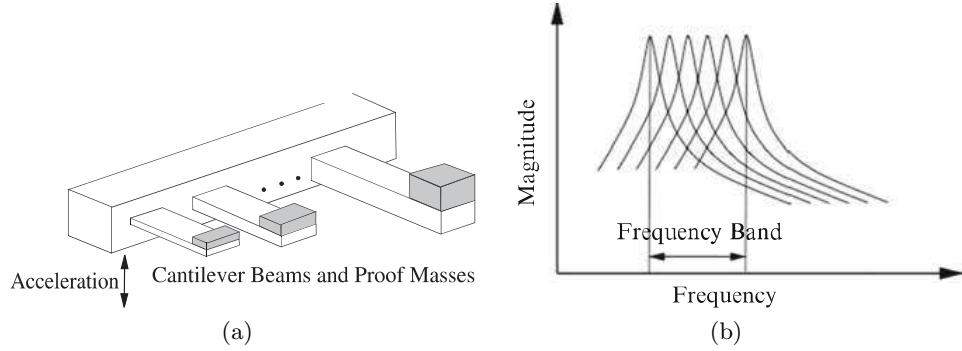


Figure 2.9: Ensemble of cantilever beams with proof masses at their tips (a) and transfer functions corresponding to the beam-mass systems (a) when the device functions as a band-pass filter (b).

The authors proved that in certain conditions, tuning the excitation's center frequency outside the bandwidth of the steady-state fixed-frequency harvester and away from its resonance frequency can be beneficial in terms of the average output power.

Since linear resonators, as mentioned before, work most likely at high frequency, whereas ambient vibration spectra have usually significant predominance of low frequency components, frequency-up conversion techniques have been proposed to "shift" the source vibration frequency to the harvester resonance frequency so that useful power can be harnessed in low frequency excitation scenarios.

Alternatively, significant bandwidth improvement can be achieved through the introduction of nonlinearity into the design of an energy harvester, which will be discussed in section 2.2.2.

It is worth noting that a bound for the energy harvesting performance of a linear oscillator is imposed by its mass. As becomes apparent from Equation (2.3), the maximum power achievable by a linear harvesting system under sinusoidal external excitation is dependent upon its mass. This statement is generalizable. It is known, in fact, that the power dissipated by a linear single degree of freedom oscillator subject to white noise base acceleration depends only on the mass of the system

and the spectrum of the input, according to the relation:

$$P = \pi \frac{m S_0}{2} \quad (2.6)$$

where S_0 is the spectrum of the base acceleration and m is the mass of the oscillator. Equation (2.6) provides an upper bound on the power that can be harvested, regardless of the values of linear damping or stiffness, meaning that there is very limited scope for optimal design. Moreover, other studies have demonstrated that the latter result applies also to multi degree-of-freedom linear systems and to single and multi degree-of-freedom systems with nonlinear stiffness driven by white noise base acceleration [44]. In the latter case, m refers to the total mass of the system.

2.2.2 Adoption of nonlinear devices for energy harvesting purpose

A significant number of research studies are currently focused on the idea of incorporating nonlinearities into the harvester's design so as to extend its bandwidth, providing a possible solution for frequency mistuning, and enhance its performance in a non-stationary vibratory environment. The WISEPOWER srl, company of energy generators design and manufacturing site in Terni, Italy, declared a considerable increase of the energy conversion efficiency enabled by nonlinear dynamics solutions, based on the research work carried out in the NiPS (Noise in Physical Systems) Laboratory at the Physics Department of the University of Perugia, Italy.

The dynamics of the general nonlinear energy harvesting system (NEH) is described by:

$$m\ddot{z}(t) = -\frac{dU(z)}{dz} - c\dot{z}(t) + f(t) \quad (2.7)$$

where $U(z) \neq 1/2kz^2$ is the potential function and $f(t)$ the generical input force coming from the ambient vibration, which can be written as $f(t) = -m\ddot{y}(t)$ in case

of base excitation. Specifically, one class of nonlinear harvesters widely investigated incorporates cubic stiffness nonlinearities. The potential energy function is of the form:

$$U(z) = \frac{1}{2}az^2 + \frac{1}{4}bz^4 \quad (2.8)$$

with $a > 0$, therefore it exhibits mono-stable characteristics and the dynamics is described by a (electromechanically coupled) Duffing's equation, with restoring force $F(z) = az + bz^3$. Ideally, the maximum amount of power harvested by a nonlinear system is approximately the same as the maximum power harvested by a linear system [20] but a strong nonlinearity ("essential", i.e. non linearizable) provides for frequency robustness, related to the bend of the response curve, that enables large amplitudes to persist over a much wider frequency range. The bandwidth of the nonlinear system depends on the damping ratio, the nonlinearity and the input excitation. The response curve bends with respect to the vertical configuration of the linear case, towards right or left direction depending on the type of nonlinearity (hard or soft nonlinearity, respectively), till the jumping phenomenon appears and the response of harvester has three periodic solutions, which include two stable solutions and one unstable solution. The bending of the response curve increases (lowers) the frequency corresponding to the maximal amplitude and power, thus it is beneficial for the harvester to work in higher- (lower-) vibration frequency environment ². For the two stable solutions of the nonlinear response, one is relatively small and the other is relatively big. Therefore, in order to output larger power, the nonlinear harvester should work at the stable response of high energy orbit (Figure 2.10). In other words, the advantage imparted by the non-linearity depends on realizing the high-energy attractor. A linearly decreasing or increasing frequency sweep can capture the high-energy attractor, and, hence, improve the output power and bandwidth for the softening and hardening cases, respectively. Unfortunately, such conditions cannot be guaranteed in practice. Should the lower-

²Typically, the goal is to increase the capability of a harvesting device at low frequency (below few hundred Hz) because this is where most of the ambient energy is available. Due to geometrical constraints, a small dimension linear harvester is, in general, not feasible.

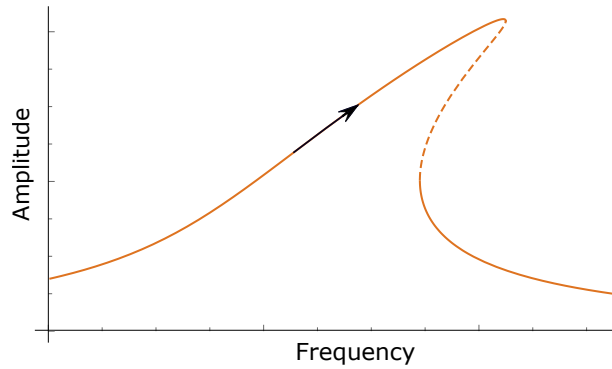


Figure 2.10: Hardening behaviour of a nonlinear system.

energy branch manifest instead, a momentary electrical short-circuit or mechanical perturbation may be required.

Essentially nonlinear, monostable configurations have been proposed to accommodate frequency variation and frequency mistuning and to enable the energy harvesting system to capture energy available from more complex excitations [45, 46, 47, 48]. However, they have been shown to possess a critical input energy threshold, resulting in ineffective harvesting of energy from low-amplitude vibration sources. In fact, under small excitation levels, the influence of the nonlinearity decreases and a monostable Duffing harvester loses its broadband properties, effectively acting as a linear resonator [47]. As an example, results by Mann and Sims [8] are presented in Figure 2.11, in which velocity response curves for two different amplitude of the base acceleration are contrasted. The system under investigation is an electromagnetic NEH harvesting from the nonlinear oscillations of a magnet in levitation. The magnetic levitation system is realized by placing a center magnet between two outer magnets into a base-excited tube, with the poles oriented so to repel the outer magnets, thus, suspending the center magnet with a non-linear restoring force (Figure 2.11(a)). It becomes apparent from Figure 2.11(b) that at relatively low excitation levels, the frequency response of the system looks very similar to the response of a linear system, whereas an increase of the excitation level causes the response curve to bend to the right (multiple periodic attractors and hysteresis in the frequency response curve).

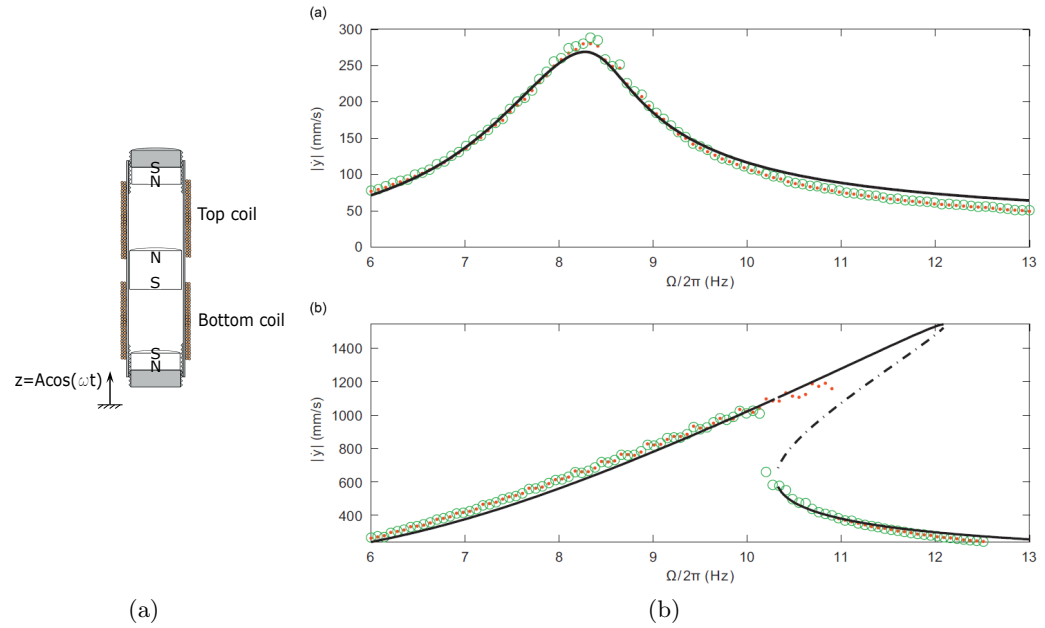


Figure 2.11: Sketch of the NEH proposed by [8] (a); Experimental (markers) and theoretical (black line) of the velocity response for low (top) and high (bottom) excitation level (b).

Stanton et al. [9] proposed another monostable nonlinear device for energy harvesting through piezoelectric effect. The device consists of a piezoelectric beam with a magnetic end mass interacting with the field of oppositely poled stationary magnets, as shown in Figure 2.12(a). The dimensional tip displacement and voltage response of the device under sinusoidal base excitation are plotted in Figure 2.12(b) for two excitation amplitudes (the lighter solid line is the response at the lower excitation amplitude) and it shows that the hardening behaviour tends to vanish as the excitation amplitude decreases. Another interesting outcome of this study is that, by tuning the nonlinear magnetic interactions around the end mass (i.e., tuning the distance d), the harvesting device is capable of both hardening and softening behaviour, surpassing many other mechanism, that can only broaden the frequency response in one direction.

Finally, according several research studies, nonlinear energy harvesters seem not to provide a significant advantage in harvesting energy in a random excitation environment. Daqaq demonstrated that under White Gaussian excitation, the

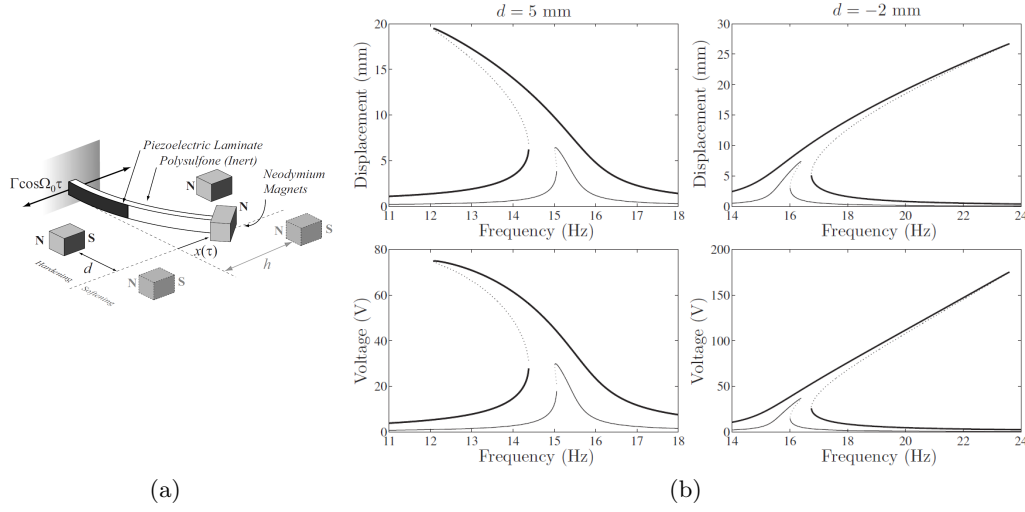


Figure 2.12: Sketch of the NEH proposed by [9] (a); displacement and voltage response for a low (higher line) and high (ticker line) excitation level for different values of d (b).

hardening-type non-linearity failed to provide any enhancement of output power over the typical linear harvesters. Under colored Gaussian excitations, the expected output power even decreased with such hardening-type non-linearity [49].

Barton [46] tested an electromagnetic NEH under both periodic and narrow-band random excitation and showed that the peak velocity attained by the harvester under periodic excitation is never reached by the harvester under random excitation. A new class of nonlinear harvesters with a bi-stable potential has been recently investigated as a possible solution to improve the performance of energy harvesters in case of both low-level energy excitations and non-stationary vibratory environments.

2.2.3 Bistable solutions

As shown in Figure 2.13, an energy harvester with a bistable potential (bistable nonlinear energy harvester, BNEH) has two stable equilibria separated by a potential barrier (an unstable saddle). The potential function is of the form given by Equation (2.8) with $a < 0$. This provides for three different dynamic operating regimes depending on the energy level input into the system. Namely, the bistable

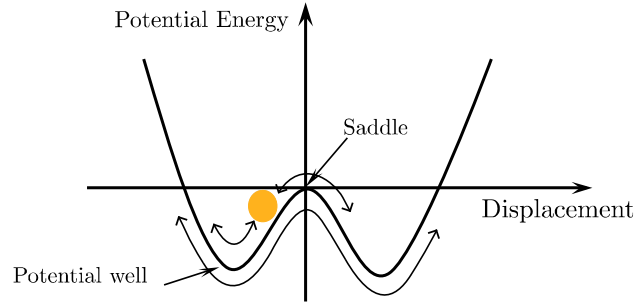


Figure 2.13: Double-well potential of a bistable oscillator showing example trajectories for in-well, chaotic cross-well and periodic cross-well oscillations.

system can perform low-energy in-well oscillations, whereby the inertial mass oscillates around one of the stable equilibrium positions, as shown in Figure 2.14(a), where the response trajectory (upper graph) and phase portrait with an overlay Poincaré map (lower graph) are displayed. When sufficient energy is supplied to the system, dynamic trajectories overcome the potential barrier and escape from one potential well to the other activating the inter-well dynamics, characterized by aperiodic or chaotic vibrations between wells (Figure 2.14(b)). This non-resonant behavior permits coupling between the environmental excitation and the energy harvester over a wider range of frequencies. As the excitation energy is further increased, the device may exhibit periodic cross-well oscillations (Figure 2.14(c)). The latter have been recognized as a means by which to dramatically improve energy harvesting performance. This is due to the fact that, since the inertial mass must displace a greater distance from one stable state to the next, its velocity is much greater than that for in-well or chaotic vibrations. As the electrical output of an energy harvester is dependent on the mass velocity, high-energy orbits substantially increase power per forcing cycle (as compared with in-well and chaotic oscillations) and are more regular in waveform (as compared with chaotic oscillations), which is preferable for external power storage circuits. Additionally, snap-through may be triggered regardless of the form or frequency of exciting vibration, alleviating concerns about harvesting performance in many realistic vibratory environments dominated by effectively low-pass filtered excitation [10]. Generally speaking, the

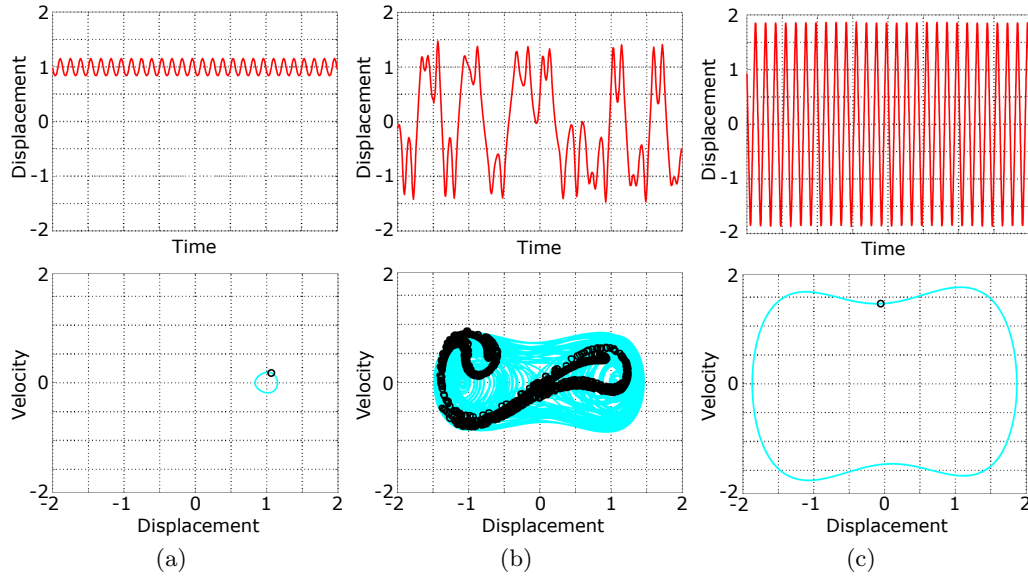


Figure 2.14: Example of displacement response trajectories (top row) and phase plots with an overlap Poincaré map as black circles (bottom row) for the three dynamic regimes of a BNEH: in-well oscillations (a), chaotic in-well and cross-well vibrations (b) and periodic cross-well oscillations (c) [10].

three dynamic regimes may theoretically coexist although only one is physically realizable at a time.

The simplest bistable structure is the von Mises truss, that is realized by means of two oblique elastic bars mutually hinged at the top. When the structure is disturbed by a sufficiently high external loading action, that can be of the form of either vertical force or vertical displacement at the top hinge, it reaches a limit point (evanescence of the stiffness), losing its stability, and a snap through occurs, causing a sudden jump from the stable equilibrium position to the next one (Figure 2.15). During the snapping-through phase, the trusses go through the horizontal unstable equilibrium. If the downward load is decreased the structure encounters a second limit point where the trusses suffer a reverse snapping to an upward configuration. The part of the equilibrium path between the two limit points (the dashed portion of the force-displacement and potential curves in Figure 2.15) is the set of unstable equilibrium states where the trusses are compressed to a level that the negative geometric stiffness overcomes the elastic stiffness. For such this structure, subject

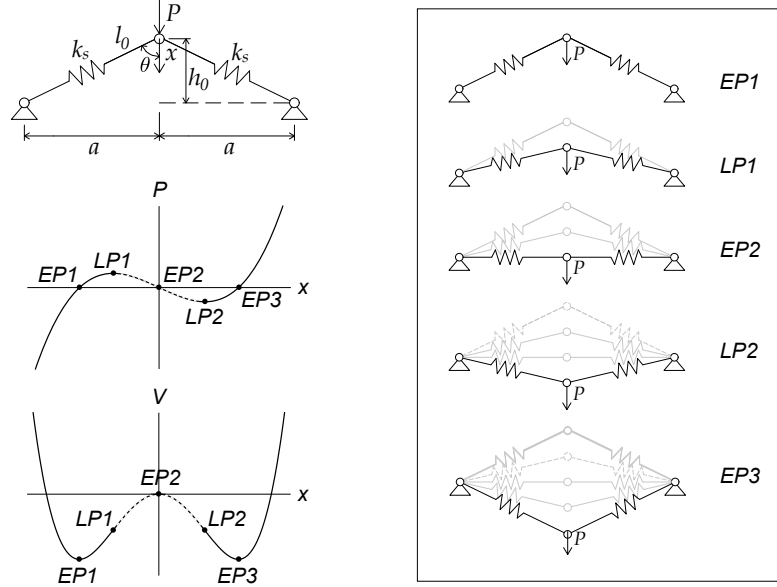


Figure 2.15: The von Mises structure, restoring force and potential function (left-hand side) and configurations at limit points (LPs) and equilibrium points (EPs) (right-hand side). EP1 and EP3 are stable, EP2 is unstable.

to a downward load P at the keystone, letting θ the angle with respect to the vertical, the equilibrium equation, under the hypothesis of identical trusses, can be written as:

$$2T\cos\theta + P = 0 \quad \text{where} \quad (2.9a)$$

$$T = k_s(l_0 - \sqrt{a^2 + (h_0 - x)^2}), \quad \cos\theta = \frac{h_0 - x}{\sqrt{a^2 + (h_0 - x)^2}} \quad (2.9b)$$

In (2.9) T denotes the tension in each spring, k_s is the trusses equivalent spring constant, l_0 the initial length of the trusses, h_0 and a as in Figure 2.15. Substituting the expressions for T and $\cos\theta$ (2.9b) in (2.9a), the governing equation of the elastic problem, in terms of the vertical displacement of the keystone x is, then, given by:

$$P + 2k_s \left(1 - \frac{l_0}{\sqrt{a^2 + (h_0 - x)^2}} \right) (h_0 - x) = 0 \quad (2.10)$$

The restoring force is clearly nonlinear and it can be expressed as a cubic polynomial using the binomial expansion of the square root truncated at the third order. By

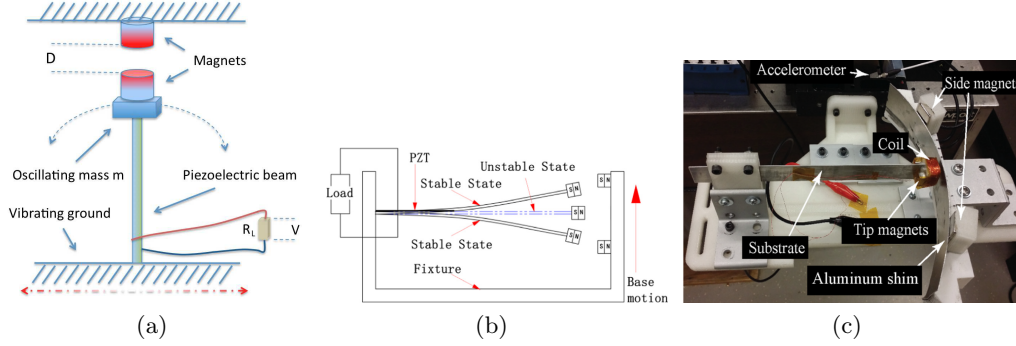


Figure 2.16: Drawing of a piezoelectric bistable cantilever beam with a tip magnet and one (a) or two (b) fixed magnets; experimental fixture of an electromagnetic cantilever beam with tip magnet by [11] (c).

setting the origin of the variable on the axis passing through the supports (or, equivalently, operating the change of variable $x = h_0 - y$), the simple expression for the restoring force F_s is obtained, as:

$$F_s = \alpha y + \beta y^3 \quad \text{where} \quad \alpha = 2k_s(1 - l_0/a) \quad \text{and} \quad \beta = k_s l_0/a^3 \quad (2.11)$$

The coefficient of the linear term α is clearly negative.

Several structures can be conceived to attain the snap-through mechanisms, besides the snap-through truss. Among all, buckled beams are a common solution for energy harvesting applications. A beam axially compressed beyond its first critical buckling load behaves, in principle, as a von Mises structure; since it represents the bistable element of the energy harvester under investigation in the present work, its mechanical characterization will be extensively discussed in Section 3.1.

Another frequently used structure is a cantilever beam holding a magnet at its tip and an external magnet conveniently placed at a certain distance from the tip magnet and with polarities opposed to those of the tip magnet. Alternatively, a couple of external magnet would have same polarities as the tip magnet (Figure 2.16).

Bistable configurations have received much attention due to their capacity for high output power when they snap through from one stable state to another, providing large-amplitude motions across a wide range of input frequencies [50, 51, 52]. Erturk et al. [53] proved that a piezomagnetoelastic harvester driven by harmonic

base excitation can produce one order of magnitude larger power output over a given excitation frequency range, compared with the conventional case without magnetic buckling.

Gammaitoni et al. [54] numerically explored the average voltage drop produced by a piezoelectric oscillator under a wide-bandwidth Gaussian noise, as a function of the linear stiffness coefficient. The voltage was found to reach a maximum when the latter takes negative values.

A piezoelectric axially loaded beam was theoretically and experimentally investigated by Cottone et al. [55] under wideband random vibrations. The buckled configuration enabled a significant amplification of displacement and output voltage compared to the unbuckled case.

Many unconventional configurations of bistable devices, as well as multistable designs with more than two stable equilibrium states, were also explored. Zhu and Beeby [56] proposed a coupled bistable structure, consisting of two cantilevers with a repelling force between them and subject to white noise vibrations with various average accelerations, which is capable of triggering bistable operation with a lower excitation force than conventional bistable and linear structures.

Hosseini and Turitsyn [57] presented a non-resonant harvester with adaptive bistable potential, able to surpass linear and conventional bistable counterparts when subject to both harmonic and non-stationary random-walk experimental excitations.

Kumar et al. [58] examined a model of a piezomagnetoelastic energy harvester capable of performing in the monostable, bistable, and tristable operating regimes and showed that bistable and tristable configurations are capable of harvesting more power while undergoing cross-well oscillations for certain values of excitation amplitude and frequencies.

All the abovementioned works on nonlinear energy harvesters refer to harvesting systems subject to direct or base excitation, mostly harmonic or random. Few works focused on a harvesting device directly excited by impulsive forces, which,

however, represent an important subset of the ambient vibration sources (including human activities such as walking or jumping, and automobiles driven over traffic counters or speed bumps, to cite but a few examples) [59, 47]. Bistable energy harvesters turn out to be particularly sensitive to impulsive excitations [60, 61]. Harne et al. [62] developed a predictive strategy to determine the power generation performance of a bistable piezoelectric cantilever resulting from the favorable snap-through oscillations induced by applied impulses.

2.3 Exploiting targeted energy transfer (TET)

Energy harvesting systems are commonly applied to vibrating structures, including civil structures, like bridges, or industrial machines. Hence, more recently, nonlinear harvesters coupled to a directly loaded host structure have been investigated, in order to evaluate the dynamic interaction and energy exchanges between the two subsystems. In these systems, vibration energy harvesting can be achieved through the passive nonlinear targeted energy transfer (TET) technique, which allows irreversible transfer of transient vibration energy from the primary system to the nonlinear local attachment, mainly by means of internal resonances and nonlinear mode localization [13], and eventually converts mechanical vibration energy into electrical energy.

Since the seminal work by Vakakis, Gendelman et al. [63, 64, 65, 66], due to its various and numerous applications, starting from vibration absorbtion (shock isolation, seismic mitigation and self-excited instabilities suppression) [12], the problem of passive nonlinear energy transfer (TET) has become a subject of growing interest. In this context, the dynamics of a linear structure weakly coupled to a local nonlinear attachment possessing essential stiffness nonlinearity was thoroughly studied. It was shown that under certain conditions this type of essentially nonlinear attachment can passively absorb energy from a linear non-conservative (damped) structure, in essence, acting as nonlinear energy sink (NES). Indeed, the addition to a linear system of a local attachment possessing essential (nonlinearizable)

stiffness nonlinearity may significantly alter the global dynamics of the resulting integrated system. This is because of the lack of a preferential resonance frequency of the attachment (it has no linear stiffness term), which, in principle, enables it to generate a countably infinite number of non-linear resonance conditions (i.e. $m\omega_{primary} = n\omega_{NES}$, with m and n integers), through which vigorous energy exchanges occur between the two oscillators and, possibly, energy localization. Resonance interactions between the two sub-systems over broad frequency bands can lead to interesting resonance capture, a transient dynamical phenomenon whereby the trajectory of the dynamical system is captured in the domain of attraction on the resonance manifold. It is such resonance capture that triggers energy pumping phenomena, whereby a one-way, irreversible transfer of energy, from the linear structure to the attachment occurs. In other words, externally imparted energy in the linear system gets transferred to the non-linear attachment in a one-way, irreversible fashion. Energy localization to the nonlinear attachment is sought in order to attain efficient energy harvesting.

A paradigmatic example is provided by the essential nonlinear coupling of a weakly damped primary linear oscillator (LO) to an ungrounded lightweight, weakly damped NES, thoroughly analyzed by many authors within the context of energy absorption. The frequency-energy plot (FEP) depicting the periodic orbits of the corresponding Hamiltonian system is plotted in Figure 2.17. The backbones of the FEP are formed by nonlinear normal mode (NNM) branches on which the system response consists of in- and out-of-phase synchronous vibrations of the two masses (respectively, $S11+$ and $S11-$). These NNMs are nonlinear continuations of the in-phase and out-of-phase linear normal modes of the corresponding two degree-of-freedom linear system. In addition, there is a sequence of higher- and lower-frequency branches of subharmonic tongues $Snm\pm$ and $Unm\pm$ with $m \neq n$, that bifurcate out from the backbone branches. Each tongue occurs in the neighborhood of an internal resonance between the LO and the NES, meaning that the NES is capable of engaging in every possible $n : m$ internal resonance with the LO.

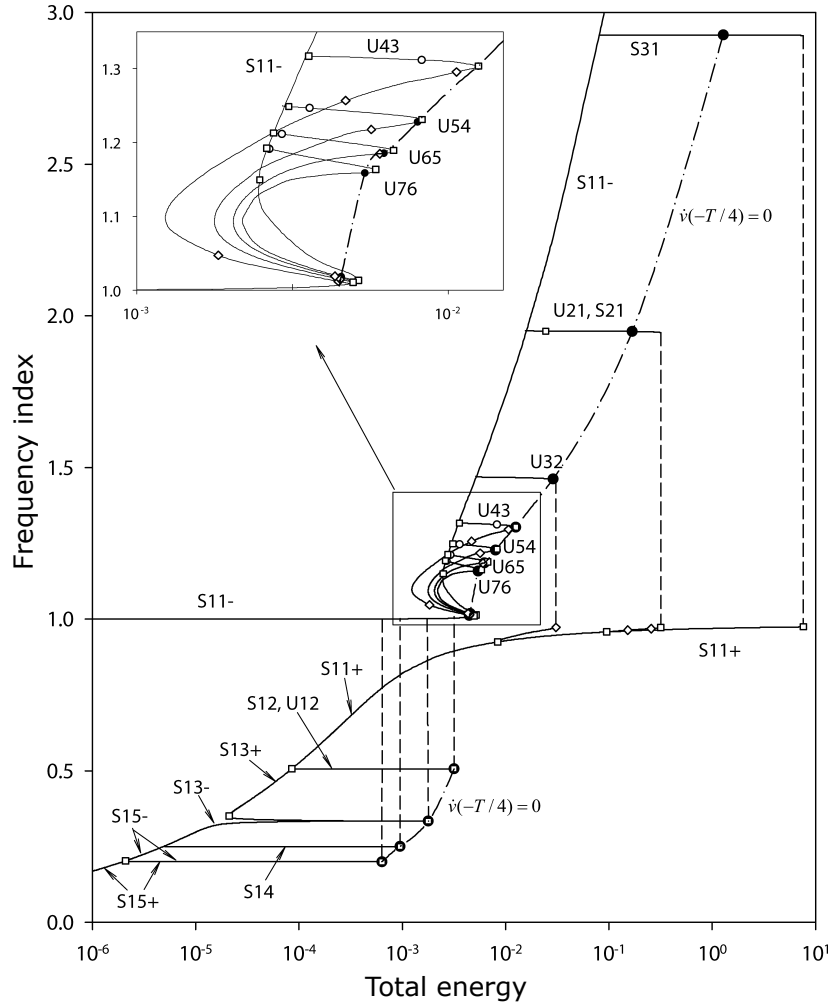


Figure 2.17: FEP of the periodic orbits of the Hamiltonian system (impulsive orbits: (●), bifurcation points: (+) when four Floquet multipliers are equal to +1 and (○) when two Floquet multipliers are equal to +1 and two to -1) [12].

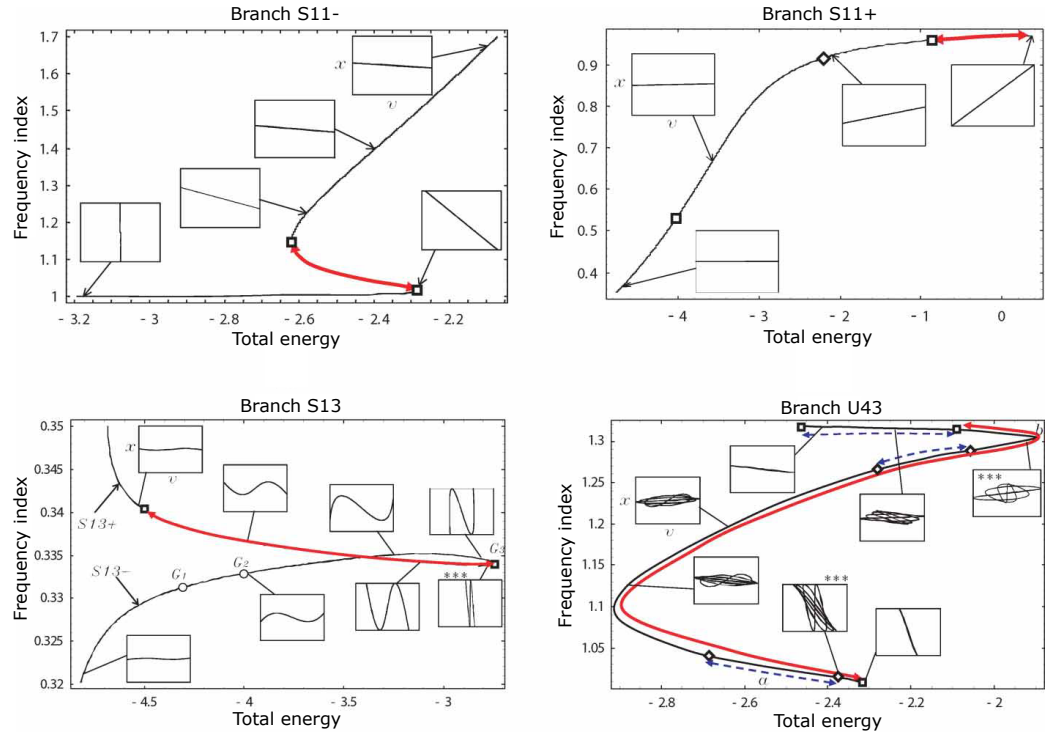


Figure 2.18: Close-ups of particular branches in the frequency index–logarithm of energy plane [12].

Figure 2.18 depicts some close-ups of the FEP, whereby the insets in the graphs display the periodic orbits in the configuration plane, with displacement of the NES and LO on the horizontal and vertical axis respectively, in the same scale. The portions of the curves marked as red refer to the unstable parts of the branches. The inset clearly show where the motion is localized into the NES (nearly horizontal curves). Without going through the analytical approach and demonstration of occurrence of irreversible energy transfer mechanisms (see [13] for detailed explanation), three types of efficient targeted energy transfer mechanisms are detected from the investigation of the complex dynamics of this coupled system: fundamental TET, occurring when the motion takes place along the backbone curve S11+ (1:1 resonance capture), subharmonic TET, when the motion takes place along a lower frequency branch Snm , $n < m \in \mathbb{Z}^+$, and TET initiated by nonlinear beats, which is based on the excitation of a special orbit with main frequency greater than the natural frequency of the linear oscillator. In particular,

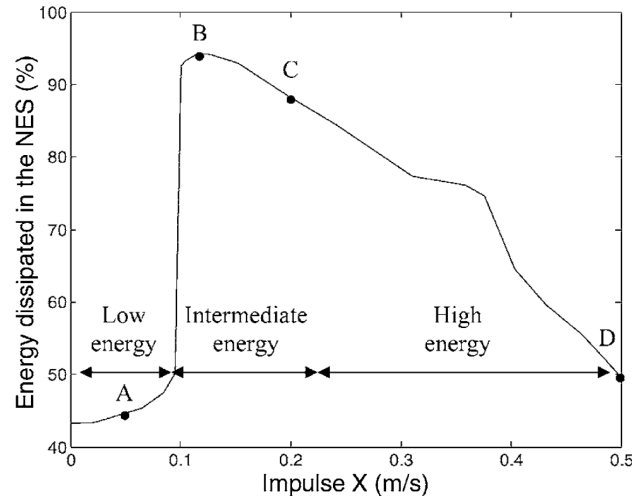


Figure 2.19: Percentage of impulsive energy eventually dissipated in the NES as a function of the magnitude of the impulse [13].

while the first two cannot be activated directly after the application of an impulsive excitation to the linear oscillator with the NES initially at rest, the latter can be initiated if the system is impulsively excited. It is also demonstrated the existence of a critical level of energy, which represents a lower bound below which no significant TET can be initiated when the LO is impulsively excited (Figure 2.19).

Based on this, some recent works are proposed in the context of energy harvesting. Kremer and Liu [67] proposed an electromechanical, two-degree-of-freedom system composed of a linear primary structure coupled to a nonlinear attachment through a nonlinear spring and electromagnetic coupling elements. The performance of the harvesting system when a base displacement was applied to the primary mass was evaluated, revealing the presence of a threshold before the NEH can be engaged. This threshold marks the beginning of 1:1 resonance and energy transfer. Remick et al. [68, 69] showed that, for an electromagnetic vibration energy harvester with a pure (nonlinearizable) geometric stiffness nonlinearity coupled to a grounded, damped linear primary oscillator (LO), under single or repetitive impulsive excitation of the linear oscillator, high-frequency transient dynamical instabilities in the damped response arise from transient resonance

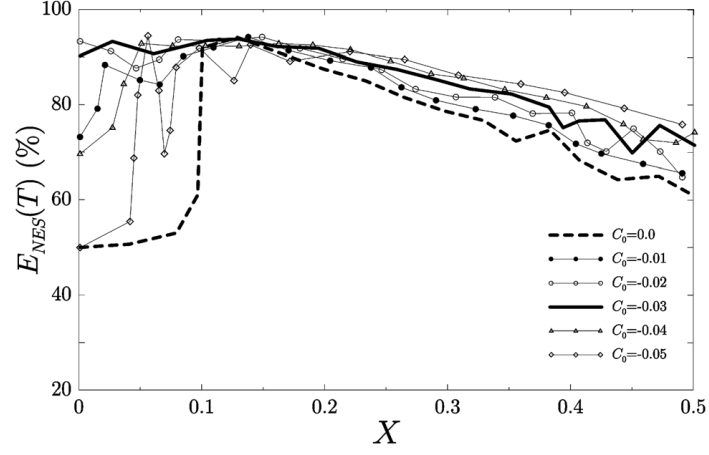


Figure 2.20: Percentage of impulsive energy dissipated in the NES as a function of the magnitude of the impulse, for varying negative stiffness (from [14]) Dashed line represents the monostable (purely cubic) system, whereas the thick solid line refers to the optimal value of the negative linear stiffness.

captures in the damped dynamics of the system, for sufficiently high levels of input energy. The high-frequency instability leads to high-amplitude oscillations of the nonlinear attachment, providing superior energy harvesting performance. Thus, it was confirmed that for an essentially nonlinear system a minimum input energy level is required for passive TET from the primary system to the coupled nonlinear device to occur and, hence, for efficient energy harvesting.

Although incorporating bistable nonlinear harvesting systems into linear primary systems has not been explored in the literature, recent analytical and numerical studies restricted to the TET context highlighted that the use of bistability in the coupling can break through the limit of the input energy threshold typical of the monostable nonlinear devices, producing an enhancement in the rapid passive energy absorption and local dissipation of broadband input energies (Figure 2.20) [70, 71, 14].

In particular, in [72] Romeo et al. investigated an impulsively excited, weakly damped, linear oscillator coupled to a light, bistable nonlinear energy sink (BNES) and showed that, in addition to the energy transfer mechanism of nonlinear beats, with high-amplitude periodic cross-well oscillations triggered by sufficiently high input energy, at a lower energy regime the presence of the negative stiffness

component gives rise to two further passive energy transfer mechanisms from the linear oscillator to the BNES, namely chaotic (aperiodic alternating in-well and cross-well) oscillations and secondary, in-well, nonlinear beats occurring at very low-energy level. Hence, this assures that a broadband efficient energy transfer is possible over a broad range of input energy. In that work, the nonlinear beats taking place within the in-well dynamics of the BNES are interpreted as Limiting Phase Trajectories (LPTs). LPTs (so called because they are trajectories representing an outer boundary for a set of trajectories encircling the basic stationary points, see [73]) represent special orbits characterized by strongly modulated oscillations during which maximum energy exchange between the oscillators occur. Figure 2.21 reports some results from [14], where TET mechanisms are distinguished based on the inspection of Poincaré sections constructed at four distinct input energy levels. Specifically, 1:1 in-phase and out-of-phase NNMs are detected for the highest energy condition, where the double-well configuration of the potential still do not come into play (Figure 2.21(a)). Primary LPT appears for the intermediate energy level: it separates the two regular regions encircling the 1:1 NNMs and corresponds to the most intense modulated oscillations that give rise to intense energy exchange between the linear oscillator and the BNES, as shown in the inset of Figure 2.21(b). As energy decreases, chaos starts to govern the dynamics of the system, which starts exhibiting alternating in-well and cross-well oscillations (Figure 2.21(c)). Here, only two classes of peculiar orbits arise in which the BNES performs periodic in-well and cross-well oscillations, with a 1:3 subharmonic oscillation. Finally, for very low level of the input energy (lower than the potential energy barrier), secondary LPTs separate the region of regular motion (quasi-periodic orbits) encircling two stationary points from the surrounding chaotic motion (Figure 2.21(d)). The two stationary points correspond to 1:1 resonance oscillations of the LO and the BNES, which oscillates within a well, while the secondary LPTs trigger the low amplitude, nonlinear beats with strong TET.

These results suggest the possibility of exploiting these additional energy transfer

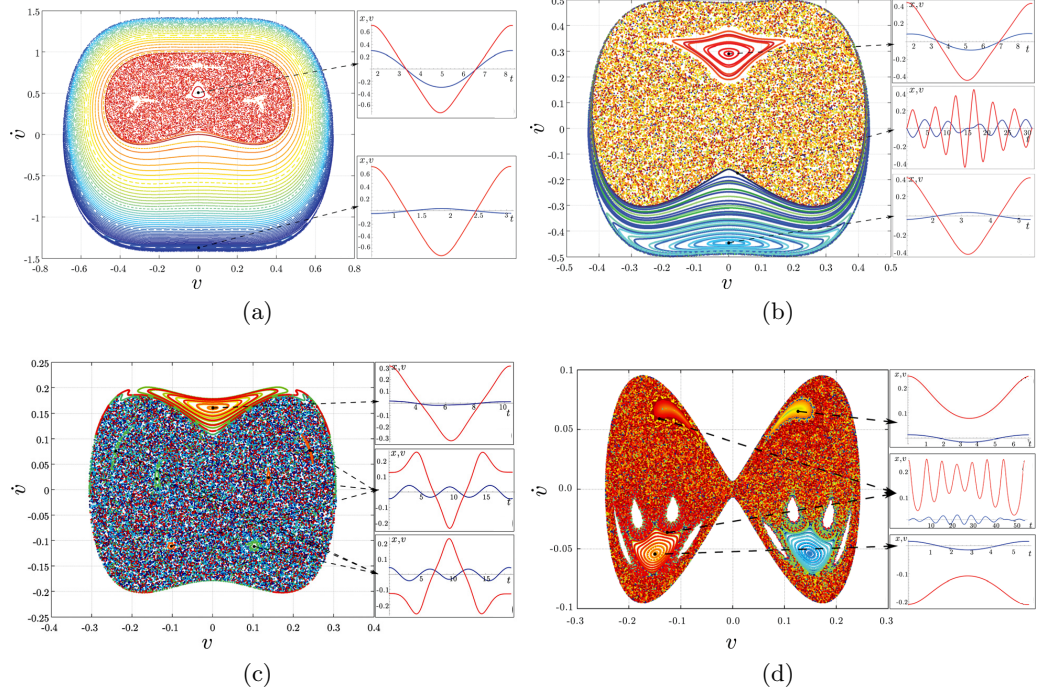


Figure 2.21: Poincaré sections of the bistable system investigated by [14]. Insets depict the displacement of the LO (blue) and BNES (red) of selected points on the Poincaré map.

mechanisms to efficiently harvest power from ambient vibrations, usually characterized by very low amplitudes.

2.4 Transduction mechanisms

The established transduction mechanisms for vibration-to-electricity conversion are piezoelectric, electromagnetic and electrostatic. The transducer can generate electricity from mechanical strain or relative displacement or velocity present within the system, depending upon the type of transducer. The use of active materials such as piezoelectrics is an obvious example that enables the strain to be directly converted into electrical energy. Electromagnetic and electrostatic transduction exploits the relative velocity or displacement that occurs within a generator. Each transduction mechanism has different characteristics such as damping effects, ease of use, scalability, and effectiveness. The power generated

varies greatly, according to device size, type, and input vibration parameters and the device sizes vary from the micro-scale (0.01 cm^3) to the macro-scale (75 cm^3) [74]. The efficiency of electromagnetic generators is dependant upon the design of the device. Assuming no size constraints, electromagnetic harvesting will be the most efficient because the coil can be large, with a high number of turns and low coil resistance (larger diameter of the wire) providing very high potential coupling factors. The efficiency of piezoelectric generators is fundamentally limited by the piezoelectric properties of the material whereas the efficiency of electrostatic generators varies with position and device design but, actually, is reduced by technical challenges relating to charging the electrodes, the separation distances and the amplitudes of displacement (achieving an efficiency as high as that of the other solutions requires impractically large amplitudes of displacement compared to the minimum capacitor separation gap). Thus, the suitability of each mechanism for any particular application depends largely on the operating environment and practical constraints of the design problem. A brief description of the main transduction methods is reported below.

2.4.1 Electrostatic energy harvesting

Electrostatic energy harvesters extract power by using mechanical vibrations to separate a set of fixed electrodes and a set of movable electrodes, charged electrostatically in opposite polarity, causing work to be done against the electrostatic attraction; the motion of the movable electrodes varies the capacitance between the two series of electrodes. A schematic of this type of device is depicted in Figure 2.22. The movable electrodes are attached to the inertial mass. The capacitance varies between maximum and minimum value. In general, these systems can work at constant charge or at constant voltage. If the charge on the capacitor is constrained, the voltage will increase as the capacitance decreases. Conversely, if the charge on the capacitor is constrained, charge will move from the capacitor to a storage device or to the load as the capacitance decreases. According to the movement

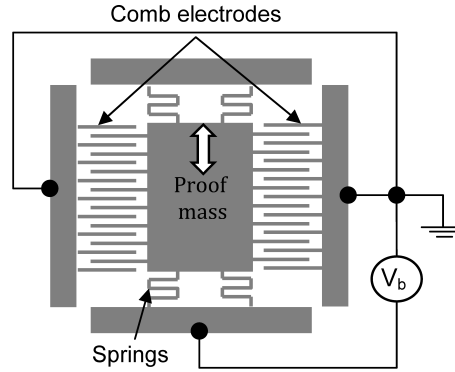


Figure 2.22: Schematic of an electrostatic energy harvester.

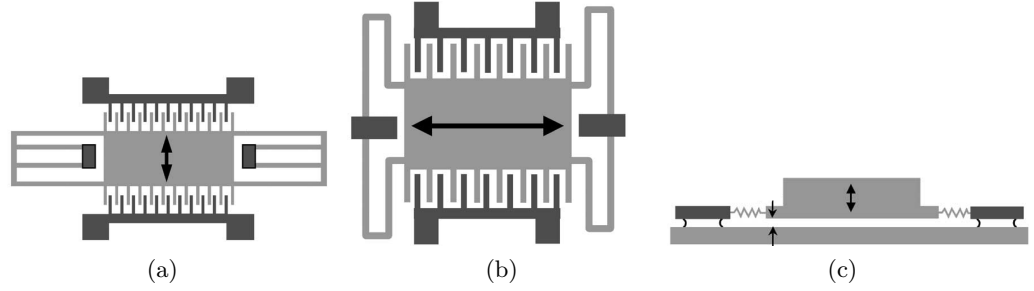


Figure 2.23: Three types of electrostatic energy harvesters: In-Plane Overlap (a); In-Plane Gap Closing (b); Out-of-Plane Gap Closing (c).

direction of the capacitor plates, electrostatic energy harvesters can be classified into three types, as shown in Figure 2.23, i.e. in-plane overlap type which varies the overlap area between electrodes, in-plane gap closing type which varies the gap between electrodes and out-of-plane gap type which varies the gap between two large electrode plates [20]. Roundy in [38] provides an exhaustive description and comparison of each of the three types. Electrostatic energy harvesters have high output voltage level and low output current. Their primary disadvantage is that they require an implanted charge or an external direct current (dc) voltage source to initiate the conversion process. The voltage output of electrostatic devices can be determined in a fairly arbitrary manner by specifying the initial charge up voltage. However, the current output of electrostatic devices depends on the capacitance, therefore, larger devices, with larger capacitances, provide

higher currents. The power density of electrostatic energy harvesters is much lower than that of the other two types of vibration energy harvesters. However, dimensions of electrostatic energy harvesters are normally small which make them well suited to microelectromechanical (MEMS) implementation. The great advantage of electrostatic converters is that MEMS processing technology offers an effective method to obtain close integration with electronics. Maximum capacitance is a critical parameter for this type of transducers because current, not voltage, will scale down with size because the capacitance of device in general decreases with decreasing size. They are also very sensitive to the minimum allowable capacitor gap. To design a generator with high power output, the range of motion of the generator must be hundreds of times greater than the minimum capacitor gap. This represents a practical implementation difficulty. The constitutive equations for electrostatic transducers depend heavily on the geometry and operating conditions (e.g., constant voltage or constant charge). Their efficiency is affected by technical challenges relating to charging the electrodes, the separation distances, and the amplitudes of displacement. Finally, generating a level of power comparable to other technologies with electrostatic generators requires that the device oscillates at a magnitude of hundreds of microns while maintaining a minimum capacitive air gap of 0.5 mm or less. This configuration presents practical implementation and stability issues.

2.4.2 Piezoelectric energy harvesting

Piezoelectric materials offer a simple approach to kinetic energy harvesting, whereby vibratory mechanical input energy is directly converted into electrical energy by using an appropriate type of piezoelectric material and associated electrodes. Piezoelectricity was first discovered in 1880 by Pierre and Jacques Curie. Their research revealed a coupled linear relationship between mechanical stress and electrical charge in crystalline material. This relationship is directly due to the crystal structure of the material. In particular, the direct piezoelectric effect,

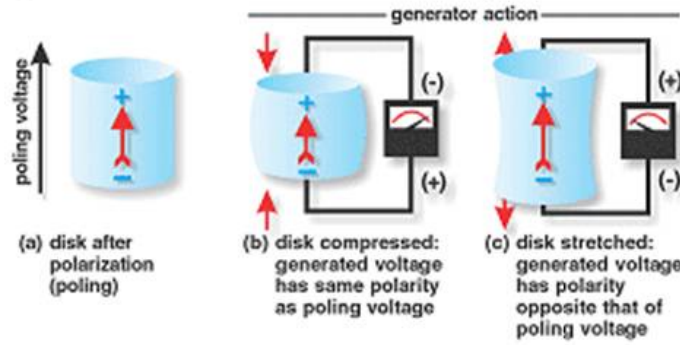


Figure 2.24: Schematic of direct piezoelectric effect; (a) piezoelectric material, (b) voltage generation under tension, (c) voltage generation under compression [15].

used for energy harvesting, refers to the change in electric polarization, that is to say the internal generation of electrical charge and consequently an electric potential, produced in the material in response of an applied mechanical stress. According to the definition of "direct piezoelectric effect", when a mechanical strain is applied to crystals by an external stress, an electric charge occurs on the surfaces of the crystal and the polarity of this observed electric charge on the surfaces can be reversed by reversing the direction of the mechanical strain applied [75]: compression along the direction of polarization, or tension perpendicular to the direction of polarization, generates voltage of the same polarity as the poling voltage, whereas tension along the direction of polarization, or compression perpendicular to the direction of polarization, generates a voltage with polarity opposite that of the poling voltage, as shown in Figure 2.24. The strain and coupling coefficients in the fundamental piezoelectric equations are in general much higher in 33 mode than in 31. However the 33 mode of bulk crystal corresponds to very high natural frequencies (~ 1 to 100 kHz), while longitudinal strain is easily produced within a cantilever beam that resonates at lower frequencies (~ 100 Hz) [76]. The electromechanical coupling produced from these crystals is physically realized in the mechanical system as a stiffness term with structural-like damping behavior, in which performance is thus proportional to displacement. The piezo-constitutive law dictates how stress and strain are related to electric charge density and electric field

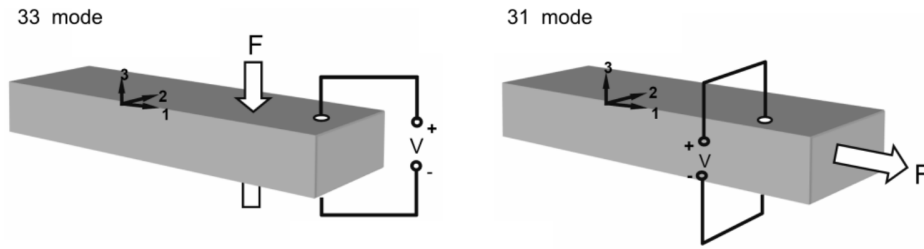


Figure 2.25: Direct piezoelectric effect with 33 and 31 strain-charge coupling.

strength, respectively, via the material parameters. The piezoelectric parameters are inherent to the material selected, making them not easily tunable or designable. There is a wide choice of piezoelectric materials available for different application environments. Commonly used piezoelectric materials are natural materials such as quartz, tourmaline etc., which, however, exhibit a limited piezoelectric effect in terms of usable power, and man-made polycrystalline ferroelectric ceramic materials such as barium titanate (BaTiO_3) and lead zirconate titanate (PZT) or piezopolymers (PVDF) with improved properties. The achievable induced strains and properties inherent to the crystalline material primarily determines coupling effectiveness. Maximization of the product of the piezoelectric voltage constant and the piezoelectric strain constant is paramount for suitable material selection for vibration energy harvesting, which serves to maximize the electromechanical coupling.

Piezoelectric elements are preferable for high frequency applications based on cantilever beam configuration, typically with a mass at the unattached end of the lever (Figure 2.26). Other harvesting schemes using piezoelectric elements include membrane structures to harvest energy from pulsing pressure sources or walking [33].

One particular advantage of this transduction principle is that piezoelectrics are well suited to microengineering (MEMS), where, due to size constraints imposed by cost, construction, and placement, they typically operate on a power scale of the order of microwatt [16, 77], that is a smaller power scale relative to the capability of electromagnetic harvesting elements; however, microscale limitations imposed

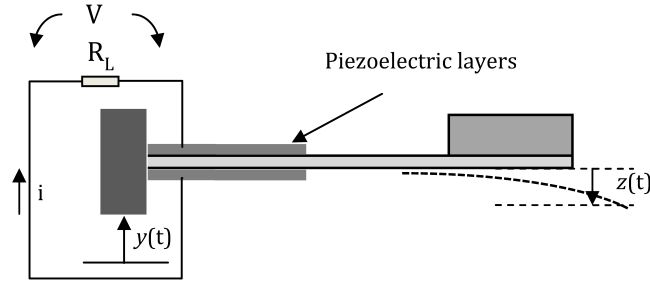


Figure 2.26: Schematic of bimorph piezoelectric cantilever beam.

on electromagnetic systems are no valid for piezoelectric systems. This trade-off is an important consideration when determining the scale of the device needed in the application environment.

Piezoelectrics are characterized by their ability to produce a relatively high voltage output but only at low electrical currents. The output impedance of piezoelectric generators is typically very high ($> 100k\Omega$). The actual voltage and current outputs for a given power output depend on the type of converter structure used. Increasing the volume of piezoelectric material can either increase the voltage or the current produced depending on the way in which the volume of material is increased. However, as low voltage is rarely a problem for this type of converters, we can say that increasing the volume will generally increase the current from the device. The piezoelectric materials need to be strained directly, and therefore their mechanical properties will limit their overall performance and lifetime. Additionally, the transduction efficiency is ultimately limited by the piezoelectric properties of the chosen material. Piezoelectric transducers are relatively easy to fabricate and can be used in both direct force and impact-coupled harvesting applications.

These coupling elements have been widely studied and utilized in the literature for small- and micro-scale vibration energy harvesting. Wang [16] numerically and experimentally investigates a nonlinear device based on the traditional cantilever beam configuration with time-varying potential energy function, to scavenge energy from human lower-limb motion (Figure 2.27(a)). The author reports a maximum energy harvesting capability on the scale of 30 mW for a human motion speed of

7 – 8 km/h. Mak et al. [17] use a traditional linear cantilever beam setup with nonlinearity induced via a vibro-impact bump stop and piezoelectric layers, as in Figure 2.27(b). The harvester is embedded within a car tyre as a means of feeding a tyre pressure monitoring system. The bump stop impacts the beam when it is excited at a sufficient magnitude, causing the beam to vibrate at higher frequencies. The system is investigated under various velocities of the car: the peak power output is of the order of magnitude of 10 mW, corresponding to the impact of the beam to the stop, with a car speed of 65 km/h. An energy harvesting system, consisting of a piezoelectric (PZT) stack and a proof mass as shown in Figure 2.27(c)), is proposed in [18] to evaluate the effect of an excitation with time-varying frequency on the response of the linear energy harvester. The output power of the given dimensional system in the fixed-frequency case was analytically found to be 3.5 mW under harmonic excitation of amplitude 1 N. Pan et al. [19] place several patches of piezoelectric ceramics on a bi-stable hybrid composite plate and test it under sinusoidal excitation. The output power was measured at different frequencies and g-level accelerations: about 20 mW was harvested at 2 g.

2.4.3 Electromagnetic energy harvesting

The conversion of kinetic energy into electricity using electromagnetic induction exploits the well-known Faraday's law (1831), which states the proportionality of the electromotive force induced in a circuit to the time rate change of the magnetic flux linkage. The relative motion generates an induced voltage (or induced emf) in the coil, proportional to the rate of change in time of the magnetic flux passing through the coil, and the induced current flowing through the coil creates, in turn, its own magnetic field that opposes the field created by the permanent magnet. The interaction between the two magnetic fields results in an electromagnetic force which opposes the motion, allowing the conversion of the mechanical energy into electrical energy, as better explained in Section 3.3. The principle was first applied to electrical energy generation in the early 1930s, when rotational generators were

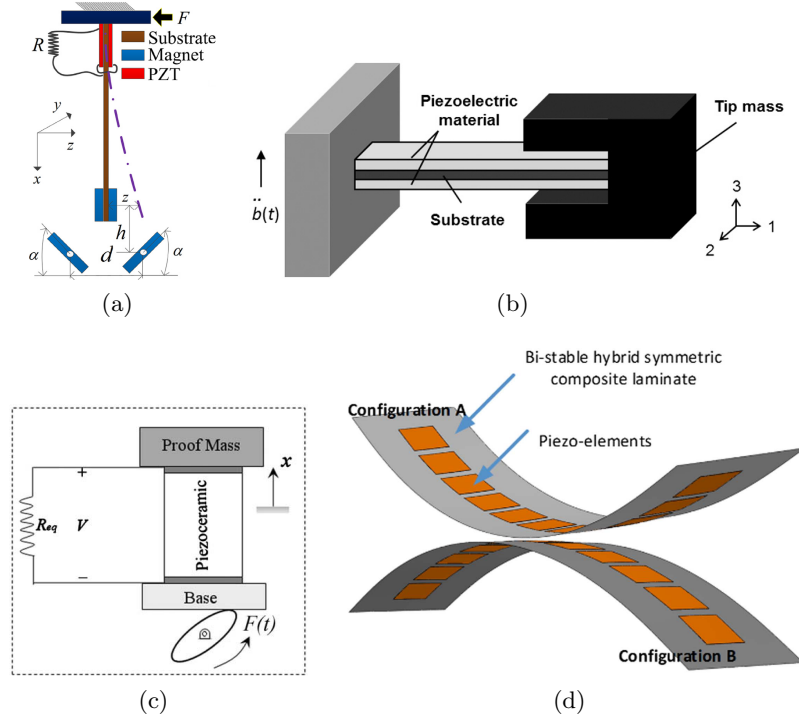


Figure 2.27: Piezoelectric energy harvesting systems: (a) [16] substrate layer 0.26 cm^3 ; (b) [17] cantilever beam mass 0.20 g , tip mass 0.97 g ; (c) [18] mass 0.011 kg ; (d) [19] size $100 \times 40 \times 12 \text{ mm}$.

mechanically driven to produce small-scale power output. The electromagnetic technique is commonly realized by coupling a static magnetic field produced by a permanent magnet and a solenoid in relative motion with respect to the magnet. One of the two components usually acts as a stator and the other as a mover (Figure 2.28(a)). In most cases, the coil is fixed while the magnet is mobile, since the coil is fragile compared to the magnet and static coil can increase the lifetime of the device. The amount of electricity generated depends upon the strength of the magnetic field, the velocity of the relative motion and the properties of the coil (Figure 2.28(b)). As for the latter is concerned, the number of coil turns and the coil resistance are important parameters for determining the voltage and useful power developed by a generator. The number of turns is governed by the geometry of the coil, the diameter of the wire it is wound from and the density with which the coil wire has been wound. The permanent magnets can be realized with several

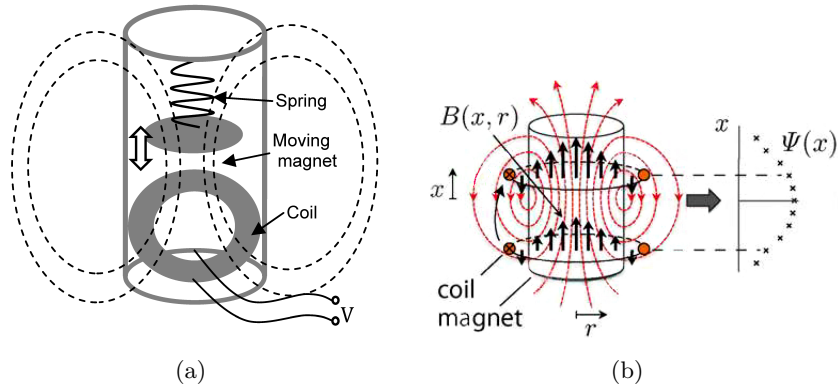


Figure 2.28: Scheme of an electromagnetic energy harvester (a) and of the electromagnetic induction(b).

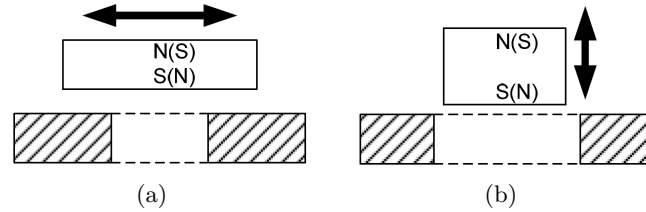


Figure 2.29: Two types of electromagnetic energy harvesters.

different materials, of which neodymium provides the strongest magnetic flux field density per volume.

Generally, there are two types of electromagnetic energy harvesters in terms of the relative displacement. The first type (Figure 2.29(a)) is based on the lateral movement between the magnet and the coil. The magnetic field cut by the coil varies with the relative movement between the magnet and the coil. In the second type, as shown in Figure 2.29(b), the magnet moves in and out of the coil. The magnetic field cut by the coil varies with the distance between the coil and the magnet. The first type is more common as it is able to provide better electromagnetic coupling [20]. As for piezoelectric transduction, electromagnetic induction does not require the device to have an initial bias voltage. Similarly, the oscillatory electrical response needs to be rectified and converted to a DC signal in order to charge a storage component. In contrast to piezoelectric transduction, instead, electromagnetic energy harvesting results in high current outputs (associated with a much lower

optimal circuit resistance as compared to piezoelectric energy harvesters) at the expense of low voltage . This means that electromagnetic converters can be scaled down in size at the cost of output voltage while piezoelectric and electrostatic converters can be scaled down only at the cost of current output. Low voltage output is frequently a problem for small converters.

Electromechanical transduction adapts to low to high frequency applications based on a variety of system configurations and has a wide operating scale spanning from micro to kilowatt [78, 7, 79], using both rotational and linear devices. They are usually recommended for lower frequencies ($2 - 20$ Hz), small impedance and medium size. An advantage consists in the high tunability of the coupling, which is dependent upon design parameters (type and size of permanent magnet, induction coil size). Advantages of this type of generator are their design simplicity, which makes them suitable for academic research laboratory activities, and, and their durability, as the harvester power generation depends on the relative velocity and change in magnetic flux, hence its amplitude is not limited by its fatigue strength, as, for example, for piezoelectric materials. Moreover, its costs less than other solutions. In general, the voltage magnitude of electromagnetic converters increases with device volume. Most of the commercial solutions are available at centimetre scales because they exhibit higher power density than piezoelectric devices. An increase in volume will increase the potential number of turns while keeping the area of each coil constant, thus increasing voltage. On the other hand, the integration of electromagnetic harvesters into micro-electro-mechanical-systems (MEMS) results difficult. In fact, minimization in scaling leads to vast efficiency reduction with the result of some design restrictions for micro-fabrication. The reason is that the induced electromotive force (EMF) decreases rapidly as the device size scales down. Figure 2.30 compares normalized power density of some reported electromagnetic vibration energy harvesters, highlighting that power density of macro-scaled electromagnetic vibration energy harvesters is much higher than that of micro-scaled devices. This proves analytical results presented by Beeby et al.

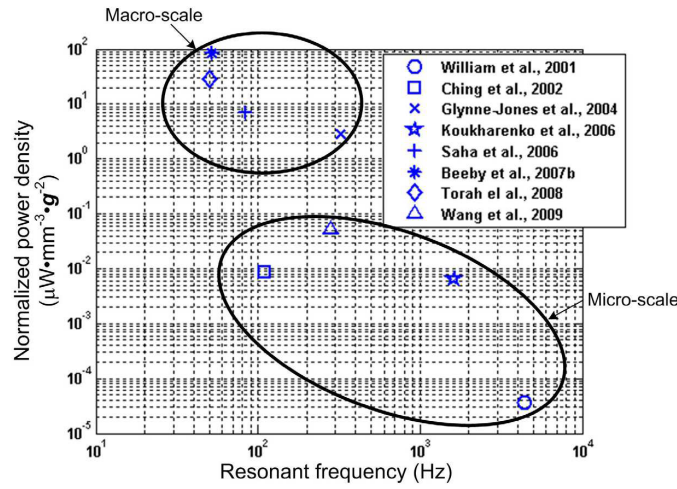


Figure 2.30: Normalized power density of some existing electromagnetic vibration energy harvesters [20].

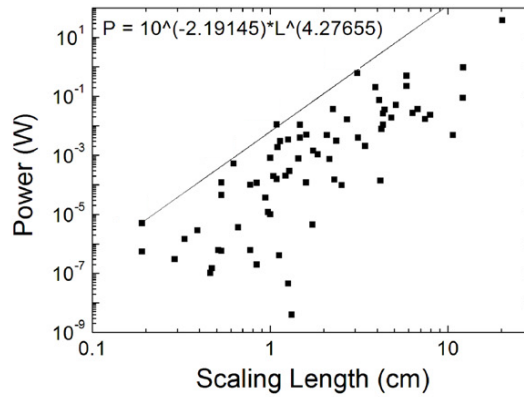


Figure 2.31: Power versus scaling length L (solid line corresponds to the line of best fit for upper limit of power) [21].

[80]. In Figure 2.31 the output power from some electromagnetic harvesters (into an electrical load) is plotted as a function of the scaling length $L = V^{1/3}$ with V the "active volume" of the device. However, micro-scale converters are still produced, typically using planar spiral micro-coils, as the one in Figure 2.32. Micro-coils are coils which are fabricated using photolithography techniques to define the coil pattern, most commonly on substrates such as silicon, flex substrates or printed circuit boards (PCBs) [81]. Thus, in general, assuming an electromagnetic generator correctly designed and not constrained in size, it is the most efficient converter of kinetic energy into electrical, because the coil can be large, with a high

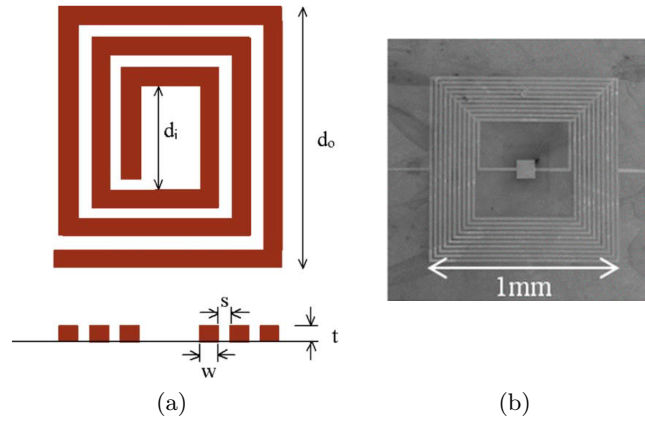


Figure 2.32: Micro-fabricated square spiral coil.

number of turns and low coil resistance (larger diameter wire) providing very high potential coupling factors. Attempts to miniaturise the technique, however, using micro-engineering technology to fabricate a generator, invariably reduce efficiency levels considerably.

These coupling elements have been utilized in a variety of configurations in the literature for small-scale vibration energy harvesting. A tunable electromagnetic energy harvester was proposed in [16]. Mann and Owens [22] investigate an electromagnetic-induction energy generator containing a moving magnet that is suspended in reference to an external housing with magnetic repulsion and a series of magnets that are positioned to make the system bistable (Figure 2.33(a)). Forward and reverse frequency sweep tests with an applied base harmonic excitation have been carried out and up to 100 mW with excitation amplitude of 8 m/s^2 . Ma and Zhang [23] use a rotational electromagnetic energy harvester based on a pendulum system with nonlinearity further induced via a potential well design (Figure 2.33(b)). The authors investigated this system for various harmonic excitation frequencies, circuit loads, and excitation magnitudes, resulting in power output on the scale of 0.5 – 3.0 mW while operating outside of the potential well. Energy harvesting technologies are particularly well suited for bridge applications, since these are structures prone to damage from repeated dynamic loading, that make excellent candidates for self-sustained SHM applications. Many recent studies

have examined the feasibility of using the low frequency vibrations of concrete and cable-stayed bridges to power SHM sensors. Jung et al. [24] conducted a field test on an in-service cable-stayed bridge using an electromagnetic energy harvester improved by introducing the combination of a motor and a gear part, as depicted in Figure 2.33(c). The prototype device produced a maximum of 15.46 mW of power when attached to the bridge's stay cable.

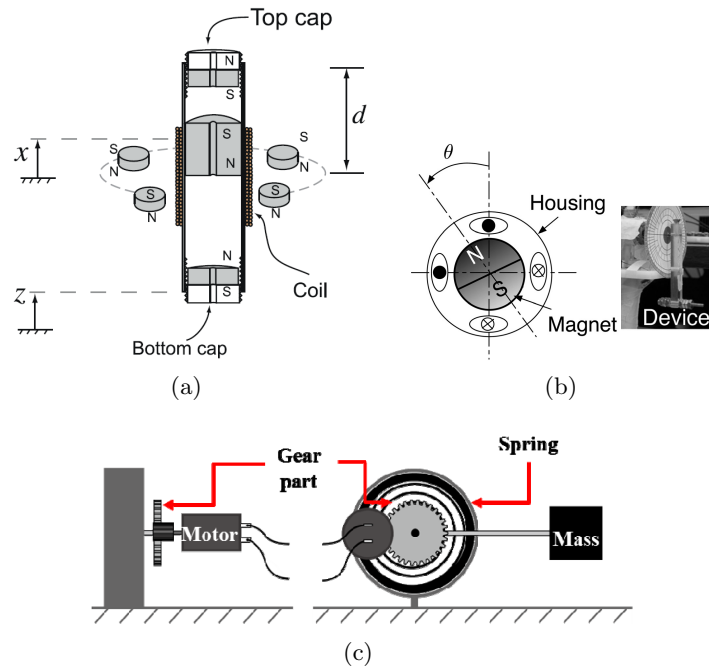


Figure 2.33: Electromagnetic energy harvesting systems: (a) [22] mass 35.6 g; (b) [23] acceleration approx. 200 mg. (c) [24], maximum stay cable acceleration 100 – 200 mg.

Chapter 3

Model of the electromechanically coupled system

In this chapter, the derivation of the mathematical model of the coupled system under investigation is presented and discussed. The model considers, for the electromechanical coupling, an electromagnetic transducer.

3.1 System modeling

The proposed energy harvesting system is modeled as a two degree-of-freedom system, composed of a grounded, weakly damped, linear primary oscillator of mass m_1 (the LO) that is coupled to a lightweight, damped, nonlinear oscillator of mass m_2 (the bistable nonlinear energy harvester, BNEH) by means of electromechanical coupling elements and an element which provides both cubic nonlinear and negative linear stiffness components. The sketch of the coupled-oscillator system under investigation is depicted in Figure 3.1.

It is here pointed out that the novelty of the presented system lies in the coupling

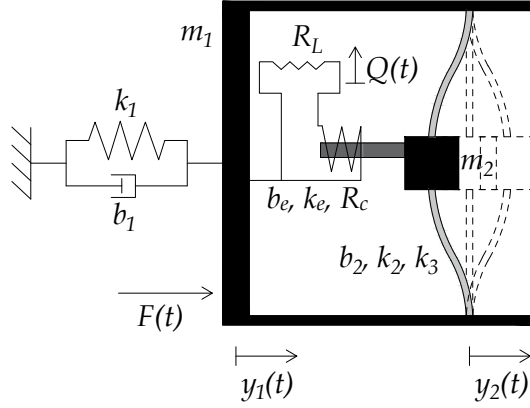


Figure 3.1: Model of the two coupled oscillators.

of the energy harvesting device to the main (linear) structure, which allows to account for the dynamic interaction of the two sub-structures.

The mechanical coupling is intended to add to the third-order stiffness nonlinearity a negative linear stiffness component. This can be achieved using a nonlinear structure possessing limit points in the equilibrium path such that, under a critical load value, a snap-through instability takes place. The von Mises truss, recalled in 2.2, is a paradigm for the mechanism of the snap-through, where two symmetric stable equilibrium states coalesce with the unstable one, producing a two-well potential energy. The snap-through instability causes a sudden jump of the trusses to a far-away stable configuration [82]. The bistability, i.e., the negative stiffness around the equilibrium position, is here realized by exploiting the buckling of a slender beam subjected to an axial compressive force and connected to the mass of the BNEH at its midspan. When the compressive force exceeds the critical load corresponding to the first mode of buckling, the beam buckles to one of the two possible buckled states [83]. The simplified one degree of freedom (dof) model that approximates the continuous model of beam is able to capture the main features of the physical harvesting device. Its derivation is described in Section 3.2, whereas Section 3.3 is devoted to modeling the electromechanical coupling.

3.2 Mechanical coupling modeling

3.2.1 Problem formulation and analytical solution of the clamped-clamped buckled beam

The analytical model of the harvesting system is derived according to the Euler-Bernoulli beam theory accounting for von Kármán nonlinear strains. The nonlinear problem of a post-buckled beam undergoing compressive axial force was extensively investigated in several works, including the more recent study of Nayfeh and Emam [84].

The transverse planar vibration of the clamped-clamped beam, subjected to a constant uniaxial compressive force of magnitude P and an external transverse load $\hat{F}(\hat{x}, \hat{t})$, is governed by the following partial differential equation of motion, including the effect of mid-plane stretching:

$$\rho A \frac{\partial^2 \hat{w}}{\partial \hat{t}^2} + EJ \frac{\partial^4 \hat{w}}{\partial \hat{x}^4} + \hat{\gamma} \frac{\partial \hat{w}}{\partial \hat{t}} + \left[\hat{P} - \frac{EA}{2L} \int_0^L \left(\frac{\partial \hat{w}}{\partial \hat{x}} \right)^2 d\hat{x} \right] \frac{\partial^2 \hat{w}}{\partial \hat{x}^2} = \hat{F}(\hat{x}, \hat{t}) \quad (3.1)$$

complemented by the following boundary conditions:

$$\begin{aligned} \hat{w}(0, \hat{t}) = 0, \quad \frac{\partial \hat{w}(\hat{x}, \hat{t})}{\partial \hat{x}} \Big|_{\hat{x}=0} &= 0 \\ \hat{w}(L, \hat{t}) = 0, \quad \frac{\partial \hat{w}(\hat{x}, \hat{t})}{\partial \hat{x}} \Big|_{\hat{x}=L} &= 0 \end{aligned} \quad (3.2)$$

where ρ is the mass per unit volume of the beam, $\hat{\gamma}$ the damping coefficient, E the modulus of elasticity, $J = bh^3/12$ the moment of inertia (being b the height and h the thickness of the beam), $A = bh$ and L the cross-sectional area and initial length of the straight beam, respectively. The transverse displacement is denoted by \hat{w} and is a function of the time \hat{t} and the spatial coordinate \hat{x} along the axis of the beam in its initial configuration. It is often convenient to express the problem in nondimensional form, by nondimensionalizing the spatial and time variables as

follows:

$$x = \frac{\hat{x}}{L}, \quad w = \frac{\hat{w}}{r}, \quad t = \hat{t} \sqrt{\frac{EJ}{\rho AL^4}}, \quad \omega = \hat{\omega} \sqrt{\frac{\rho AL^4}{EJ}} \quad (3.3)$$

where $r = \sqrt{J/A}$ is the radius of gyration of the cross-section. This nondimensionalization allows Equation (3.1) to have the simplest scaled form, written as:

$$\ddot{w} + w^{iv} + \gamma \dot{w} + \left(P - \frac{1}{2} \int_0^1 w'^2 dx \right) w'' = F(x, t) \quad (3.4)$$

$$w(0, t) = 0, \quad w'(x, t)|_{x=0} = 0, \quad w(1, t) = 0, \quad w'(x, t)|_{x=1} = 0 \quad (3.5)$$

where the overdot indicates the derivative with respect to time t and the prime indicates the derivative with respect to the spatial coordinate x . Also, the nondimensional quantities are:

$$P = \frac{\hat{P}L^2}{EJ}, \quad \gamma = \frac{\hat{\gamma}L^2}{\sqrt{\rho AEJ}}, \quad F = \frac{\hat{F}L^4}{rEJ} \quad (3.6)$$

The buckling problem is obtained from Equations (3.4) and (3.5) by dropping the time derivatives and the dynamic load, resulting in the following equations:

$$\psi^{iv} + \left(P - \frac{1}{2} \int_0^1 \psi'^2 dx \right) \psi'' = 0 \quad (3.7)$$

having denoted as $\psi(x)$ the static configuration associated to the compressive load P . The boundary conditions for the fixed-fixed beam are given by:

$$\psi = 0 \text{ and } \psi' = 0 \text{ at } x = 0 \text{ and } x = 1 \quad (3.8)$$

Since the integral in Equation (3.7) is a constant for a given $\psi(x)$, the term in brackets is constant, hence Equation (3.7) reduces to:

$$\psi^{iv} + \lambda^2 \psi'' = 0 \quad (3.9)$$

where

$$\lambda^2 = P - \frac{1}{2} \int_0^1 \psi'^2 dx \quad (3.10)$$

represents a nondimensional critical buckling load P_{cr} . The general solution of the forth-order differential equation (3.7) is of the form:

$$\psi(x) = c_1 + c_2 x + c_3 \cos \lambda x + c_4 \sin \lambda x \quad (3.11)$$

Satisfying the boundary conditions by substituting (3.11) in (3.8) yields a system of equations in c_i , $i = 1, 4$ and λ , representing the eigenvalue problem for λ , the characteristic equation of which is $2 - 2 \cos \lambda - \lambda \sin \lambda = 0$. The first four eigenvalues λ are found to be 2π , 8.9868, 4π and 15.4505 and the corresponding mode shapes are of the form:

$$\psi(x) = c \left[1 - \cos \lambda x - \frac{\lambda(1 - \cos \lambda)}{\lambda - \sin \lambda} x + \frac{1 - \cos \lambda}{\lambda - \sin \lambda} \sin \lambda x \right] \quad (3.12)$$

where c is a constant that can be defined by satisfying the condition (3.10) and is expressed as:

$$c = \pm 2 \sqrt{\frac{P}{\lambda^2} - 1} \quad (3.13)$$

Thus, for a given axial load P , the constant c corresponding to any eigenvalue λ can be determined and hence its corresponding buckled shape can be obtained. The former expression of $\psi(x)$ governs both symmetric and antisymmetric buckling shapes. It follows that the first four nondimensional critical buckling loads $P_{cr,i}$ are $4\pi^2$, $8.18\pi^2$, $16\pi^2$ and $24.19\pi^2$. The first buckling shape results in the simple expression:

$$\psi^{(1)}(x) = c(1 - \cos 2\pi x) \quad \text{with} \quad c^2 = \frac{P - P_{cr,1}}{\pi^2}, \quad P_{cr,1} = 4\pi^2 \quad (3.14)$$

When the axial load exceeds the first critical buckling load, the straight position loses stability and the beam buckles. As the axial load is increased beyond

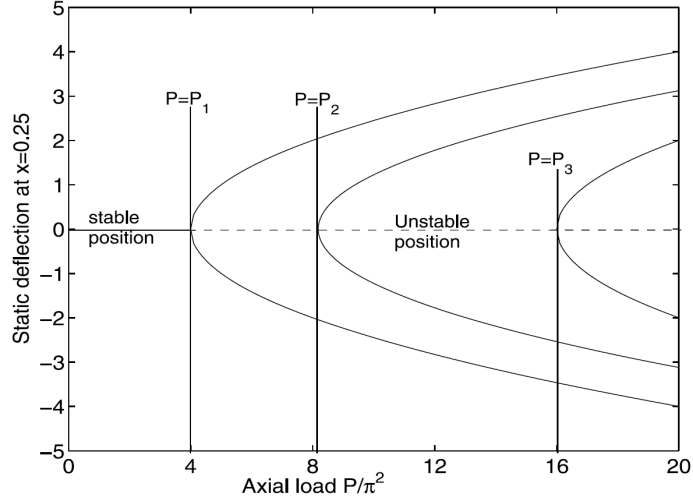


Figure 3.2: Bifurcation diagram for the static deflection of the fixed-fixed beam at $x = 0.25$ with the axial load. P_1 , P_2 , P_3 are the first three critical loads.

the second critical buckling load, the beam has three equilibria: the straight configuration, which is unstable, and two nontrivial equilibria, corresponding to the first and second buckled configurations, and so forth (Figure 3.2). The first buckled configuration is a stable equilibrium position, whereas buckled configurations beyond the first buckling mode are unstable equilibrium positions [84]. As a consequence, when the applied axial load goes beyond the second buckling load, the beam exhibits stable and unstable equilibrium positions, with the result of a rich and complex dynamics. To study the dynamical problem of the beam around the buckled configuration, the total deflection can be defined as the summation of the post-buckling static deflection and the time-dependent displacement $v(x, t)$ around the initial equilibrium configuration, namely $w(x, t) = \psi(x) + v(x, t)$. Substitution into (3.4) and (3.5) leads to the following equations:

$$\ddot{v} + v^{iv} + \gamma \dot{v} + \lambda^2 v'' = \left(\int_0^1 \psi' v' dx + \frac{1}{2} \int_0^1 v'^2 dx \right) (\psi'' + v'') + F \quad (3.15)$$

$$v(0, t) = 0, \quad v'(x, t)|_{x=0} = 0, \quad v(1, t) = 0, \quad v'(x, t)|_{x=1} = 0 \quad (3.16)$$

Equation (3.15) possesses both quadratic and cubic nonlinearities due to the change

of variable in v . Since there are no restrictions on v to be small, (3.15) governs the global dynamics of the buckled beam, around the two buckled configurations. The nonlinear dynamical problem of distributed-parameter systems can be solved through an approximate analytical approach consisting in finite-degree-of-freedom discretization technique, which replaces the distributed-parameter system by a set of nonlinearly coupled ordinary differential equations. Either the spatial or the temporal form of the solution is assumed a priori. The Galerkin method is commonly used for a spatial discretization and a truncated set of eigenfunctions of the linearized problem are usually taken as the trial functions. Hence, according to the multi-mode Galerkin-type discretization, the solution is written in the form:

$$v(x, t) = \sum_{n=1}^N \phi_n(x) q_n(t) \quad (3.17)$$

where N is the number of the retained modes, $\phi_n(x)$ is the n^{th} linear vibration mode shape of the buckled beam and $q_n(t)$ is the n th generalized coordinate. The eigenvalue problem for the natural frequencies and mode shapes can be obtained by dropping the nonlinear, damping, and forcing terms from Equation (3.15) and letting $v(x, t) = \phi(x)e^{i\omega t}$, being ω the natural frequency and $\phi(x)$ its corresponding linear vibration mode shape. The resulting linear free vibration problem is:

$$\phi^{iv} + \lambda^2 \phi'' = \psi'' \int_0^1 \psi' \phi' dx \quad (3.18)$$

$$\phi = 0 \text{ and } \phi' = 0 \text{ at } x = 0 \text{ and } x = 1 \quad (3.19)$$

The general solution is given by the summation of a homogeneous solution and the particular solution, as:

$$\phi(x) = d_1 \sin s_1 x + d_2 \cos s_1 x + d_3 \sinh s_2 x + d_4 \cosh s_2 x + d_5 \psi'' \quad (3.20)$$

where the d_i , $i = 1, \dots, 5$ are constants and:

$$s_{1,2} = \frac{1}{2} \left[\pm \lambda^2 + \sqrt{\lambda^2 + 4\omega^2} \right] \quad (3.21)$$

Solving this eigenvalue problem yields the natural frequencies ω and their corresponding vibration mode shapes ϕ around a buckled configuration ψ due to a given axial load P . The eigenmodes satisfy the orthonormality condition $\int_0^1 \phi_i \phi_j dx = \delta_{ij}$, where δ_{ij} is the Kronecker delta. Figure 3.3(a) shows variation of the lowest four nondimensional natural frequencies around the first buckled configuration, with the nondimensional buckling level [85]. The latter is the rise of the beam at its midspan b , related to the axial load by the relationship $b = 2c = \pm 4\sqrt{\frac{P}{\lambda^2} - 1}$. From Figure 3.3(a) it can be seen that buckled beams possess several internal resonances that can be activated at different buckling levels. The variation of the first four natural frequencies for the first, second and third buckling shapes with the axial load P is depicted in Figure 3.3(b). Odd vibration modes, indicated by solid lines, depend on the applied axial load (or, equivalently, on the initial buckled deflection), whereas even modes, represented by dotted lines, do not depend on the axial load. From Figure 3.3(b) it becomes apparent that many internal resonances might be activated among vibration modes not only around the same buckled configuration, but also around different buckled configurations [84]. Substituting (3.17) into (3.15) and applying the expansion theorem (multiplying by ϕ_m and integrating over the domain) leads to a set of equations for $q_m(t)$, as follows:

$$\ddot{q}_m + \gamma \dot{q}_m + \omega_m^2 q_m = \sum_{i=1}^N \sum_{j=1}^N \mathcal{Q}_{mij} q_i q_j + \sum_{i=1}^N \sum_{j=1}^N \sum_{k=1}^N \mathcal{T}_{mijk} q_i q_j q_k + f_m(t), \quad m = 1, \dots, N \quad (3.22)$$

where

$$\begin{aligned} \mathcal{Q}_{mij} &= \int_0^1 \psi'' \phi_m dx \int_0^1 \phi'_i \phi'_j dx + \int_0^1 \phi''_i \phi_m dx \int_0^1 \psi' \phi'_j dx \\ \mathcal{T}_{mij} &= \int_0^1 \phi''_i \phi_m dx \int_0^1 \phi'_j \phi'_k dx \end{aligned} \quad (3.23)$$

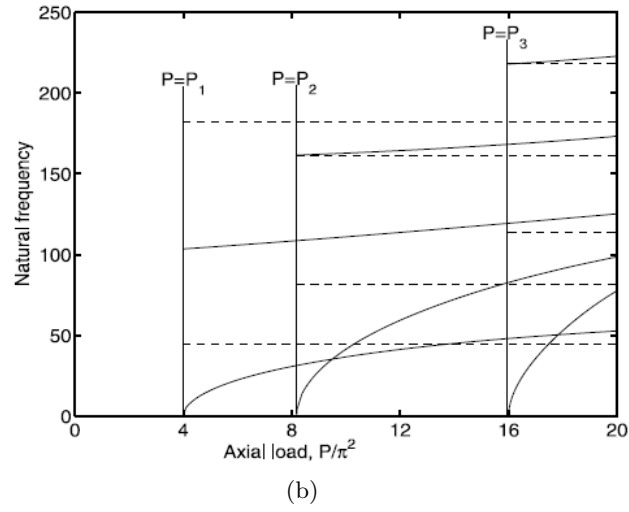
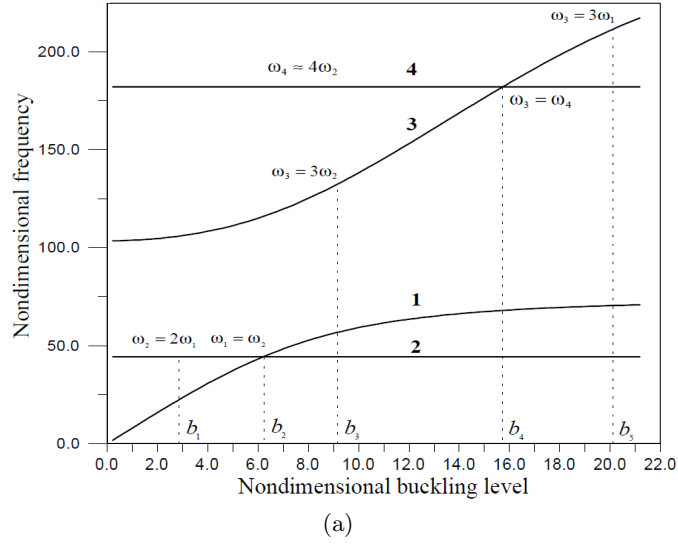


Figure 3.3: Variation of the first four natural frequencies around the lowest three buckling shapes with the axial load (a) and around the first buckled configuration with the nondimensional buckling level

are the coefficients of the quadratic and cubic nonlinearities, respectively, and

$$f_m(t) = \int_0^1 \phi_m F(x, t) dx \quad (3.24)$$

is the projection of the external force on the m th mode. The reduction of the problem to single-mode approximation is reported in the next subsection.

3.2.2 Single-mode approximation of the harvester's dynamics

A single-mode discretization can be obtained letting $v(x, t) = \phi_n(x)q_n(t)$ in Equation (3.15), multiplying the result with $\phi_n(x)$ and integrating from $x = 0$ to $x = 1$. The result is:

$$\ddot{q}_n + \gamma \dot{q}_n + \omega_n^2 q_n = \alpha_2 q_n^2 + \alpha_3 q_n^3 + f_n(t) \quad (3.25)$$

where:

$$\begin{aligned} \alpha_2 &= \int_0^1 \psi'' \phi_n dx \int_0^1 (\phi_n')^2 dx + \int_0^1 \phi_n \phi_n'' dx \int_0^1 \psi' \phi_n' dx \\ \alpha_3 &= \int_0^1 \phi_n \phi_n'' dx \int_0^1 (\phi_n')^2 dx \end{aligned} \quad (3.26)$$

and $f_n(t)$ expressed by (3.24) for $n = m$. For a fixed-fixed beam, ω_n , α_2 and α_3 are not available in simple form.

To study the forced vibration of buckled beams, it is a common practice to assume as trial functions only the eigenmodes that are directly or indirectly excited. In particular, if a system is excited near the natural frequency of a specific linear mode and that mode is not involved in an internal resonance with any other modes, only that mode is assumed in the expansion, regardless of the conditions under which such a projection from an infinite-dimensional space to a finite-dimensional space is performed. Such an approach is referred to as single-mode discretization [86]. The discretization approach for the clamped-clamped beam may yield erroneous results in some ranges of buckling level, such as internal resonances and for high levels of buckling, and this is confirmed by comparison with direct approach [87]. The reason is that the shape of the motion is fixed a priori and the nonlinear motion is

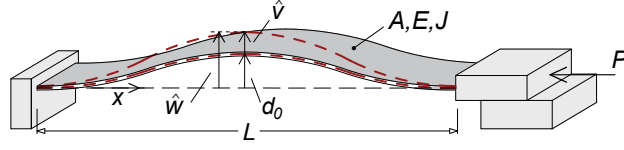


Figure 3.4: Sketch of the buckled beam.

postulated as separable in space and time. Therefore, the spatial nonstationarity of the actual nonlinear motion is neglected a priori. Hence, some calculated intrinsic system properties, such as the nonlinearity coefficient (cfr. [88]), which depend on the spatial variation, can be affected by the single-mode approximation. Thus, care must be taken when using a single-mode discretization in analyzing the possible issues related to the current buckling level of the beam.

Nevertheless, existing theoretical predictions of the nonlinear response of buckled beams to harmonic excitations are based on a single-mode Galerkin discretization of the governing partial differential equation and boundary conditions. Such this single-mode approximation is useful to characterize the mechanical features of a simple mechanical system and to provide insights on the dynamical behaviour. It is a common practice, then, to complement the analytical results with experimental data or finite element models to adjust the mechanical parameters of the buckled beam [89].

A dimensional approach for the one degree-of-freedom model is proposed below. The problem formulation is written with reference to the straight configuration, unstable position of the buckled beam, where the governing equation takes the form of a Duffing-type oscillator with negative linear coefficient (Figure 3.4). To study the dynamical problem of the beam around the buckled configuration, the total deflection can be defined as the summation of the post-buckling static deflection and the time-dependent displacement $\hat{v}(\hat{x}, \hat{t})$ around the initial equilibrium configuration, namely $\hat{w}(\hat{x}, \hat{t}) = d_0\psi(\hat{x}) + \hat{v}(\hat{x}, \hat{t})$, where $\psi(\hat{x})$ is the first buckling mode shape and $d_0 = \hat{w}(L/2, 0)$ is the rise at the midspan of the beam. The first buckling mode shape and its corresponding Euler's load, solution of the buckling problem

obtained from Equation (3.1) by dropping the time derivatives and the dynamic load, are given by:

$$\psi(\hat{x}) = \frac{1}{2} \left(1 - \cos 2\pi \frac{\hat{x}}{L} \right) \quad \text{and} \quad \hat{P}_{cr} = 4\pi^2 \frac{EJ}{L^2} \quad (3.27)$$

where $\psi(\hat{x})$ is normalized so that $\psi(L/2) = 1$; thus the post-buckling deflection is described by:

$$\hat{w}_s(\hat{x}) = d_0 \psi(\hat{x}) = \frac{1}{2} d_0 \left(1 - \cos 2\pi \frac{\hat{x}}{L} \right) \quad (3.28)$$

Substituting (3.28) into the equation of the buckling problem, which is given by:

$$EJ \frac{\partial^4 \hat{w}_s}{\partial \hat{x}^4} + \left[\hat{P} - \frac{EA}{2L} \int_0^L \left(\frac{\partial \hat{w}_s}{\partial \hat{x}} \right)^2 d\hat{x} \right] \frac{\partial^2 \hat{w}_s}{\partial \hat{x}^2} = 0 \quad (3.29)$$

and solving for d_0 yields, for post-buckling ($\hat{P} > \hat{P}_{cr}$ and $d_0 \neq 0$), the relationship between the dimensional axial load \hat{P} and the resulting dimensional initial deflection d_0 :

$$d_0^2 = \frac{4}{\pi^2} \frac{(\hat{P} - \hat{P}_{cr})L^2}{EA} \quad (3.30)$$

According to the multi-mode Galerkin discretization, $\hat{v}(\hat{x}, \hat{t})$ can be expanded into a superposition of N orthonormal base functions $\phi_n(\hat{x})$, as $\hat{v}(\hat{x}, \hat{t}) = \sum_{n=1}^N \eta_n(\hat{t}) \phi_n(\hat{x})$ where $\eta_n(\hat{t})$ are the generalized coordinates. Retaining only the first mode and approximating the mode shape with the first buckling mode shape function ($\hat{v}(\hat{x}, \hat{t}) \approx \eta(\hat{t}) \psi(\hat{x})$), the expression for the total deflection becomes:

$$\hat{w}(\hat{x}, \hat{t}) = d_0 \psi(\hat{x}) + \eta(\hat{t}) \psi(\hat{x}) = q(\hat{t}) \psi(\hat{x}) \quad (3.31)$$

where $q(\hat{t}) = d_0 + \eta(\hat{t})$ represents the time-dependent displacement of the middle point of the clamped-clamped beam relative to the axis passing through the supports. Substituting the expression for $\hat{w}(\hat{x}, \hat{t})$ (3.31) into (3.1) and applying the expansion theorem (by multiplying for ψ and integrating over the length) yields to

the equation:

$$m\ddot{q} + c\dot{q} + k_3q + k_2q^3 = f \quad (3.32)$$

where $(\dot{\cdot}) = d(\cdot)/d\hat{t}$, m , c and f are the generalized mass, damping and load, respectively, and k_3 and k_2 are the linear and (cubic) nonlinear stiffness, respectively.

They are expressed as:

$$\begin{aligned} m &= \rho A \int_0^L \psi^2 d\hat{x}, \quad c = \gamma \int_0^L \psi^2 d\hat{x}, \quad k_2 = \frac{EA}{2L} \left(\int_0^L \psi'^2 d\hat{x} \right)^2 \\ k_3 &= EJ \int_0^L \psi''^2 d\hat{x} - \hat{P} \int_0^L \psi'^2 d\hat{x}, \quad f = \int_0^L \hat{F} \psi d\hat{x} \end{aligned} \quad (3.33)$$

Equation (3.32) is the equation of a Duffing-type nonlinear oscillator, describing the single-degree-of-freedom motion of the transverse vibration of the beam midpoint.

The restoring force potential of the Duffing oscillator, written in the form:

$$V(q) = +\frac{1}{2}k_3q^2 + \frac{1}{4}k_2q^4 \quad (3.34)$$

suggests that the sign of k_3 determines the number and type of the equilibrium positions. In fact, as the linear stiffness term becomes negative (i.e. $k_3 < 0$), the center equilibrium $q = 0$ becomes unstable and the potential becomes of the standard double-well type, resulting in the bistable harvesting system of interest. The potential barrier height is given by $\Delta V = k_3^2/(4k_2)$ and the two minima of the potential energy function, corresponding to the stable equilibrium positions, are located at $q_e = \pm\sqrt{-k_3/k_2}$. The bistable system can exhibit three different dynamic operating regimes depending on the depth of the potential barrier and the level of the input energy: in-well oscillations (oscillations in the neighborhood of one of the two stable equilibrium positions) if the input energy is lower than ΔV , chaotic alternating cross- and in-well oscillations for excitation energy sufficiently high to overcome the potential barrier, or large-amplitude cross-well response with further increase of the energy level.

3.3 Electromechanical coupling modeling

The electromechanical coupling is intended to be achieved via a permanent magnet and a cylindrical inductance coil. The electromechanical elements harvest the energy, which is dissipated across a resistive element in the electrical circuit; the transduction mechanism generates electricity by exploiting the relative displacement occurring within the system. The relative motion between the magnet and the coil of conducting wire generates an induced voltage (or induced emf) \mathcal{E} in the coil, which is proportional to the rate of change in time of the magnetic flux passing through the coil, according to Faraday's law. For an N turn coil, it is:

$$\mathcal{E} = -\frac{d\Phi}{dt} = -N\frac{d\phi}{dt} \quad (3.35)$$

where ϕ is the average flux linkage per turn and $\Phi = N\phi$ is the total flux linkage of the N turn coil. The flux linkage depends on the magnet and coil parameters and the air gap flux density between the magnet and coil. The total flux linkage for a N turn coil positioned in a magnetic field is evaluated as the combination of flux linkages through single turns, which encircle a surface area A_i , i.e.:

$$\Phi = \sum_{i=1}^N \int_{\vec{A}_i} \vec{B}(\vec{x}_i) d\vec{A} \quad (3.36)$$

where B denotes the magnetic field flux density for a given i^{th} turn area A_i , x_i the position of the coil. The area of the effective magnetic field depends on the magnet's relative position with respect to the coil (axial dependence) and the size of the coil in terms of its outer radius and inner radius (radial dependence). In the case where the flux density can be considered uniform over the area of the coil, the integral in (3.36) can be reduced to the product of the coil area, number of turns and the component of flux density normal to the coil area, $\Phi = NBA \sin \alpha$, where α is the angle between the coil area and the flux density direction. In most linear vibration generators, the motion between the coil and the magnet is in a

single direction, e.g., let us say the w -direction, and the voltage induced in the coil can then be expressed as the product of a flux linkage gradient and the velocity:

$$\Phi = -\frac{d\Phi}{dw} \frac{dw}{dt} = -N \frac{d\phi}{dw} \frac{dw}{dt} \quad (3.37)$$

A load resistance R_L connected to the coil terminals allows the power to be extracted from the harvesting device and the induced current to circulate into the coil. The induced current is able to flow through the coil and load resistance, creating its own magnetic field that opposes the field created by the permanent magnet. The interaction between the two magnetic fields results in an electromagnetic force F_{em} which opposes the motion, allowing the conversion of the mechanical energy into electrical energy.

According to Lorentz's law, the electromagnetic force F_{em} induced by the interaction of the magnet and the coil is proportional to the coil current \dot{Q} , i.e.:

$$F_{em} = k_e \dot{Q} \quad (3.38)$$

being $(\dot{\cdot}) = d(\cdot)/dt$. The proportionality constant k_e is the transduction factor, which physically describes the strength of the electromechanical coupling. The transduction factor can be defined as:

$$k_e = d\Phi/dw \quad (3.39)$$

It depends on the magnetic field flux density and coil geometry [67] and, for a uniform flux density over the area of the coil, substituting (3.36) into (3.39) it can be reduced to the following expression:

$$k_e = \frac{l_w h_c (r_o - r_i)}{A_c} B \quad (3.40)$$

with l_w length of the wire, r_o and r_i outer and inner radius of the coil, respectively, h_c and A_c thickness and cross-sectional area of the coil ($A_c = \pi((r_o + r_i)/2)^2$), B

the magnetic induction. Substituting the expression (3.39) into (3.35), the induced electromotive force is written as:

$$\mathcal{E} = k_e \dot{w} \quad (3.41)$$

On the other hand, the output voltage can be defined by applying Kirchhoff's law to the system, i.e.:

$$\mathcal{E} = (R_c + R_L)\dot{Q} + L_c\ddot{Q} \quad (3.42)$$

where R_c and L_c are the resistance and inductance of the coil respectively. The former is simply:

$$R_c = \rho \frac{l_w}{A_c} = \rho \frac{N^2 \pi (r_o + r_i)}{f h_c (r_o - r_i)} \quad (3.43)$$

with f the fill factor and ρ the resistivity of the coil material. By substituting (3.41) into (3.42), the current in the circuit can be written as:

$$\dot{Q} = \frac{k_e}{R_c + R_L} \dot{w} - \frac{L_c}{R_c + R_L} \ddot{Q} \quad (3.44)$$

An estimate for the coil inductance is provided by Wheeler in [90] as:

$$L_c = \frac{7.875 \cdot 10^{-06} (r_o + r_i)^2 N}{13r_o - 7r_i + 9h_c} \quad (3.45)$$

and the maximum coil impedance Z_L can be estimated as:

$$Z_L = 2\pi f_{max} L_c \quad (3.46)$$

where f_{max} is the maximum driving frequency, in Hz, imposed by the mechanical system.

Depending on the geometric properties of the coil, the inductance can be assumed to be negligible relative to the load resistance used, by an appropriate choice of the

coil dimensions). With this assumption the equation (3.44) can be simplified as:

$$\dot{Q} = \frac{k_e}{R_c + R_L} \dot{w} \quad (3.47)$$

Finally, the electromagnetic force is proportional to the current and hence the velocity, and thus it can be described as a linear, electromagnetic damping [81]:

$$F_{em} = b_e \dot{w} \quad (3.48)$$

where b_e is the electromechanically induced damping coefficient. Here, w denotes the relative displacement, defined as $y_2 - y_1$ (y_1 and y_2 being the absolute displacements of the primary system and the harvester, respectively) and \dot{w} its time derivative. By expressing the electromechanical damping coefficient as:

$$b_e = \frac{k_e^2}{R_c + R_L} \quad (3.49)$$

the linear differential equation that governs the electromagnetic interaction can be written as:

$$\dot{Q} = \frac{b_e}{k_e} \dot{w} \quad (3.50)$$

3.4 Governing equations and harvesting measures

Recalling Equation (3.32), which models the mechanical coupling between the primary mass m_1 and the secondary mass m_2 of the system of Figure 3.1, the nonlinear equations of motion of the complete system can be written using (3.32), provided that the Lagrangian coordinate q is substituted with the relative displacement $w = y_2 - y_1$ of the mass m_2 , placed at the midpoint of the beam (note that in Equation (3.31) $\psi(L/2) = 1$) and the damping coefficient accounts for both the inherent (mechanical) damping and the electromechanically induced damping b_e (see Equation (3.48)). The current \dot{Q} flowing in the circuit is related to the relative velocity \dot{w} by Equation (3.50). Finally, the coupled second-order

differential equations governing the dynamics of the electromechanical system of Figure 3.1, excited by a force $F(t)$ directly applied to the primary mass with zero initial conditions, can be written as follows:

$$\begin{aligned} m_1 \ddot{y}_1 + b_1 \dot{y}_1 + k_1 y_1 - (b_e + b_2) \dot{w} - k_3 w - k_2 w^3 &= F(t) \\ m_2 (\ddot{w} + \ddot{y}_1) + (b_e + b_2) \dot{w} + k_3 w + k_2 w^3 &= 0 \\ \dot{Q} - \frac{b_e}{k_e} \dot{w} &= 0 \end{aligned} \quad (3.51)$$

where k_1 and b_1 represent respectively the linear stiffness coefficient and the linear viscous damping coefficient of the LO, b_2 the linear viscous damping coefficient of the BNEH, and k_2 the cubic stiffness coefficient, and k_3 denotes the linear stiffness coefficient. The sign of k_3 determines the number and type of the equilibrium positions of the system. In fact, as seen in Section 3.2, from the definition of the restoring force potential governing the system dynamics, written for the complete system as:

$$V(y_1, w) = \frac{1}{2} k_1 y_1^2 + \frac{1}{2} k_3 w^2 + \frac{1}{4} k_2 w^4$$

it becomes apparent that for $k_3 \geq 0$ the harvester is monostable whereas in the presence of a negative linear stiffness term (i.e. $k_3 < 0$) the center equilibrium $y_1 = w = 0$ becomes unstable bifurcating into the two specular stable states $y_1 = 0, w = \pm \sqrt{-k_3/k_2}$ (Figure 3.5). The potential barrier height is given by $\Delta V = k_3^2/(4k_2)$ and the bistable system can exhibit different dynamic operating regimes, for a given potential barrier height, depending on the level of the input energy: if the input energy is lower than ΔV , it performs oscillations in the neighborhood of one of the two stable equilibrium positions (in-well oscillations); increasing the excitation energy yields chaotic alternating cross- and in-well oscillations; with further increase of the energy, large-amplitude periodic cross-well responses occur. Each of them represents a different targeted energy transfer mechanism from the directly forced LO to the BNEH [14]. Hence, the dynamics of the bistable system is driven by the depth of the potential wells and the magnitude of input energy.

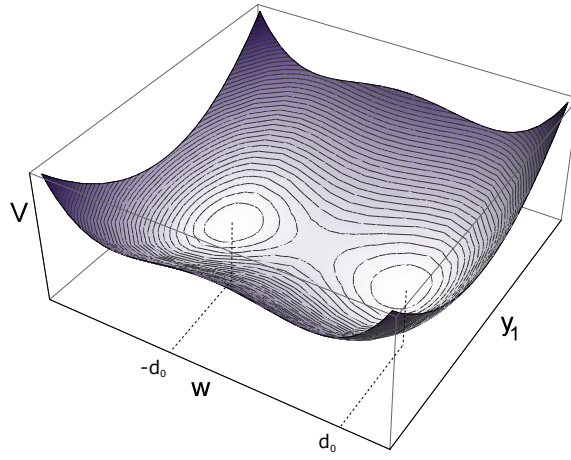


Figure 3.5: Potential energy surface of the coupled system.

The set of governing equations (3.51) can be conveniently written with reference to the initial equilibrium position of the BNEH mass, corresponding to one of the potential wells. In order to do so, the change of variables $w = z + d_0$ is introduced, where $d_0 = \sqrt{-k_3/k_2}$ is the position of each of the two equilibrium points, so that the nonlinear elastic force:

$$F_s(w) = k_3w + k_2w^3$$

assumes the expression:

$$F_s(z) = -2k_3z + 3d_0k_2z^2 + k_2z^3$$

Ergo, the set of equations (3.51) become:

$$\begin{aligned} m_1\ddot{y}_1 + b_1\dot{y}_1 + k_1y_1 - (b_e + b_2)\dot{z} + 2k_3z - 3d_0k_2z^2 - k_2z^3 &= F(t) \\ m_2(\ddot{z} + \ddot{y}_1) + (b_e + b_2)\dot{z} - 2k_3z + 3d_0k_2z^2 + k_2z^3 &= 0 \\ \dot{Q} - \frac{b_e}{k_e}\dot{z} &= 0 \end{aligned} \tag{3.52}$$

By scaling the time such that $t = c_t\tau$ and introducing the variables $y_1 = c_x x, z =$

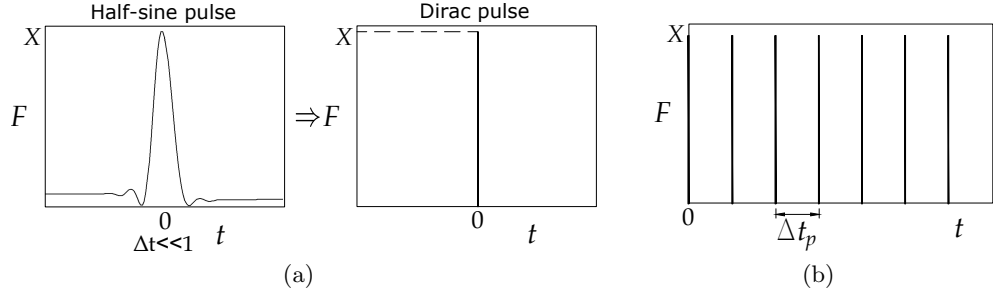


Figure 3.6: Single impulse (a) and train of impulses of inter-arrival times Δt_p (b).

$c_x v, Q = c_q q$, equations (3.52) can be rewritten in normalized form as:

$$x'' + \lambda x' + x - \mu[(\beta + \zeta)v' - 2\xi v + 3\alpha v^2 + v^3] = \gamma f(\tau) \quad (3.53a)$$

$$v'' + x'' + (\beta + \zeta)v' - 2\xi v + 3\alpha v^2 + v^3 = 0 \quad (3.53b)$$

$$q' - \beta v' = 0 \quad (3.53c)$$

where the following non-dimensional parameters have been defined:

$$\mu = \frac{m_2}{m_1}, \quad \lambda = \frac{b_1}{\sqrt{m_1 k_1}}, \quad \zeta = \frac{b_2}{m_2} \sqrt{\frac{m_1}{k_1}}, \quad \beta = \frac{b_e}{m_2} \sqrt{\frac{m_1}{k_1}}, \quad \xi = \frac{k_3}{k_1} \frac{m_1}{m_2} \quad (3.54)$$

with $\gamma = \frac{1}{k_1} \sqrt{\frac{k_2 m_1}{k_1 m_2}}$ and $(\cdot)' = d(\cdot)/d\tau$. The normalization coefficients are given by

$$c_t = \sqrt{\frac{m_1}{k_1}}, \quad c_x = \sqrt{\frac{k_1 m_2}{k_2 m_1}}, \quad c_q = \frac{k_1 m_2}{k_e m_1} \sqrt{\frac{m_2}{k_2}} \quad (3.55)$$

For the normalized system the two stable equilibrium positions are $x = 0, v = 0$ and $x = 0, v = 2\alpha$, with $\alpha = \sqrt{-\xi}$. In order to study the effects of system damping, electromechanical coupling and mass ratio on the performance of the harvester, the coupled system (3.51) is first explored in the normalized form (3.53).

Two different excitation scenarios are considered. In the first case, a single impulsive forcing excitation is applied to the linear subsystem. As is well known,

an instantaneously applied force $F(t) = X\delta(t)$ at $t = 0$, obeying

$$\int_{-\infty}^{+\infty} F(t) dt = \int_{-\infty}^{+\infty} X\delta(t) dt = X$$

with $\delta(t)$ the Dirac delta function and X the magnitude of the impulse, applied to the system at rest at $t = 0^-$, is equivalent to imposing an initial velocity of X/m_1 and no external forcing. Denoting by $I_0 = X/m_1$ the dimensional initial velocity of the primary system directly following the applied impulse, the non-dimensional equations (3.53) are complemented by the following initial conditions:

$$x(0^+) = 0, \quad x'(0^+) = \tilde{I}_0, \quad v(0^+) = 0, \quad v'(0^+) = -\tilde{I}_0, \quad q(0^+) = 0 \quad (3.56)$$

where $\tilde{I}_0 = c_t/c_x I_0$, solved with $\gamma f(\tau) = 0$.

As a second forcing scenario, a series of pulses, defined as:

$$F(t) = \sum_{p=0}^N X_p \delta(t - t_p), \quad t_p = \sum_{r=1}^p \Delta t_r \quad (3.57)$$

is input into system (3.52), where N is the total number of impulses applied after the initial excitation, corresponding to $p = 0$, t_p the time of application of the p^{th} impulse, Δt_p the interval of time between the two consecutive pulses $(p - 1)$ and p .

For the first impulse, at $t_0 = 0$, assuming that the system is at rest at $t = 0^-$, the initial conditions are still expressed by (3.56) or, referring to the dimensional system (3.52):

$$y_1(0^+) = 0, \quad \dot{y}_1(0^+) = I_0, \quad z(0^+) = 0, \quad \dot{z}(0^+) = -I_0, \quad Q(0^+) = 0 \quad (3.58)$$

whereas the p^{th} impulse, applied to the LO at time t_p^+ , is assigned by imposing the

following initial conditions:

$$\begin{aligned} y_1(t_p^+) &= y_1(t_p^-), \quad \dot{y}_1(t_p^+) = \dot{y}_1(t_p^-) + I_{0,p} \\ z(t_p^+) &= z(t_p^-), \quad \dot{z}(t_p^+) = \dot{z}(t_p^-) - I_{0,p} \\ Q(t_p^+) &= Q(t_p^-), \quad r = 1, \dots, N \end{aligned} \quad (3.59)$$

As becomes clear from (3.59), the initial state of the system at the time of the application of the p^{th} impulse depends upon the mechanical energy remaining in the system at that time.

The instantaneous power extracted by the transduction mechanism, i.e. dissipated across the resistive element in the coupled circuit, is given by

$$P(t) = R_L \dot{Q}^2 = \left(\frac{k_e^2 - R_c b_e}{k_e^2} \frac{k_1^2 m_2}{k_2 m_1} \sqrt{\frac{k_1}{m_1}} \right) \frac{\mu}{\beta} q'^2 \quad (3.60)$$

where the term in brackets has units of Watts, whereas the term $\mu/\beta q'^2$ is the non-dimensional power. It follows that the total energy harvested following the p^{th} impulse is obtained by integrating the power (3.60) over the time interval between the application of the p^{th} impulse and the succeeding one; that is,

$$E_h(t_{p+1}^-) = \int_{t_p}^{t_{p+1}} P(t) dt = \frac{k_e^2 - R_c b_e}{k_e^2} \frac{k_1^2 m_2}{k_2 m_1} \int_{\tau_p}^{\tau_{p+1}} \frac{\mu}{\beta} q'(\tau)^2 d\tau \quad (3.61)$$

If only one impulse is applied to the primary system, the energy harvested by the BNEH up to time t , $E_h(t)$, can be obtained from Equation (3.61) by replacing the lower limit of the integral by zero and the upper limit of the integral by t ; the total energy harvested up to the end of the damped motion, at $t = t_f$, is given by the asymptotic limit reached by $E_h(t)$.

The energy harvesting performance is also defined in terms of energy harvesting efficiency, which is expressed as the total energy harvested after the p^{th} impulse, normalized by the total energy in the system at the time t_p^+ of application of that

impulse:

$$\eta_{\%} = \frac{E_h(t_{p+1}^-)}{E_{tot}(t_p^+)} 100 \quad (3.62)$$

where

$$\begin{aligned} E_{tot}(t_p^+) = & \frac{1}{2}m_1[y_1(t_p^+)]^2 + \frac{1}{2}m_2[\dot{z}(t_p^+) + y_1(t_p^+)]^2 + \frac{1}{2}k_1[y_1(t_p^+)]^2 - k_3[z(t_p^+)]^2 \\ & + ak_2[z(t_p^+)]^3 + \frac{1}{4}k_2[z(t_p^+)]^4 \end{aligned} \quad (3.63)$$

The expression (3.63) for the total energy in the system immediately after the application of an impulse suggests that, if a single impulse is considered, it coincides with the kinetic energy input into the primary system, holding the initial conditions (3.58); otherwise it takes into account the amount of energy still possessed by the system at the time of application of the p^{th} impulse.

Chapter 4

Numerical investigation

This chapter deals with the numerical study of the integrated harvesting system. Discussed here is the dynamics of the electromechanical system and resulting phenomena upon which a novel vibration energy harvesting apparatus is designed and validated. Due to the double-well potential of the bistable system, several distinct dynamic regimes arise and provide for efficient transfer and harvesting of energy.

4.1 Parametric analysis and optimization

In order to study the effect of the bistability on the damped dynamics and to evaluate the effect of sensitive parameters on the performance of the bistable harvesting system, a computational study for the first excitation scenario of single impulse is carried out, using the non-dimensional nonlinear equations of motion (3.53) and the initial conditions (3.56). The sensitivity analysis conducted on this system reveals the strong dependence of the efficiency of the BNEH on the mass ratio parameter. The efficiency measure is here computed from (3.62) with

$$E_{tot}(0^+) = \frac{1}{2}m_1\dot{I}_0^2 = k_1^2 \frac{m_2}{2k_2m_1} \tilde{I}_0^2$$

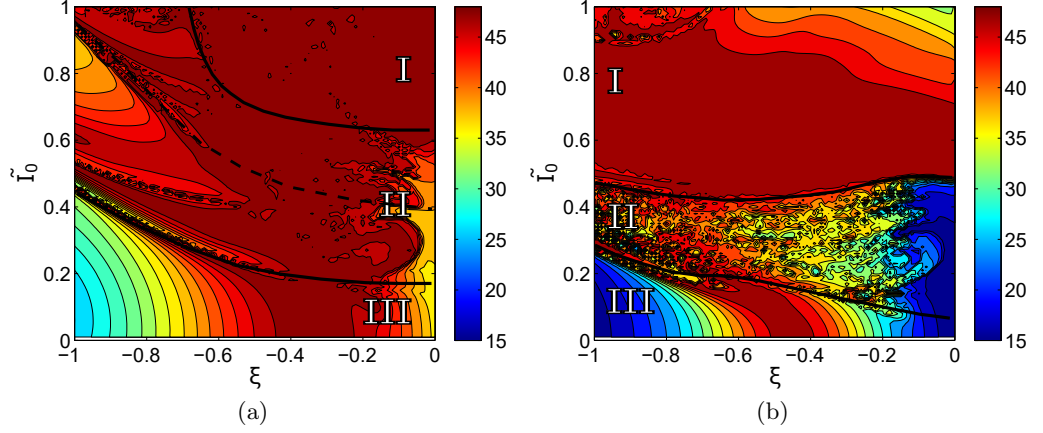


Figure 4.1: Contour plots for efficiency measure $\eta\%$ resulting from the application of a single impulse to the primary linear system, evaluated at $\tau = 60$ as a function of ξ and \tilde{I}_0 . Parameters are $\beta = 0.1$, $\lambda = 0.001$, $\zeta = 0.02$: (a) $\mu = 0.2$; (b) $\mu = 0.05$; regions I, II and III refer to different dynamic behaviours as discussed in the text.

so that

$$\eta\% = \frac{(k_e^2 - R_c b_e)/k_e^2 \int_0^\tau \mu/\beta q'(\tau)^2 d\tau}{1/2\tilde{I}_0^2} \times 100 \quad (4.1)$$

with the coil resistance, transduction factor and electromagnetic damping coefficients given in Table 4.2. Figure 4.1 shows the percentage of impulsive energy $\eta\%$ which is harvested during the damped motion by the BNEH up to a time $\tau = 60$ (which corresponds physically to approximately $t = 1$ s for the physical system presented in Section 4.2), as a function of the negative stiffness parameter ξ in the range $[-1.0, 0.0]$ and the magnitude of the initial velocity \tilde{I}_0 in the range $(0.0, 1.0]$. The comparison of the two contour plots reveals that, in the domain of low impulse magnitudes, i.e. $\tilde{I}_0 \in (0.0, \sim 0.5)$, as the mass ratio decreases, the presence of the negative stiffness allows a greater enhancement of the harvester efficiency with respect to the monostable configuration (approximately three times). Conversely, high values of the mass ratio increase the monostable efficiency, whereas they slightly reduce the bistable harvesting capability, with the result that the bistable structure loses its advantage.

In Figure 4.1(b) three different regions of the contour plot can be detected, each of which corresponds to one of the three different mechanisms of energy transfer

from the linear oscillator to the bistable attachment discussed in [72]. Region I is associated with high input energy which enables cross-well oscillations to occur. The snap through between the two stable equilibrium positions leads to an intense energy exchange between the two subsystems, and hence to intense energy harvesting. As the input energy level further increases, 1:1 transient resonance capture dominates the initial dynamics, whereas cross-well oscillations take place only in a second stage during a few cycles before the BNEH falls into one of the potential wells. However, the cross-well phase is characterized by the best performance of the harvester. The intermediate regime of region II is dominated by alternating in-well and cross-well oscillations. This chaotic motion is still beneficial for energy harvesting mainly due to the jumps from one stable equilibrium position to the other. As expected, this intermediate dynamical regime tends to disappear as the negative stiffness parameter ξ tends to zero (i.e., in the monostable configuration); this is evidenced by the blue region on the right of Figure 4.1(b). Region III refers to the lowest-energy regime, in which the motion of the BNEH is confined in one of the two wells, depending on the initial conditions; here, the negative stiffness promotes nonlinear beats which are the main mechanisms for energy absorption. Strongly modulated oscillations can be observed as the negative stiffness parameter approaches its optimal range. In general, both periodic and chaotic cross-well dynamics are observed in the first cycles of the motion (see Figures 4.5 et seq. in Section 4.2). Even in the presence of very weak inherent damping of the BNEH, the overall damping, including the contribution by the electromechanical elements and any losses associated with the linear stiffness, leads to fast decay of oscillations. As the energy decreases, the motion of the bistable attachment is trapped in one of the wells, where the third mechanism still allows some energy harvesting until the system goes to rest. The three energy transfer mechanisms can be only partly traced on the plot for the case of high mass ratio (Figure 4.1(a)). In the intermediate region, chaotic cross-well motions can take place depending on the magnitude of the impulse and the height of the potential barrier (upper portion of

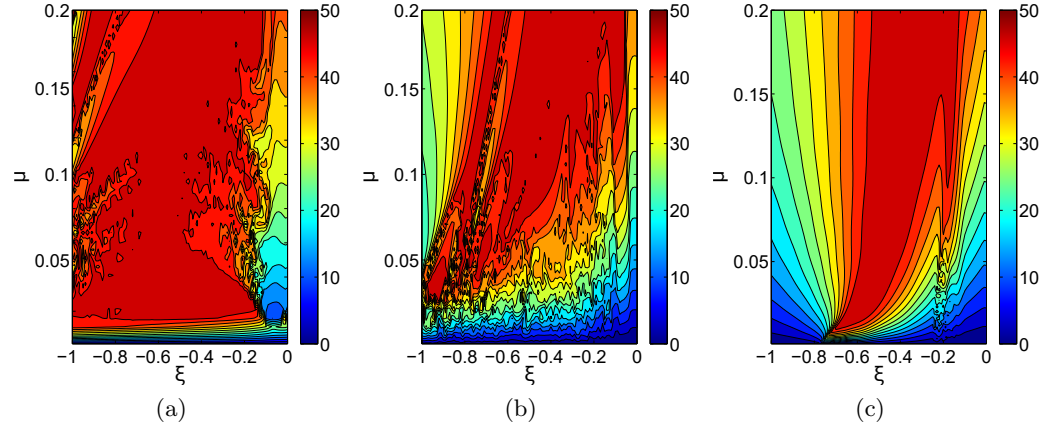


Figure 4.2: Contour plots for the efficiency measure $\eta\%$ resulting from the application of a single impulse to the primary linear system, evaluated at $\tau = 60$ as a function of the negative stiffness parameter ξ and the mass ratio μ . Parameters are $\beta = 0.1$, $\lambda = 0.001$, $\zeta = 0.02$: (a) $\tilde{I}_0 = 0.45$; (b) $\tilde{I}_0 = 0.25$; (c) $\tilde{I}_0 = 0.09$.

region II, delimited by the dashed line); alternatively, the harvester can perform high-amplitude in-well oscillations after a single initial jump into the opposite well (lower portion of region II). In Figure 4.2, the energy measure $\eta\%$ for three different energy levels within the range of the low impulses, namely $\tilde{I}_0 = 0.45$, $\tilde{I}_0 = 0.25$ and $\tilde{I}_0 = 0.09$, is presented as a function of the mass ratio and negative stiffness parameters. The plots confirm, in particular for very low impulses, the greater gain in energy harvesting of the bistable configuration for a lower mass ratio. A small mass of the harvester is desirable, and often required, in real applications.

In the low-initial-energy portion of Figure 4.1, depending on the impulse magnitude and the mass ratio, a range of optimal negative stiffness is clearly detected. This well-defined range for optimal ξ disappears in the high-energy region (\tilde{I}_0 greater than approximately 0.5), revealing the loss of effectiveness of the bistability in the harvester performance. It should be noted that the value of $\xi \simeq 0.5$, corresponding to the maximum efficiency of the harvesting device in the low-energy regime, implies that the harvester's frequency of oscillation in its motion around a stable equilibrium state (i.e., in one of the potential wells) is tuned to the natural frequency of linear oscillator. It is also noteworthy that these findings depend on the time interval of computation for the harvesting measure (4.1). Naturally, energy can be

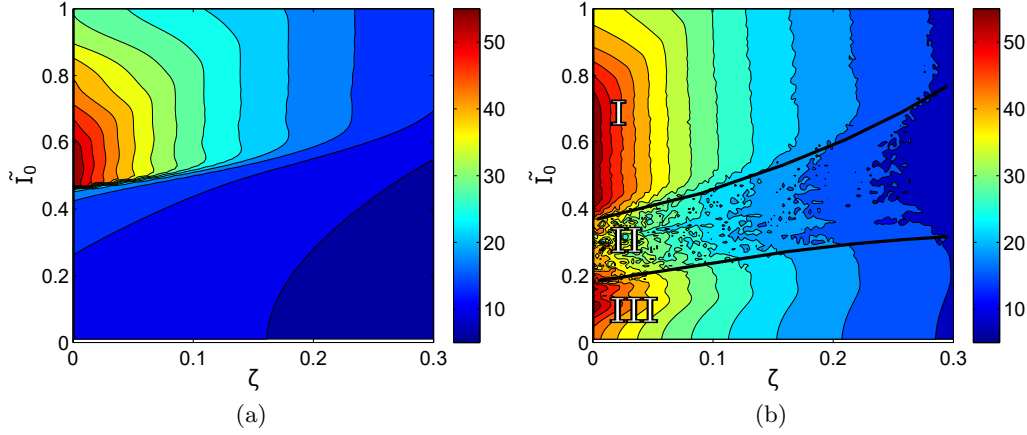


Figure 4.3: Contour plots of the efficiency measure $\eta\%$ resulting from the application of a single impulse to the primary linear system, harvested up to time $\tau = 60$, as a function of the inherent viscous damping of the coupling ζ and the amplitude of the initial velocity \tilde{I}_0 . Parameters are $\beta = 0.1$, $\lambda = 0.001$, $\mu = 0.04$: (a) monostable configuration ($\xi = 0.0$); (b) bistable configuration ($\xi = -0.6$); regions I, II and III refer to the same regions of Figure 4.1.

harvested until the system comes to rest, around $\tau = 140$; however, as will be shown in Section 4.2, the time $\tau = 60$ corresponds physically to approximately 1 second, which is convenient in view of subsequent investigation of repeated impulses.

The parametric analysis of energy harvesting performance conducted on the non-dimensional system highlights also the central role of damping. As shown in Figure 4.3, an increase of the inherent (purely mechanical) linear viscous damping in the coupling, ζ , causes a deterioration of the energy harvesting efficiency, regardless of the presence of the negative stiffness term in the coupling. As expected, contrary to what would be needed in a passive nonlinear vibration control system, very weak damping in the coupling is desirable in order to optimize the performance of the harvester. The contour plots of Figure 4.3(a) also confirm the existence of a critical threshold for the initial energy imparted to the system, below which the performance of the system in its monostable configuration drastically decreases. The contours in the plot of Figure 4.3(b) are in agreement with the boundaries of the three behavioral regions identified above.

Furthermore, as discussed in Section 3.3, the electromechanical coupling introduces an additional velocity-proportional damping term in the equations of motion,

besides determining the amount of the electric current circulating in the coil, according to Equation (3.53c). The electromechanical coupling coefficient β is dependent upon the transduction factor k_e (see Equation (3.49)), which is determined by the geometric features of the coil and by the permanent magnet selection (cfr. Equation (3.40)). Hence, the restriction to $(0.0, 1.0]$ of the electromechanical coupling to the range β , within which the variation of energy harvested is explored, corresponds to physical limitations of the experimental apparatus. Numerical simulations of a non-optimized system with high mass ratio and high BNEH damping reveal that the percentage of energy harvested by the BNEH is strongly affected by the value of β , namely following a monotonically increasing trend with positive but decreasing slope up to $\beta = 1.0$, independent of the NEH mono- or bistable configuration and of the impulse level. For an optimized system, the contour plot of the surface given by $\eta_{\%}$ as a function of β and \tilde{I}_0 is displayed in Figure 4.4. In the region of low input energy, where the monostable harvester performance is still strongly related to the value of β (Figure 4.4(a)), this dependence is progressively reduced by the addition of the negative stiffness, reaching the scenario shown in Figure 4.4(b) at the optimal value of the negative stiffness parameter ($\xi = 0.6$). A plateau of increasing efficiency is shown to exist for the entire range of impulse magnitudes studied, starting from $\beta \approx 0.1$ (Figure 4.4). Since the electromechanical coupling parameter β depends on the size of the coil, $\beta = 0.1$ is deemed acceptable to preserve different energy transfer mechanisms (addressed in [72]) while keeping the coil construction simple, in view of the planned experiments that will be built upon the available experimental apparatus developed by Remick et al. [68]. It becomes apparent upon comparing the contour plots of Figures 4.4(a) and 4.4(b) that a great enhancement in energy harvesting efficiency is allowed by the addition of the negative stiffness for the case of low impulses.

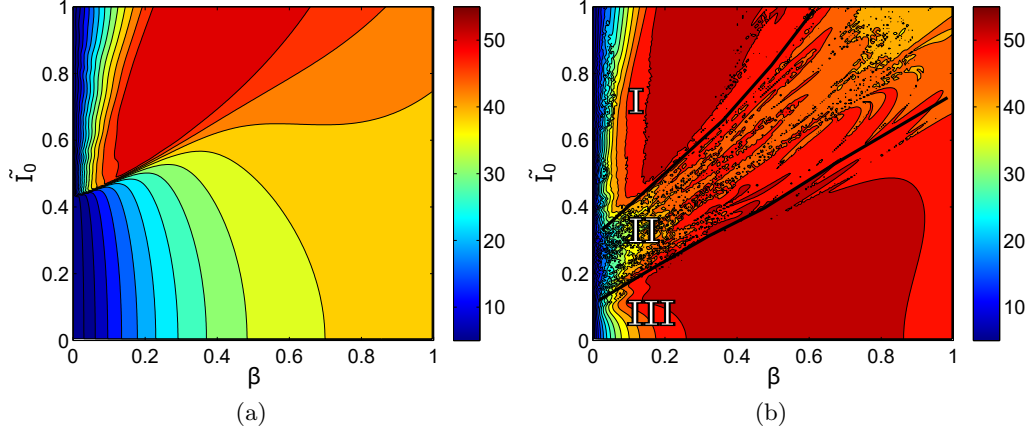


Figure 4.4: Contour plots of the efficiency measure $\eta\%$ resulting from the application of a single impulse to the primary linear system, evaluated at $\tau = 60$ as a function of the electromechanical coupling parameter ζ and the amplitude of the initial velocity I_0 . Parameters are $\lambda = 0.001$, $\zeta = 0.02$, $\mu = 0.04$: (a) monostable configuration ($\xi = 0.0$); (b) bistable configuration ($\xi = -0.6$); regions I, II and III refer to the same regions of Figure 4.1.

Description, symbol	Value
Mass ratio, μ	0.04
Negative linear stiffness in the coupling, ξ	-0.6
LO linear viscous damping, λ	0.001
Linear viscous damping in the coupling, ζ	0.02
Electromechanical coupling, β	0.1

Table 4.1: Non-dimensional parameters of the system (3.53).

4.2 Dynamic response of the optimal BNEH

In this section the dynamics of the system is investigated for varying energy levels input into the linear oscillator, within the domain of low impulses, where the capacity of an analogous monostable NEH for optimal energy harvesting deteriorates. For the system properly designed using the results from the parametric study, three different energy-transfer mechanisms are detected for different magnitudes of impulsive excitation, in agreement with the results discussed in [72]. The time-domain response of the system (3.52) and the associated temporal evolution of the energy measures described by (3.61) and (3.62) are explored by performing numerical simulations for the non-dimensional system (3.53) with the initial conditions (3.56), with parameters (3.54) chosen on the basis of the parametric study and listed in

Description, symbol	Value
LO mass, m_1	7.1 kg
LO linear viscous damping, b_1	0.38 Ns/m
LO linear stiffness, k_1	19 889.25 N/m
BNEH mass, m_2	0.284 kg
Linear viscous damping in the coupling, b_2	0.31 Ns/m
BNEH cubic stiffness, k_2	$1.824 \times 10^7 \text{ N/m}^3$
BNEH linear stiffness, k_3	-477.36 N/m
Load resistance, R_L	47 Ω
Coil resistance, R_c	32.1 Ω
Transduction factor, k_e	11 T m
Electromechanical damping coefficient, b_e	1.53 Ns/m

Table 4.2: Dimensional parameters for the system (3.51).

Table 4.1, and with physical variables scaled using the normalization constants (3.55).

The dimensional parameter values of system (3.52) are shown in Table 4.2. The system is integrated for a simulation duration of 140 time units, corresponding physically to 2.6 s, which is long enough to allow the system dynamics to damp out completely. The frequency content of the displacement time histories during the time interval analyzed is studied by applying the wavelet transform to the damped responses. Also, the instantaneous energy stored in the BNEH is computed, as the ratio between the total energy of the BNEH and the total energy in the two-DOF system at time t , in order to provide more insights into the energy transfer between the two subsystems, and thus the capability of the harvester to passively absorb impulsive energy from the LO.

Three different energy levels are reported: the highest energy level, close to the upper limit of the range of low impulses, corresponding to an initial velocity $I_0 = 0.16 \text{ m/s}$ ($\tilde{I}_0 = 0.45$); an intermediate energy level, with $I_0 = 0.09 \text{ m/s}$, corresponding to $\tilde{I}_0 = 0.25$; and finally, the lowest one, with initial velocity $I_0 = 0.03 \text{ m/s}$ and $\tilde{I}_0 = 0.09$.

In Figure 4.5 the response of the system when the primary oscillator is impulsively excited by the highest energy level is shown. Cross-well oscillations performed by

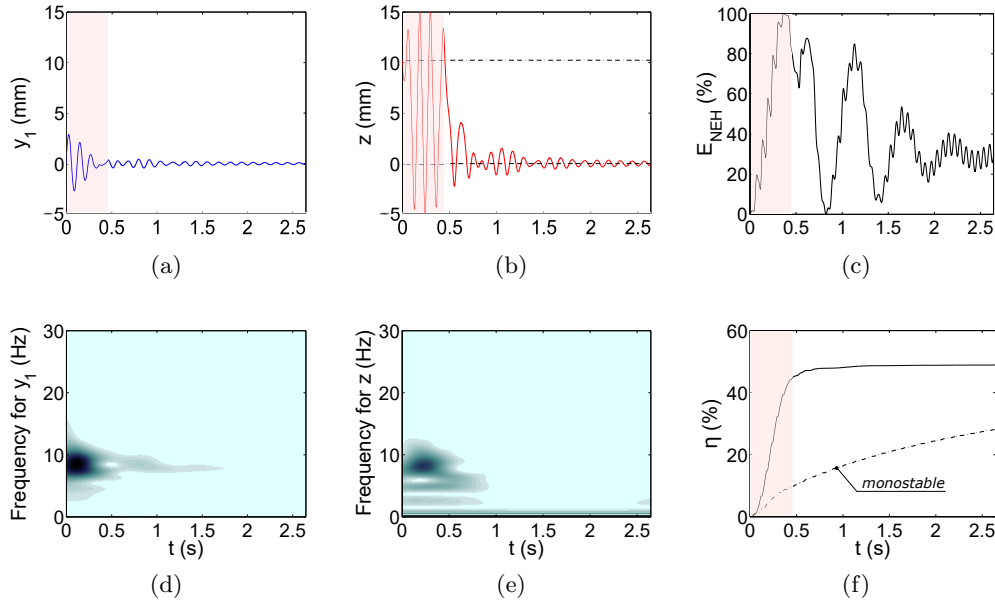


Figure 4.5: Transient dynamics of the two-DOF system for the high input energy level ($I_0 = 0.16$ m/s): time histories of the linear oscillator (a) and harvester (b) responses (dashed lines represent the two equilibrium positions); (d) and (e) corresponding wavelet transform spectra; (c) percentage of instantaneous total energy in the BNEH; (f) percentage of total energy harvested by the BNEH (the dotted-dashed line represents the same quantity for the analogous monostable NEH).

the BNEH in the first 0.4 s allow fast energy transfer from the linear oscillator to the nonlinear bistable energy harvesting device, resulting in energy harvesting efficiency of approximately 44% within this initial stage of the motion, which represents 90% of the overall harvesting. The corresponding amount of energy harvested up to the first 0.4 s is 38 mJ, reaching 43 mJ by the time the system comes to rest. The energy initially stored in the LO quickly flows to the BNEH, then is released back to the LO. The motion is strongly localized to the BNEH as evidenced by the fact that the amplitude of oscillation of the BNEH is more than three times as large as that of the LO. The time-frequency analysis (wavelet spectrum) of the relative response reveals that a 1:1 resonance capture between the LO and the BNEH takes place, but also subharmonic components over a broader frequency ranges, mainly 1:2 and 1:3, are present, which is what enhances TET. Figure 4.6 shows the dynamics of the system for the intermediate impulse level. The BNEH time series shows that the harvester is able to overcome the potential

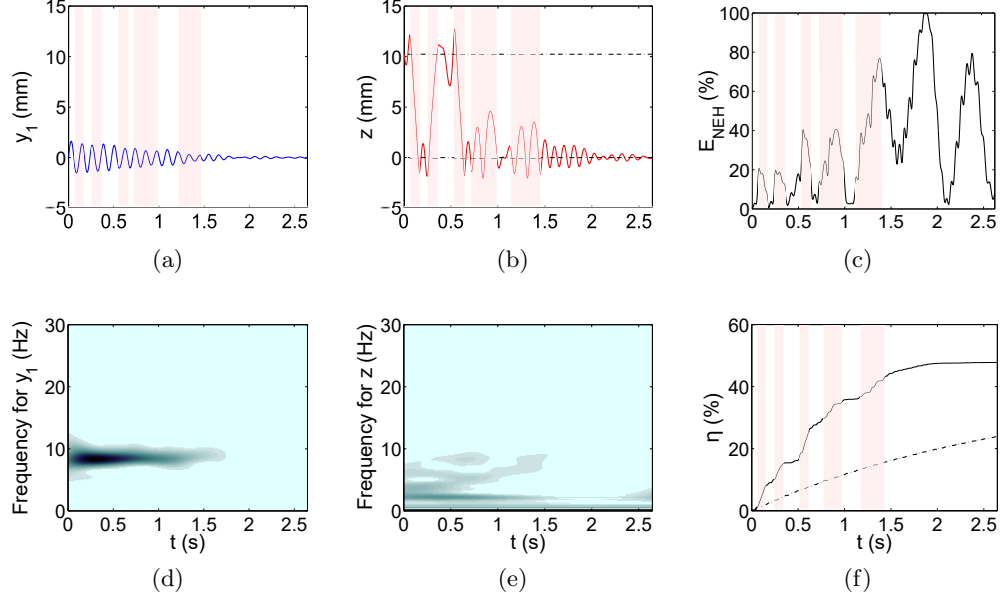


Figure 4.6: Transient dynamics of the two-DOF system for the intermediate input energy level ($I_0 = 0.09$ m/s): time histories of linear oscillator (a) and harvester (b) responses (dashed lines represent the two equilibrium positions); (d) and (e) corresponding wavelet transform spectra; (c) percentage of instantaneous total energy in the BNEH; (f) percentage of total energy harvested by the BNEH (the dotted-dashed line represents the same quantity for the analogous monostable NEH).

barrier and undergo chaotic cross- and in-well oscillations in the range 0–0.6 s. The three jumps between the two stationary positions correspond in the energy harvesting efficiency plot to an increase of the rate of harvesting. This first regime accounts for around 26% of the energy harvested. The following second regime, consisting in in-well oscillations, leads the system to achieve the final 48% efficiency. The amount of energy eventually harvested by the nonlinear bistable device is of 13 mJ. Part of the energy initially stored in the LO flows back and forth between the two oscillators for the first second in a reversible energy transfer. Hence the system is still able to capture energy, but more slowly.

For the lowest excitation magnitude the dynamics evolves around one of the two stationary positions, depending on the initial conditions (Figure 4.7(b)). In-well oscillations again allow good energy harvesting performance; the energy exchange is due in this case to a 1 : 1 resonance capture. Nonlinear beats occur and, as a result, energy is continuously exchanged between the LO and the nonlinear attachment.

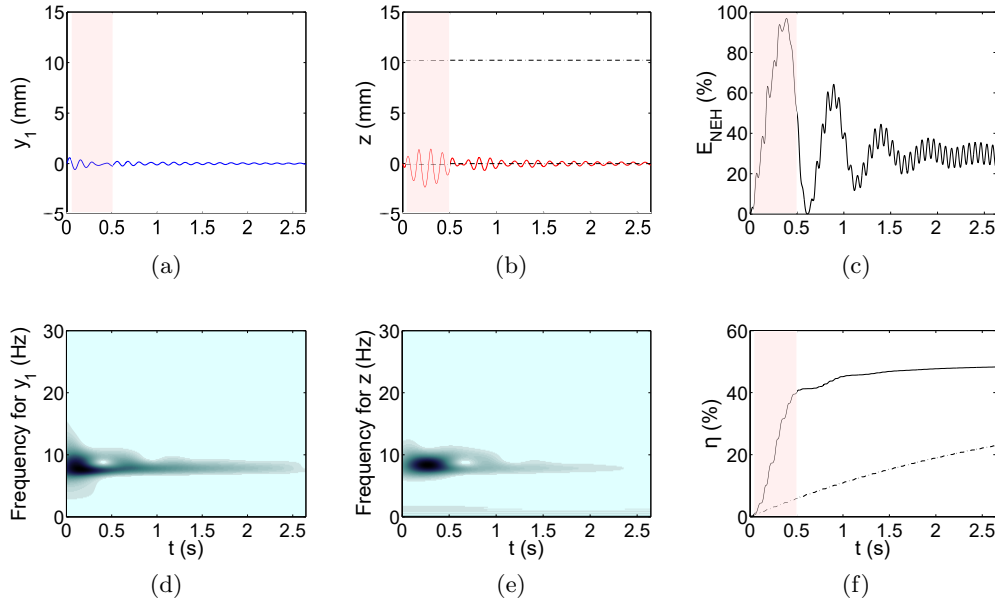


Figure 4.7: Transient dynamics of the two-DOF system for the low input energy level ($I_0 = 0.03 \text{ m/s}$): time histories of linear oscillator (a) and harvester (b) responses (dashed lines represent the two equilibrium positions); (d) and (e) corresponding wavelet transform spectra; (c) percentage of instantaneous total energy in the BNEH; (f) percentage of total energy harvested by the BNEH (the dotted-dashed line represents the same quantity for the analogous monostable NEH).

A fast energy transfer from the LO to the BNEH, with 40% of the total 48% of energy harvested, occurs in the first 0.5s, due to larger oscillation amplitudes of the nonlinear attachment. 2 mJ of energy is harvested by the nonlinear device when this low-magnitude impulse is input to the LO.

The monostable counterpart of the system under investigation presents a common behavior in the entire range of excitation magnitudes studied. The case for $I_0 = 0.09 \text{ m/s}$ is reported as an example in Figure 4.8. The NEH undergoes small oscillations and most of the impulsive energy remains localized to the directly excited primary system, as becomes apparent from Figure 4.8(c), where the instantaneous energy possessed by the NEH during the motion is approximately zero (the scale has been changed for the sake of readability). The amount of total energy eventually harvested by the monostable nonlinear device is three times smaller for the high and intermediate energy levels and four times smaller for the lowest one.

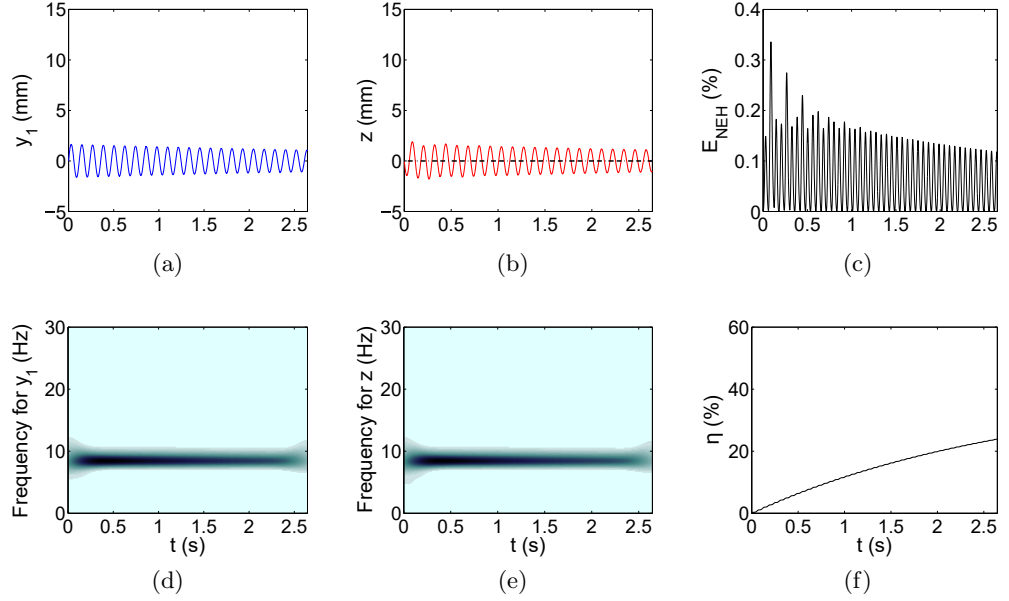


Figure 4.8: Transient dynamics of the two-DOF system in its monostable configuration, for the intermediate input energy level ($I_0 = 0.09m/s$): time-histories of linear oscillator (a) and harvester (b) responses; (d) and (e) corresponding wavelet transform spectra; (c) percentage of instantaneous total energy in the NEH; (f) percentage of total energy harvested by the NEH

4.3 Energy harvesting efficiency under repeated impulses

4.3.1 Periodic impulses scenario

The response of the system (3.51) when the primary structure is excited by a train of pulses characterized by the same magnitude ($X_p = X$, $p = 1, \dots, N$, hence $I_{0,p} = I_0$, $p = 1, \dots, N$) and same inter-arrival time ($\Delta t_p = \Delta t_r$, $p, r = 1, \dots, N$) is investigated in this section. Numerical simulations are carried out for the dimensional system (3.52) complemented by the initial conditions (3.58) and (3.59), for various forcing amplitudes, expressed in terms of initial velocity I_0 , and for various inter-arrival times Δt_p . A normalized impulsive period μ_T is defined, as the duration of time Δt_p between the application of two consecutive pulses, normalized by the fundamental period of the primary system $T_1 = 2\pi\sqrt{k_1/m_1}$, such that the impulse period is defined as $\mu_T = \Delta t_p/T_1$ ($T_1 = 0.1187s$ for the

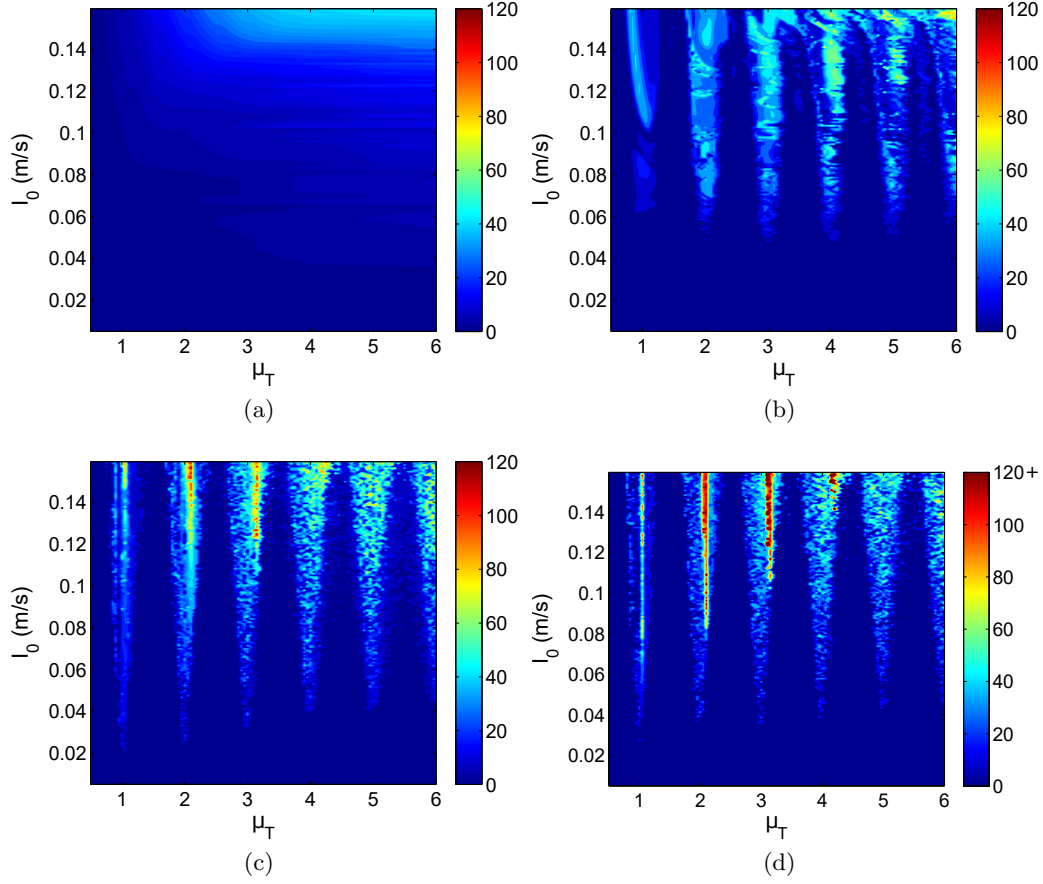


Figure 4.9: Contour plots of the total energy harvested E_h as a function of the impulse period μ_T and the amplitude of the initial velocity I_0 , measured after (a) 1, (b) 3, (c) 10 and (d) 20 impulses.

physical system with parameters listed in Table 4.2). It describes the frequency of application of the impulses as a function of the cycles of response of the LO. The energy harvesting performance is evaluated by computing the measures given by equations (3.61) and (3.62).

Figures 4.9 and 4.10 depict the total energy harvested and the energy harvesting efficiency as functions of the impulse magnitude, within the low-energy impulse domain, and of the normalized inter-arrival time μ_T in the range $(0, 6]$. The case of application of a single impulse is plotted in Figures 4.9(a) and 4.10(a). μ_T indicates in this case the normalized time of the system response; for example, $\mu_T = 6$ means a time $t = 0.7$ s, at which the amount of energy harvested is calculated. The two

contour plots confirm the results presented in Section 4.2. As expected, the amount of energy harvested depends on the excitation magnitude and on the time during which the system oscillates (Figure 4.9(a)); moreover, the efficiency is higher in the low and high impulse magnitude regions, especially in the first stage of the system motion (Figure 4.10(a)). Starting from the second impulse applied, discrete “ribs” of higher performance begin to form for discrete ranges of the impulse period, near multiples of the primary system fundamental period (Figures 4.9(b), 4.9(d) and 4.10(b), 4.10(d)), and they continue to develop with the successive pulses. The occurrence of these regions of higher performance indicates the strong dependence of the harvesting capability upon the dynamic state of the primary system when excited. In fact, the peaks occur when the primary mass is hit while performing its maximum velocity (i.e., possessing maximum kinetic energy). A steady-state condition in terms of definition of the ribs can be detected after 10 impulses, for all parameter combinations (μ_T, I_0) , with peak values of energy harvested from high-energy pulses of more than 200 mJ occurring at $\mu_T \approx 3.1$. Operating outside of the high-performance ribs reduces energy harvesting performance significantly.

The presence of sharply defined ribs of higher efficiency was found by Remick et al. in [69] for a purely cubic nonlinear system coupled to a linear primary oscillator driven by a periodic pulse train. Similarly, it can be observed for the monostable counterpart of the system under investigation herein. Hence, the comparison between the results obtained for the mono- and bistable configurations highlights the gain of the latter in terms of energy harvesting efficiency within the portions between the ribs and, mainly, the existence of a novel high-efficiency region in the regime of low-energy impulses.

This overall qualitative behavior can be examined in a more quantitative way in the plots of Figure 4.11, where the energy extracted from each impulse by the vibration harvester is averaged over 600 impulses. The mean extracted energy \bar{E}_h and presented as a function of the inter-arrival time parameter μ_T , for each of the three energy levels examined. In particular, for the high and intermediate

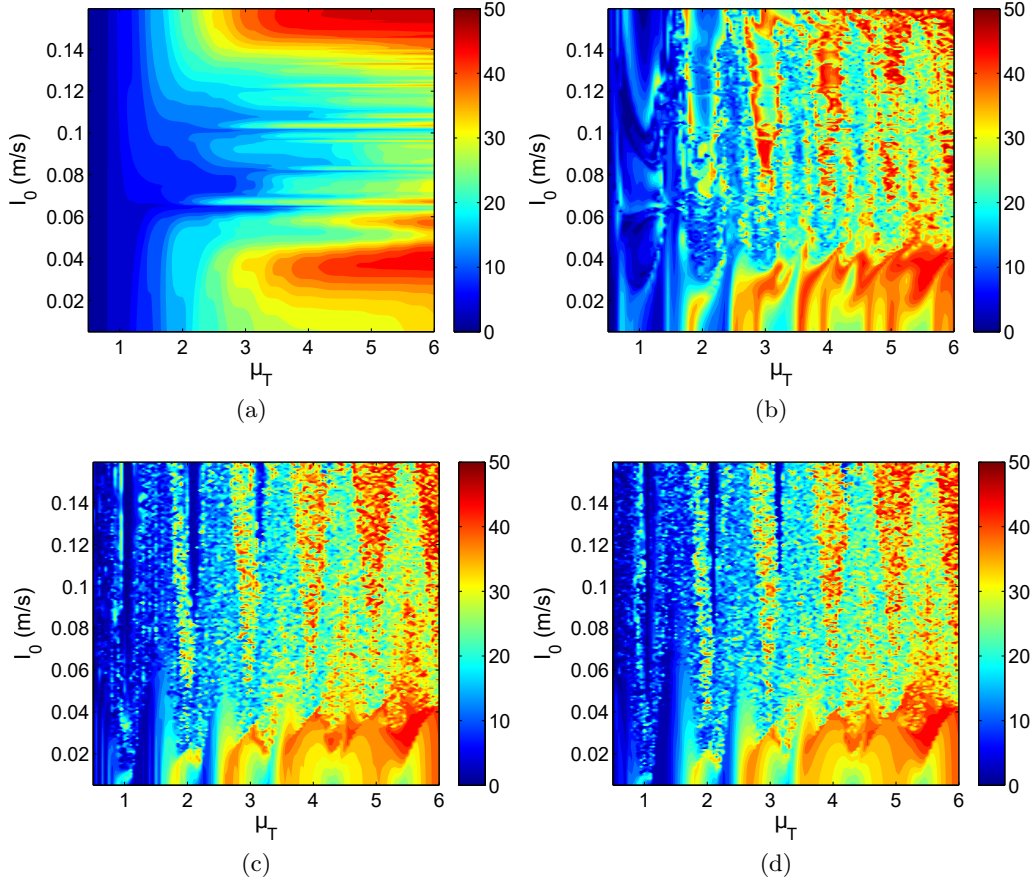


Figure 4.10: Contour plots of the efficiency $\eta\%$ as a function of the impulse period μ_T and the amplitude of the initial velocity I_0 , measured after (a) 1, (b) 3, (c) 10 and (d) 20 impulses.

impulse levels (Figures 4.11(a) and 4.11(c), respectively) the addition of bistability to the system turns out to be ineffective in close proximity to the high-efficiency ribs, whereas it is beneficial outside the ribs. The resulting average of the total amount of energy harvested is much greater for the bistable case, revealing superior robustness. For the excitation amplitude $I_0 = 0.16$ m/s, $E_h = 9.8$ mJ is achieved at $\mu_T = 4.5$ cycles, which is in the deepest part between the two consecutive ribs at $\mu_T = 4.1$ and $\mu_T = 5.2$; this performance exceeds that of the purely cubic system by more than six times, with the bistable system harvesting 61.3 mJ versus 2.5 mJ for the monostable configuration at $\mu_T = 4.3$ (Figure 4.11(a)). The peak value reaches 480 mJ of average energy harvested. Conversely, at low energies the

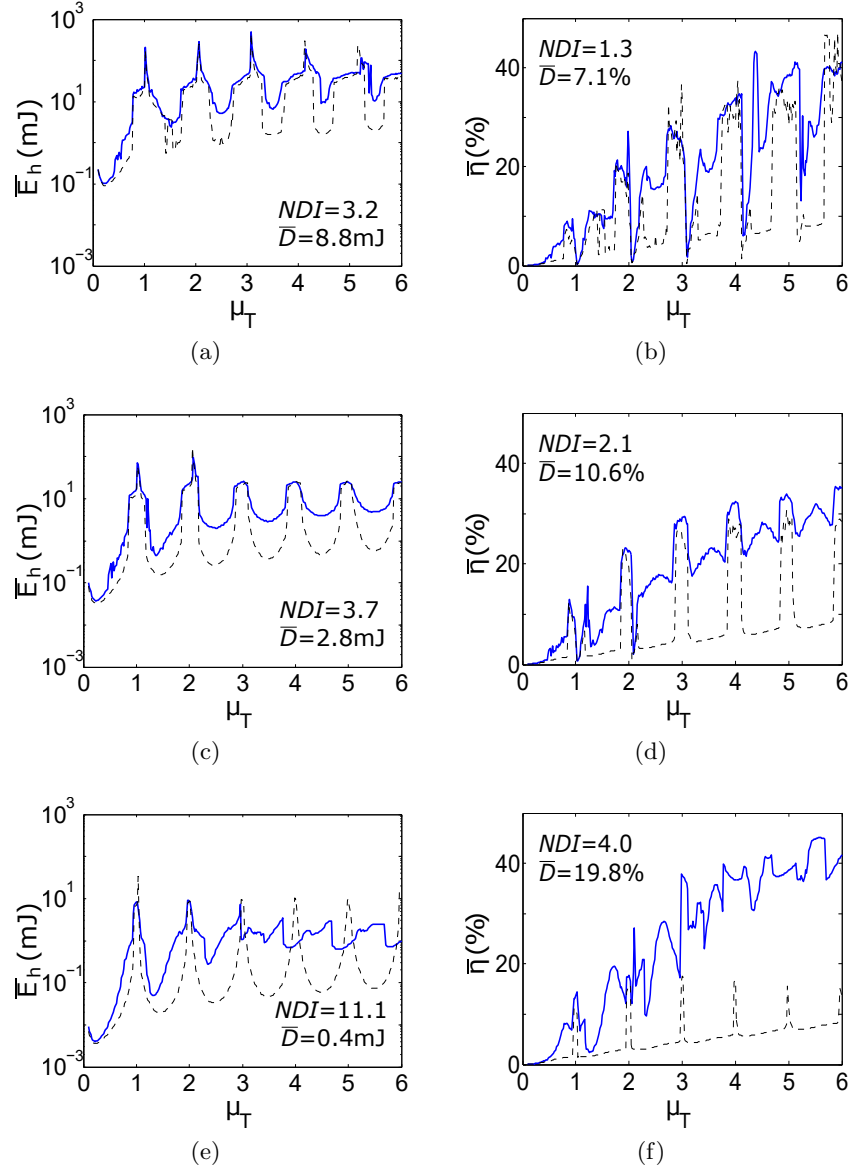


Figure 4.11: Average energy harvested \bar{E}_h in mJ and energy harvesting efficiency $\bar{\eta}\%$ as a function of the impulse period μ_T , computed for 600 impulses. (a),(b) $I_0 = 0.16$ m/s; (c),(d) $I_0 = 0.09$ m/s; (e),(f) $I_0 = 0.03$ m/s. Comparison with the monostable configuration (dashed lines).

bistable system outperforms its monostable counterpart for all impulse periods, as revealed by Figure 4.11(f), where the high-efficiency ribs mostly vanish. In the case of Figure 4.11(e), a significant enhancement in the energy harvesting capability occurs outside of the high-performance ribs (3 mJ for the bistable case, compared to 0.08 mJ of the monostable case, for $\mu_T = 3.7$), although it diminishes near the ribs (10 mJ is harvested on average by the monostable system at $\mu_T = 4$ cycles, more than ten times the energy harvested by the bistable system).

For impulse periods greater than 6, the curves of E_h show a gradual flattening, resulting in higher gain for impulse periods outside the ribs and a progressive deterioration on the ribs. This tends to an asymptotic limit because, if the inter-arrival time is large enough to let the LO and BNEH come to rest before the next impulse is applied, the mechanical energy in the primary system following the application of an impulse is completely harvested (or dissipated) before the next impulse is applied. This critical period is $\mu_T \approx 25$ cycles and coincides with the time required by the system to damp out completely. Above this value, the system response replicates the single-impulse results presented in Section 4.2. Time histories of LO and BNEH responses for this case are presented for the intermediate energy level in Figure 4.12.

Two indices are chosen to "condense" the results discussed above, namely a *normalized difference index* (NDI) and a *mean difference* (\overline{D}), defined as:

$$NDI(X) = \text{mean}\left[\frac{X_{b,i} - X_{c,i}}{X_{c,i}}\right], \quad \overline{D}(X) = \text{mean}[X_{b,i} - X_{c,i}], \quad X = \overline{E}_h, \overline{\eta}$$

where the subscriptions b and c stand for "bistable configuration" and "purely cubic configuration" respectively, and the means are intended over the i -th triad (μ_T, I_0, X) . These indices give a prompt view of the overall trend of the curves in Figure 4.11, and in particular, of the deviation between the bistable and cubic curves, and they are particularly useful for the upcoming results of Section 4.3.2 about the random pulses case, where the overcoming of one configuration over the other is less easily identifiable.

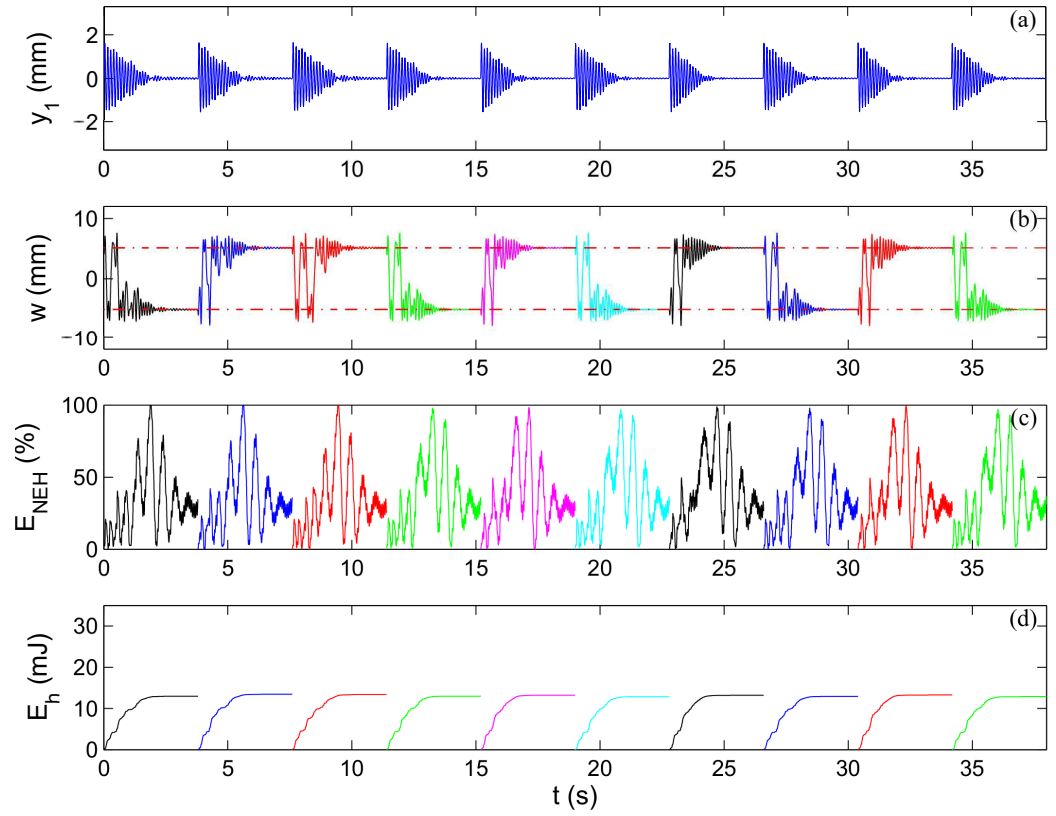


Figure 4.12: Displacement time history of LO (a) and BNEH (b); percentage of instantaneous total energy in the BNEH (c) and total energy harvested (d) for $I_0 = 0.09$ m/s and $\mu_T = 32$. Number of impulses: 10. Dashed lines represent the two equilibrium positions.

Numerical simulations of the response of the system (3.51) for several specific parameter sets (μ_T, I_0) are also reported in the next plots for the very-low-energy case. Different colors are used in the time histories to identify the consecutive applied impulses. The displacement responses of the system for $I_0 = 0.03$ m/s and $\mu_T = 2$ for the first 25 applied impulses are shown in Figure 4.13, along with the percentage of instantaneous energy in the BNEH (computed as the total energy in the BNEH divided by the total energy in the two-DOF system at time t) and the energy harvesting measure (3.61), used to compare system performance. The response of the monostable counterpart for the same parameter set is depicted in Figure 4.14. This operating condition reflects the case in which the energy harvesting capability of the bistable configuration is similar to that of the monostable one. As seen in Figure 4.13(b) the dynamics of the nonlinear oscillator is characterized by a complex motion composed of chaotic alternating cross-well and in-well oscillations. The sequence of cross-well oscillations absorbs and harvests most of the energy initially possessed by the LO (Figures 4.13(c) and 4.13(d)). However, at the same operating conditions, the purely cubic energy harvester is capable of performing high-amplitude oscillations, resulting in similar performance.

The results of the time simulation for $\mu_T = 3.7$ are shown in Figures 4.15 and 4.16 for the bistable and monostable NEH respectively. This parameter value corresponds to the region between two consecutive ribs. In-well nonlinear beating (Figure 4.15(a)) yields fast energy transfer from the LO to the BNEH, with localization of impulsive energy to the BNEH as each impulse is applied to the linear sub-system (Figure 4.15(c)). This operating regime corresponds to good energy harvesting performance in which energy is quickly harvested for the entire duration of each response. Figure 4.16 shows the poor performance of the monostable counterpart. Note that some scales have been changed for the sake of readability. Finally, the response for $\mu_T = 4$ is presented in Figures 4.17 and 4.18, where the monostable system performance overcomes the bistable one. As each impulse is

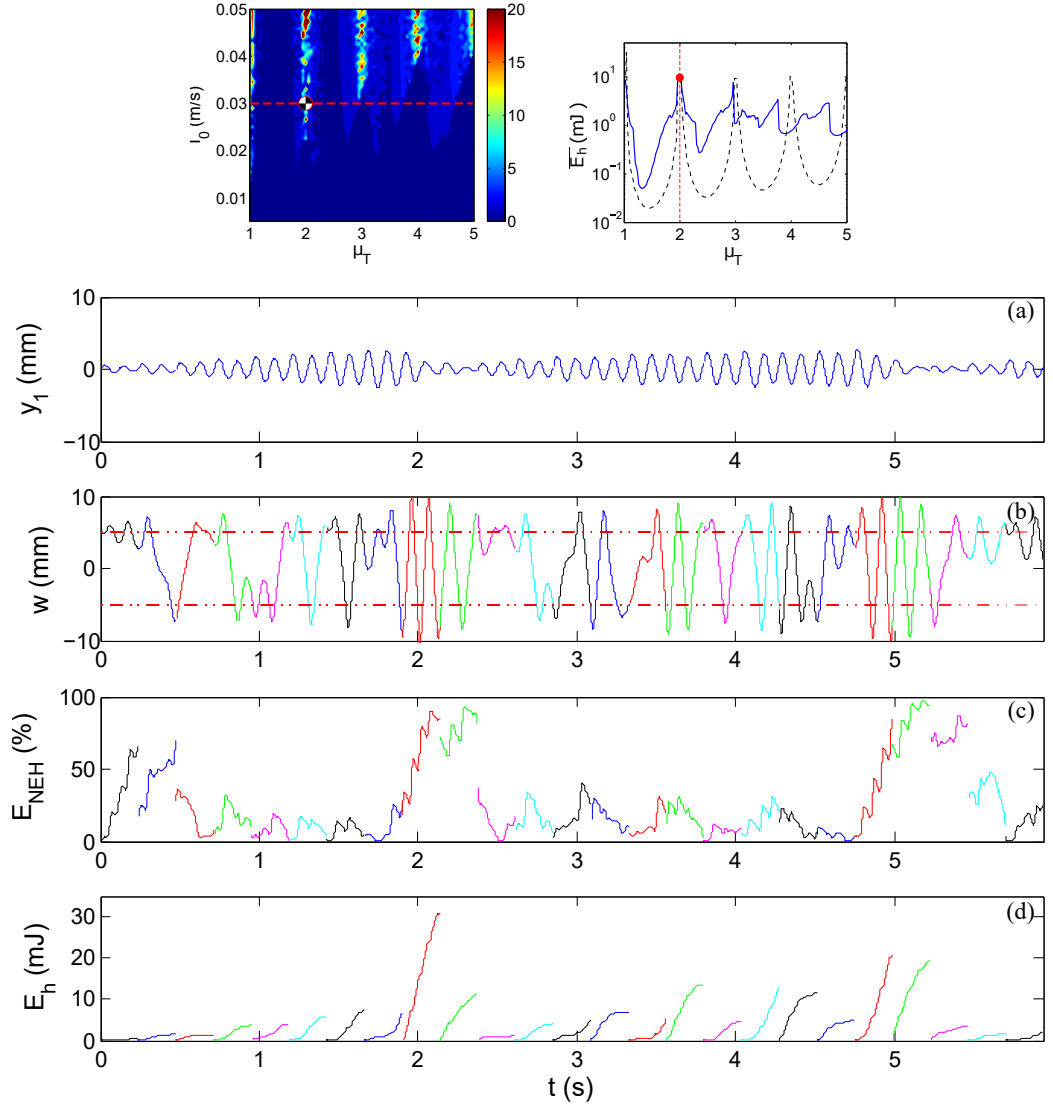


Figure 4.13: Bistable system response for $I_0 = 0.03 \text{ m/s}$ and $\mu_T = 2$: displacement time history of LO (a) and BNEH (b); percentage of instantaneous total energy in the BNEH (c) and total energy harvested (d). Number of impulses: 25. Dashed lines represent the two equilibrium positions.

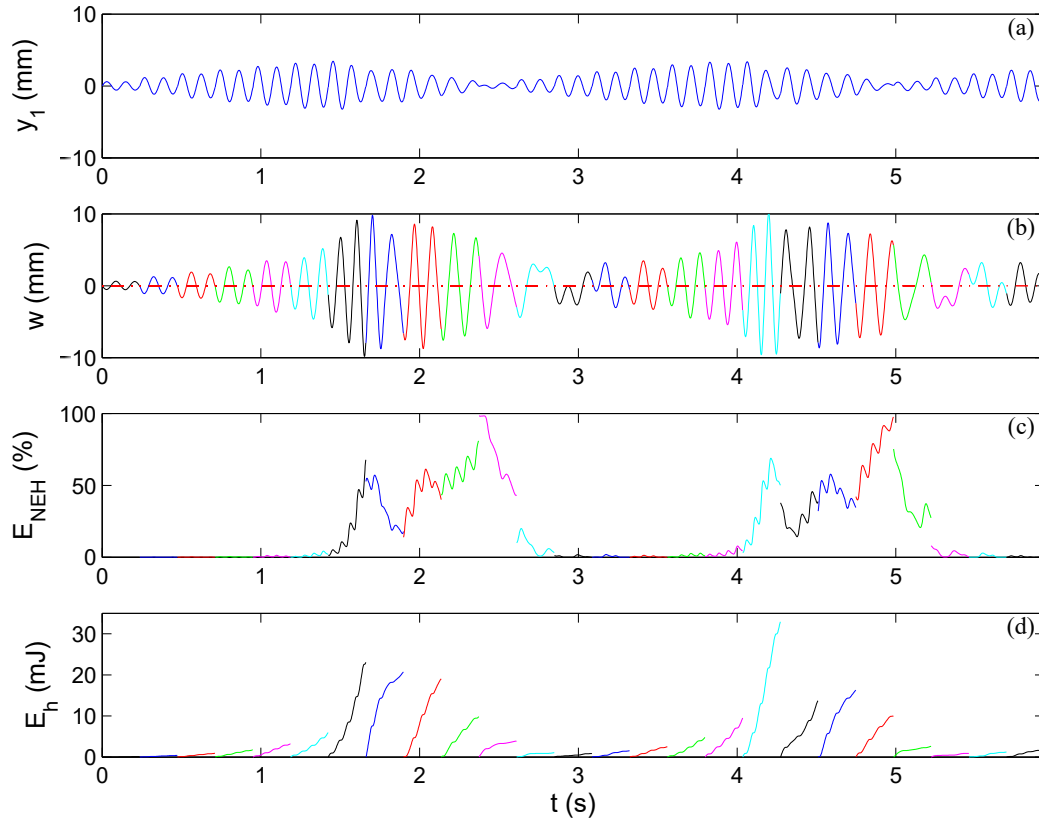


Figure 4.14: Monostable system response for $I_0 = 0.03 m/s$ and $\mu_T = 2$: displacement time history of LO (a) and monostable NEH (b); percentage of instantaneous total energy in the NEH (c) and total energy harvested (d). Number of impulses: 25.

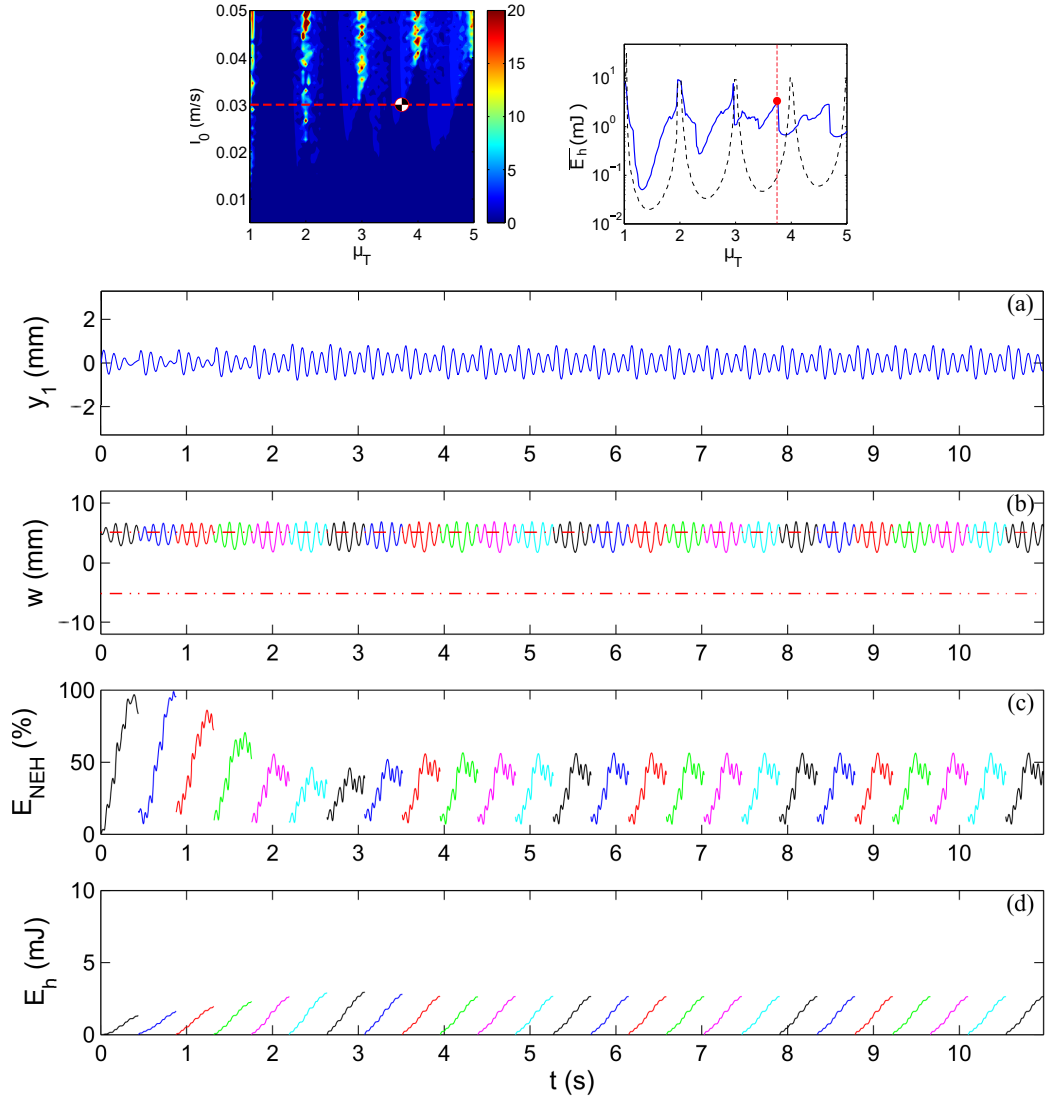


Figure 4.15: Bistable system response for $I_0 = 0.03$ m/s and $\mu_T = 3.7$: displacement time history of LO (a) and NEH (b); percentage of instantaneous total energy in the BNEH (c) and total energy harvested (d). Number of impulses: 25. Dashed lines represent the two equilibrium positions.

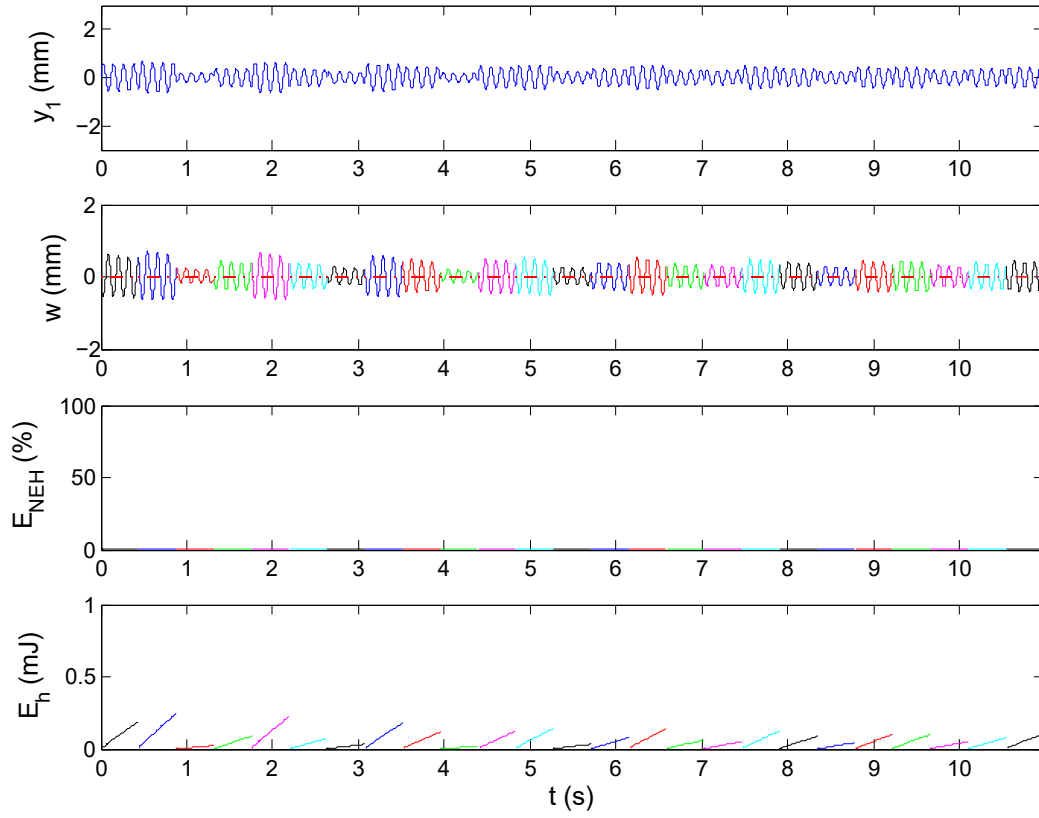


Figure 4.16: Monostable system response for $I_0 = 0.03m/s$ and $\mu_T = 3.7$: displacement time history of LO (a) and NEH (b); percentage of instantaneous total energy in the NEH (c) and total energy harvested (d). Number of impulses: 25.

applied to the primary mass, a fast energy transfer from the LO to the BNEH occurs and the energy localizes to the BNEH; it is then released back to the LO half a period after of application of the impact. The motion is confined around one of the two stable equilibrium positions. Inside the potential well, nonlinear beats take place. The high efficiency is confirmed by the higher oscillation amplitude of the attachment compared to that of the linear oscillator, but the total energy harvested is modest if compared to the monostable case (Figure 4.18).

4.3.2 Random impulses scenario

The numerical investigation has been also extended to random pulse trains. Generally, a train of pulse-like random excitation can be described as a shot noise process, or Poisson noise process, and is described by the superposition of random pulses arriving independently at random times, as follows:

$$F(t) = \sum_{k=1}^{N(t)} F_k w(t - t_k) \quad (4.2)$$

where F_k is a sequence of independent random variables of the magnitude of the k^{th} impulse, and $w(t - t_k)$ is the so-called *noise function*, a non-random (deterministic) function describing the shape of the pulses. For the case of impulsive noise process, the pulse-shape function $w(t - t_k)$ in Equation (4.2) is a unit impulse, meaning a Dirac delta function $\delta(t - t_k)$. $N(t)$ is assumed to be a Poisson process. A Poisson process is a simple and widely used stochastic process for modeling the times at which arrivals enter a system. Thus, the random variable $N(t)$, $\forall t > 0$, is the number of arrivals in the time interval $(0, t]$, described by the Poisson discrete probability mass function:

$$P_{\{N(t)\}}(n) = e^{-\lambda t} \frac{(\lambda t)^n}{n!}, \quad n = 0, 1, \dots, \infty$$

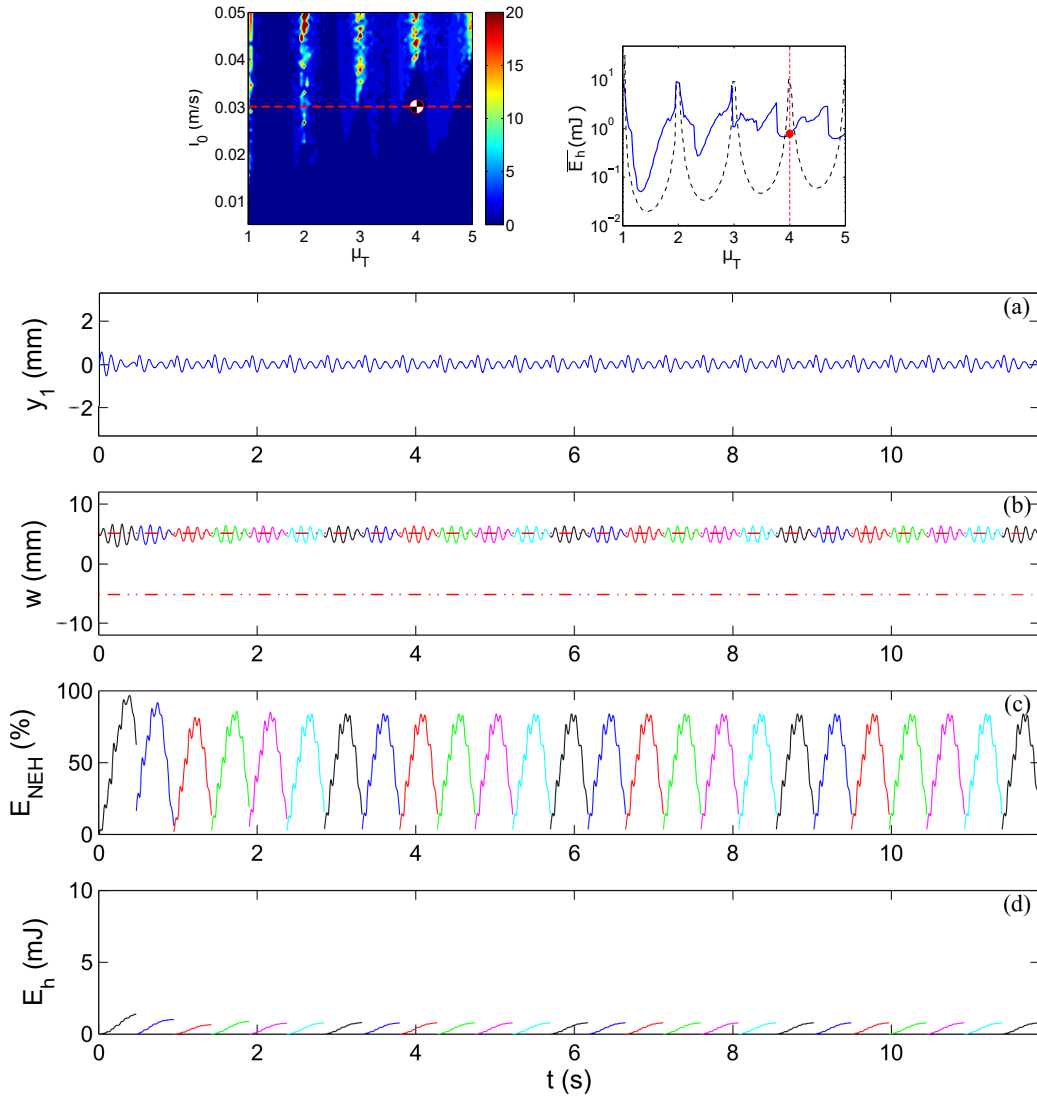


Figure 4.17: Bistable system response for $I_0 = 0.03$ m/s and $\mu_T = 4$: displacement time history of LO (a) and BNEH (b); percentage of instantaneous total energy in the BNEH (c) and total energy harvested (d). Number of impulses: 25. Dashed lines represent the two equilibrium positions.

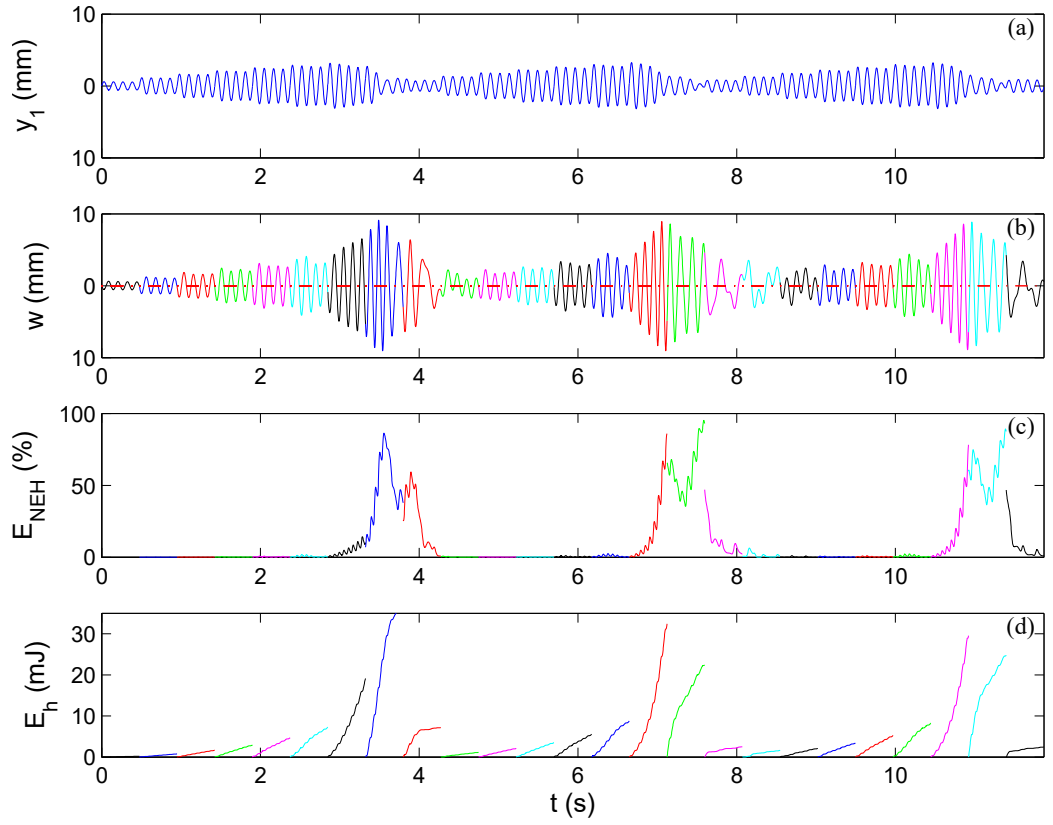


Figure 4.18: Monostable system response for $I_0 = 0.03 \text{ m/s}$ and $\mu_T = 4$: displacement time history of LO (a) and NEH (b); percentage of instantaneous total energy in the NEH (c) and total energy harvested (d). Number of impulses: 25.

where λt is the expected number of occurrences in the time interval of size t . The Poisson process is completely characterized by the average pulse arrival rate λ of events, i.e. the expected number of events (impulses) per unit time (mean and variance are $\mu_P = \sigma_P^2 = \lambda t$). t_k 's are the arrival times for the Poisson counting process $N(t), t > 0$.

In the Poisson process, time intervals $X_k = t_{k+1} - t_k$ between two subsequent pulses (X_k : random variable of the waiting time) have an exponential distribution [91], the probability density function of which is:

$$p_{\{X\}}(x) = \lambda e^{-\lambda x}, \quad x \geq 0$$

where λ is the arrival rate of the process. Mean and variance are $\mu_X = 1/\lambda$ and $\sigma_X^2 = 1/\lambda^2$, respectively (Figure 4.19(a)).

The F_k 's are identically distributed random variables, mutually independent and independent of the distribution of the pulse arrival time t_k . The distribution for the variables F_k is chosen to be the Rayleigh distribution, whose probability density function is given by:

$$p(n) = \frac{n}{b^2} e^{-\frac{n^2}{2b^2}}$$

with mean $\mu_R = b\sqrt{\pi/2}$ and variance $\sigma_R^2 = (2 - \pi/2)b^2$ (Figure 4.19(b)). The impulsive-noise model given by Equation (4.2) is a white noise.

Finally, μ_R represents the average amplitude of the impulses (it will be named \bar{I}_0) and μ_X the average interarrival time, i.e. $\mu_T = \mu_X/T_1$ ($\mu_X \equiv \bar{\Delta t}_p = \mu_T T_1$). Figure 4.20 shows a realization of the Poisson-distributed impulse train.

The response and performance of the system under stochastic impulsive excitation is investigated by examining separately the effect of random amplitudes, keeping the interarrival time constant, and the effect of random waiting times with constant amplitudes.

Figure 4.21 depicts the average energy harvested \bar{E}_h in mJ and average energy harvesting efficiency $\bar{\eta}\%$ over 600 pulses, for the system subject to trains of period-

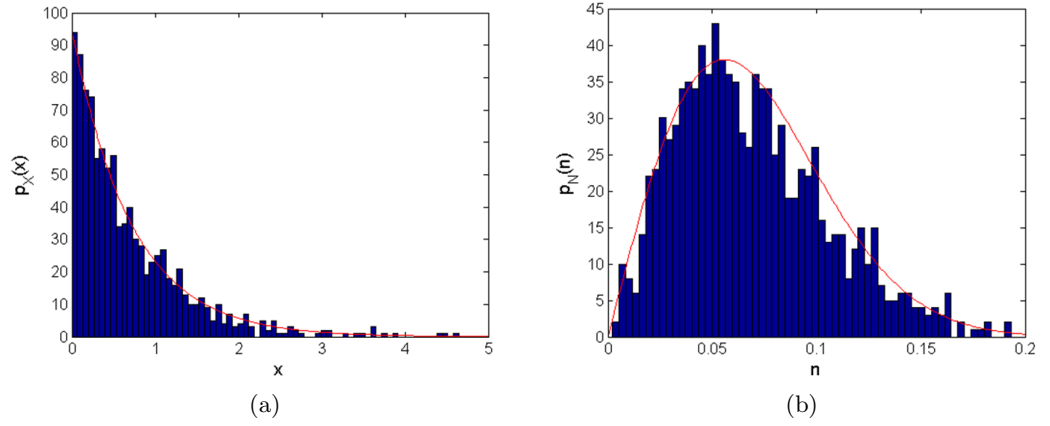


Figure 4.19: Exponential distribution for the waiting times $\mu_T = 6$, $\mu_X = \sigma_X = 0.07$ (a) and Rayleigh distribution for the impulse amplitudes: $N = 1000$, $\mu_R = 0.07$, $b = 0.06$ (b).

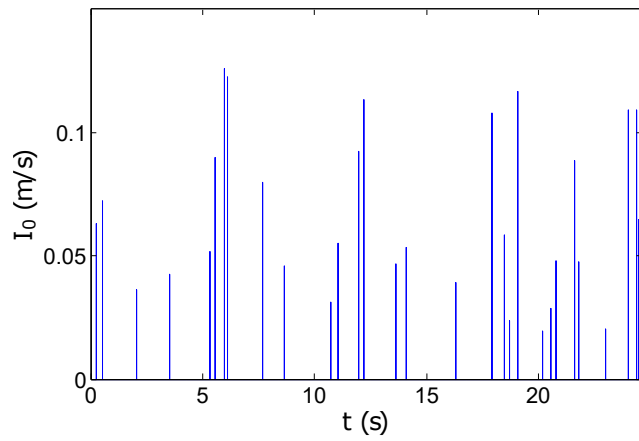


Figure 4.20: Random pulse train as Poisson process, with Rayleigh distributed magnitudes: $\bar{I}_0 = 0.07$ m/s, $\mu_T = 6$.

ically repeated impulses with random magnitudes. The three cases corresponding to the low, intermediate and high energy levels respectively are considered with reference to the mean value of the impulse magnitude \bar{I}_0 .

It becomes apparent from Figures 4.21(a) that the stochasticity of the impulse magnitude allows a significant enhancement of the total energy extracted by the system in the higher energy regime, with respect to the periodic case, regardless the type of configuration (mono- or bi-stable) of the harvesting device. A slight enhancement from the bistable system can be also seen in comparison to the monostable case (note that the y-axis of the graphs has a logarithmic scale). Conversely, in the lower energy regime (Figure 4.21(e)), the gain of energy harvested by the bistable device compared to the monostable case becomes considerable. The second evidence regards the appreciable improvement provided by the random distribution of the impulse amplitude, occurring for both the intermediate and low energy scenarios (Figures 4.21(c) and 4.21(e)), respectively, at very low values of μ_T (slow arrival time).

The effect of random interarrival time of the impulses on the harvesting performance is evaluated by varying the standard deviation of the interarrival times (i.e. from a maximum value to zero, which corresponds to the case of uniform intervals). In order to do this, the arrival time intervals are computed as the summation of a constant rate Δt^c and a random rate Δt^r . By letting the mean of Δt ($\overline{\Delta t}$) be constant (for each μ_T it is $\overline{\Delta t} = \Delta t_p = \mu_T T_1$), and varying the rate of each contribution to $\overline{\Delta t}$, that is:

$$\overline{\Delta t^r} = \alpha \overline{\Delta t}, \quad \Delta t^c = (1 - \alpha) \overline{\Delta t} \rightarrow \overline{\Delta t} = \Delta t^c + \overline{\Delta t^r}$$

the distribution of the interarrival times has mean $\overline{\Delta t}$ and standard deviation the standard deviation of the random part. The multiplier $\alpha \in [0; 1]$ defines the deviation from the periodic intervals, which occurs for $\alpha = 0$. As α increases, the standard deviation, as well as the mean of the random part, increases. By inspecting the results with varying α , the occurrence of random intervals seems to

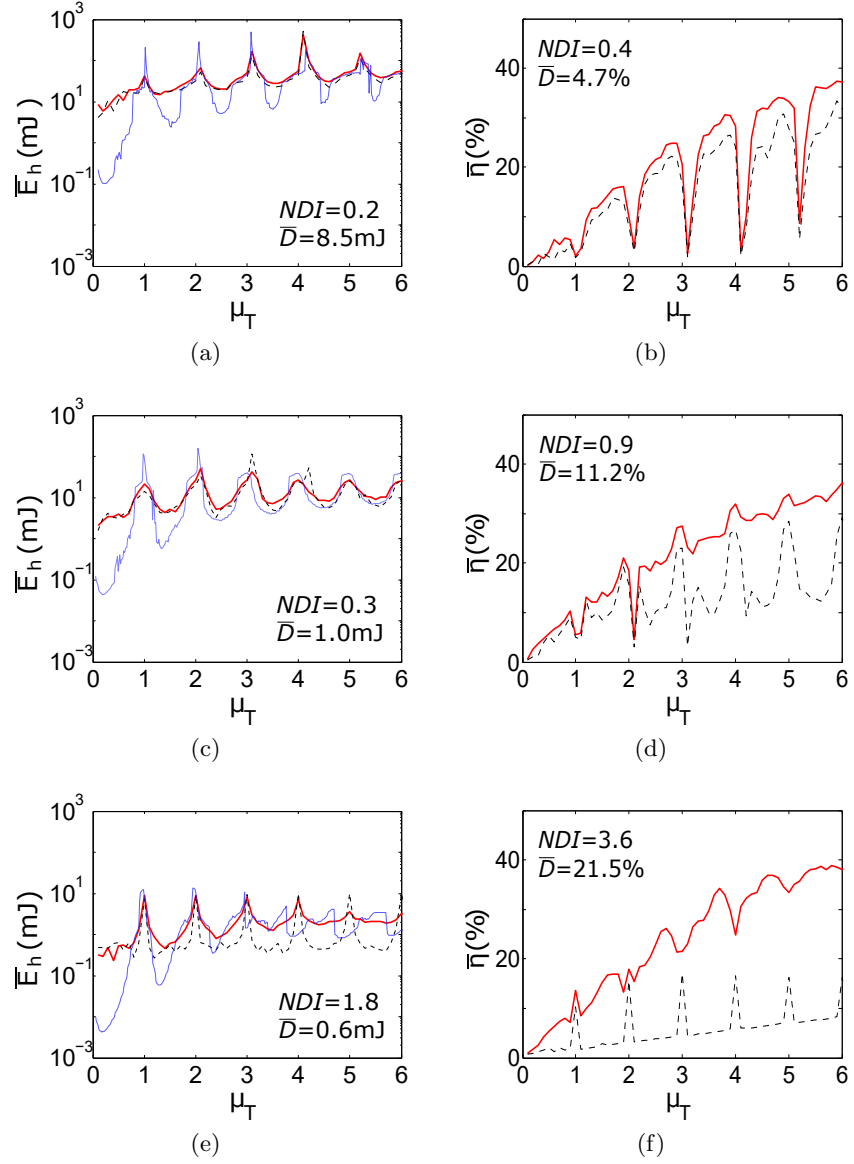


Figure 4.21: Average energy harvested \bar{E}_h in mJ and energy harvesting efficiency $\bar{\eta}\%$ as a function of the impulse period μ_T , computed for 600 impulses. (a),(b) $\bar{I}_0 = 0.16$ m/s; (c),(d) $\bar{I}_0 = 0.09$ m/s; (e),(f) $\bar{I}_0 = 0.03$ m/s. Comparison with the monostable configuration (dashed lines) and with the periodic case for the bistable configuration (blue lines).

deteriorate progressively the response of the system, as α increases. The graphs for $\alpha = 1$ are depicted in Figure 4.22. The presented curves result from a process of piecewise averaging and further interpolation (with 'spline' interpolation method) of the original curves with the purpose of achieving smoother curves to extrapolate the overall trend and allow a better interpretation of the results. The values of NDI and \bar{D} confirm a better performance of the bistable configuration, compared to the monostable one. However, it should be noted that the raw graphs present values of the energy harvesting efficiency and mean total energy harvested per impulse that are highly variable with respect to the impulse period (or μ_T), denoting low robustness and reliability of the harvester.

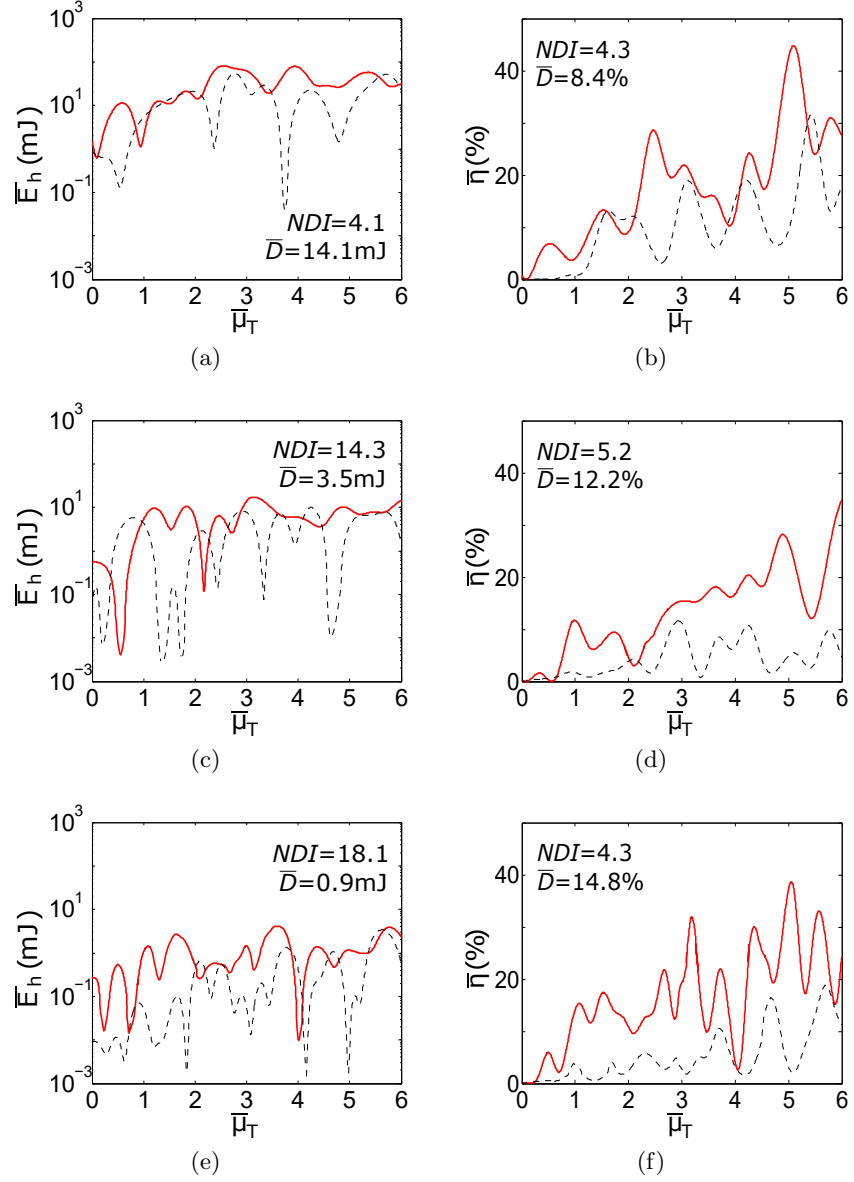


Figure 4.22: Average energy harvested \bar{E}_h in mJ and energy harvesting efficiency $\bar{\eta}\%$ as a function of the average impulse period $\bar{\mu}_T$, computed for 600 impulses. (a),(b) $I_0 = 0.16$ m/s; (c),(d) $I_0 = 0.09$ m/s; (e),(f) $I_0 = 0.03$ m/s. Comparison with the monostable configuration (dashed lines).

Chapter 5

Experimental study

The main results of experimental tests on an electromagnetic bistable energy harvesting system coupled to a hosting primary mass are presented herein. This novel experimental apparatus proves the superior energy harvesting ability of this system compared to a more conventional cubic nonlinear energy harvester.

5.1 Experimental setup

A bistable nonlinear electromagnetic energy harvester coupled to an impulsively excited primary linear oscillator has been experimentally investigated. The experimental campaign was carried out in the Mechanical Engineering Laboratory of the University of Illinois at Urbana-Champaign.

The experimental apparatus is presented in Figure 5.1.

The hosting structure, representing the linear primary system, is a frame consisting of a HDPE mounting mass, which holds eleven steel plates used to achieve the desired mass. It is grounded to an optical table via two thin spring steel vertical flexures, which provide for the linear stiffness and light viscous damping. A blue-tempered steel beam with its supports (in Figure 5.2(a)) and an inductance copper coil with aluminum mounting bracket contribute to the total mass of the primary

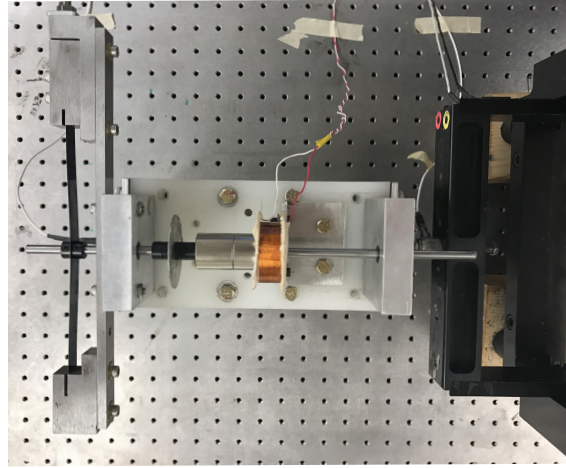
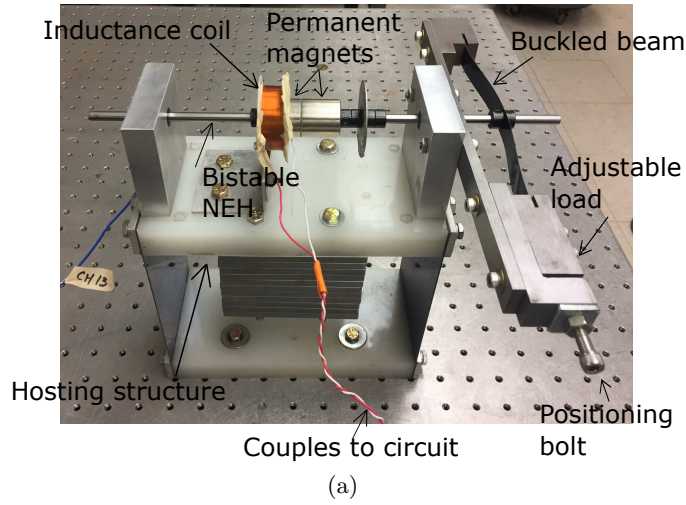


Figure 5.1: Photograph of the experimental apparatus of the energy harvesting system (top view in (b)).

system. The bistable nonlinear energy harvesting system (BNEH) is composed of two permanent magnets, collar mounts and a steel rod, which slides within two linear ball bearings embedded in the aluminum uprights fixed at the ends of the HDPE mounting mass (Figure 5.2(b)). The damping in the coupling arises mainly from the interaction of the rod with the bearings. As known, damping arising from bearings can be conveniently considered as a linear viscous damping, that is to say, proportional to the velocity [92], rather than Coulomb damping.

The mechanical coupling between the linear system (LO) and the BNEH is provided

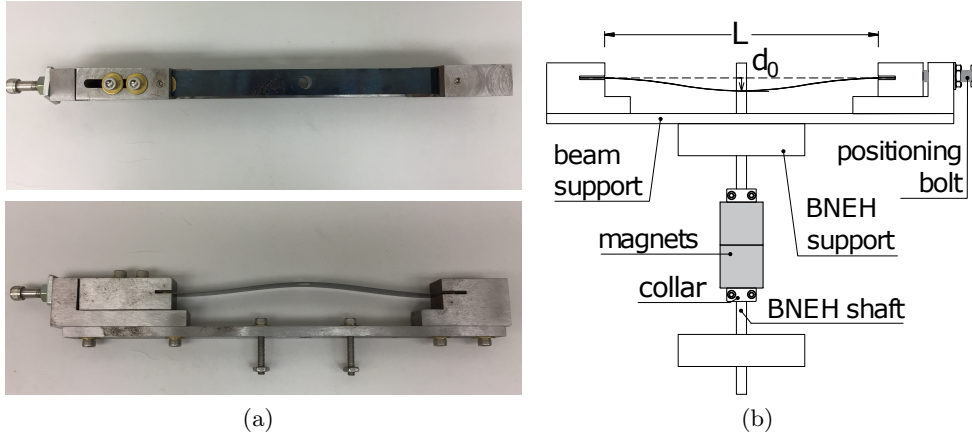


Figure 5.2: Photograph of the beam support (a) and sketch of the coupled harvesting device (b).

by the blue-tempered steel slender beam with Young modulus $E = 200$ GPa, which is physically connected at its midspan to the BNEH mass via two collar mounts. Other collar mounts are placed to precisely hold the permanent magnets in place. The beam is clamped at both ends. It has a thickness of 0.2 mm, height 15.8 mm and length of 165 mm. The transverse deflection resulting from the orientation of the beam perpendicular to the direction of motion of the harvester mass, gives rise to a cubic stiffness nonlinearity. The bistability, i.e., the negative stiffness around the equilibrium position, is realized by exploiting the buckling of the slender beam subject to an axial compressive force, which slightly exceeds the Euler's critical load. The buckled beam, in fact, possesses limit points in the equilibrium path such that, under the critical load, a snap-through instability takes place. A positioning bolt is properly tightened to adjust the compressive force, or, equivalently, the initial static deflection of the beam.

As for the electromechanical coupling, the inductance coil is fixed at the LO frame, so to act as the stator, while the magnet composing the BNEH mass will be moving relatively to it. The coil is constructed within a HDPE spool of inner radius $r_i = 14$ mm. The coil is wrapped into 819 turns to achieve a thickness of $h_c = 16$ mm and outer radius $r_o = 20$ mm, which provides the desired electromechanical coupling. Size and number of turns of the coil assure the assumption made in Section 3.3,

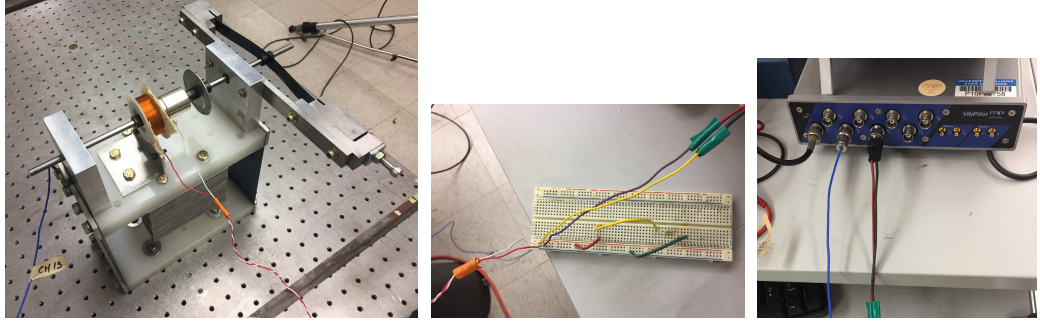


Figure 5.3: Photographs of the electrical circuit.

according to which the coil inductance L_c , calculated as (3.45), and hence the coil impedance Z_c (recall (3.46)), are negligible. The coil was wound by while striving to maintain an orthogonal fill factor. The fill factor encompasses tightness of winding, insulation thickness and winding shape, which essentially determines the efficiency of the coil. The orthogonal fill factor physically describes coil winding in which each new turn of wire lies directly on top of the wire turn below it and perfectly in line with the wire turn next to it and corresponds to a coil efficiency of $\approx 80\%$. Enameled AWG 30 copper wire is used to maximize turns, in order to improve the electromagnetic transduction, while minimizing coil resistance, which adds additional linear viscous damping to the system without the benefit of contributing to energy harvesting output. Two cylindrical neodymium (NdFeB) permanent magnets, with 25.4 mm outside diameter and 25.4 mm length, are placed together to create a uniform magnetic field within the coil. Neodymium magnets have higher magnetic flux output per unit volume than other types; the selected magnets provide a flux density of $B = 1.32$ T. The coil leads are soldered to longer wires, connected to a breadboard and placed in series with a simple resistor of resistance $R_L = 47\ \Omega$, which allows the power to be extracted from the harvesting device and the induced current to circulate in the coil (Figure 5.3). It is worth mentioning the relevance of the position of the coil relative to the lines of force of the magnetic field generated by the magnet. According to Faraday's law, the electromotive force induced by the relative motion between the magnet and the

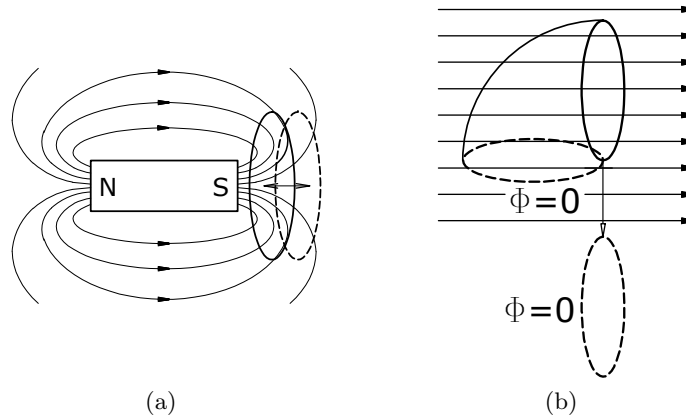


Figure 5.4: Change of magnetic flux concatenated to the circuit.

coil of conducting wire (induced voltage) is directly proportional to the time rate of change of the magnetic flux concatenated to the circuit, that is the magnetic flux passing through the imaginary surface bounded by the wire loop. Changes that occur entirely outside the region enclosed by the coil cannot affect it. Hence, the circuit must cut the lines of induction of the field, in order to vary the number of lines of induction enclosed into the circuit during the relative motion of the wire loop with the magnet. This can happen, for example, by axially moving wire loop and magnet relative to each other, when the first is in a close proximity to the latter (Figure 5.4(a)) or by rotating the coil or extracting it from the field, in the case of uniform field (Figure 5.4(b)). With reference to the first of the two configurations, which is employed in the specific rig, the coil must be moved rapidly and in close proximity to the magnet in order to maximize the induced voltage. On the contrary, if at the center of the magnet, it will not experience significant changes of magnetic flux as the field lines are approximatively parallel to the direction of relative motion. Moreover, as known, the magnetic field is strongest near to the poles of the magnet where the lines of flux are more closely spaced.

The graph in Figure 5.5 describes the dependence of the voltage upon the position of the coil relative to the magnet. The curve is constructed experimentally by

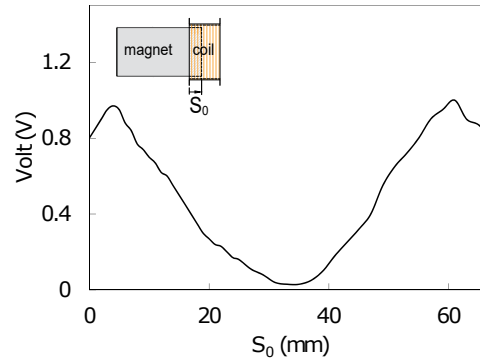


Figure 5.5: Output voltage as a function of the position of the coil relative to the magnet.

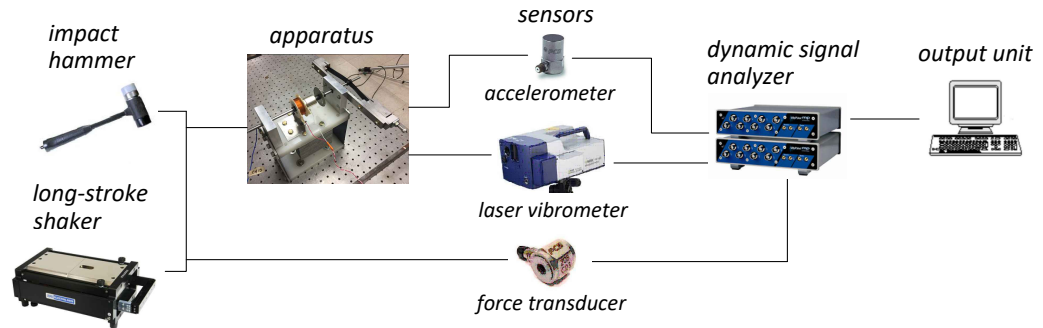


Figure 5.6: Block diagram of the instrumentation.

recording the peak of the voltage across the load resistance resulting from the application to the BNEH of a controlled displacement and velocity time series, varying the initial position of the magnet of 1 mm for each measurement. For $S_0 = 0$, the oscillating magnet is fully outside the coil and its edge is aligned with the side of the coil. The maximum output voltage occurs when the magnet is initially inserted into the cavity of the coil at 4 mm, whereas the minimum potential difference is experienced when the center of the coil coincide with the center of the magnet.

The described coupled system has been tested under isolated and periodically repeated impulses applied to the linear sub-system, within a range corresponding to an initial velocity spanning (0.05; 0.4) m/s. Figure 5.6 shows the block diagram of the instrumentation. Single impulsive forces are applied to the linear oscillator by use of an instrumented PCB 086D20 modal hammer with a plastic tip with the

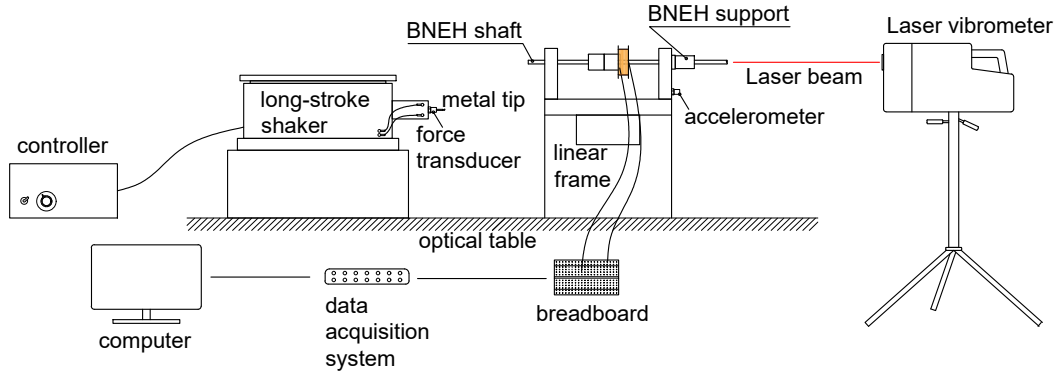


Figure 5.7: Set-up of the experimental test.

system initially at rest. Trains of periodically repeated impulses are applied to the primary system by use of an APS Dynamics Model 400 long-stroke electromagnetic shaker. The stinger, fixed to the crosshead armature of the shaker, strikes the linear oscillator and a PCB 208C05 force transducer, mounted on the stinger, measures precisely the excitation force time history. The input frequency and voltage levels are adjusted until the desired impulse period and excitation magnitude are obtained. A customized square waveform is input into the shaker controller, namely a positive half-square wave, which applies a fast impulsive force, similar to the impulse imparted by the modal hammer in the single impulse excitation scenario, followed by a negative half square wave, which aims to quickly retract the shaker armature and stinger, in order to avoid undesirable double impacts to the excited structure. Elastic bands inside of the shaker are adjusted to precisely control the separation between the primary system and stinger tip prior to the application of each impulse. They bring the stinger back to the prescribed separation before the next impulse is applied. The average width of the half-sine pulse provided by both the modal hammer and the shaker tip was ≈ 3 ms, thus it well approximates the Dirac function. For this reason, the excitation magnitude can be equivalently defined in terms of initial velocity I_0 of the primary system directly following the impulse. Time series measurements of the BNEH absolute velocity are recorded using a Polytec PSV laser vibrometer with a sampling frequency of $f_s = 12.8$ kHz while

a PCB accelerometer with sensitivity 100 mV/g is used to measure accelerations of the primary system. Voltage time histories measurement taken across the load resistance are recorded to compute the output power from the harvesting device, as $P = V^2/R_L$, with R_L the load resistance, so that the energy harvested is calculated by integration from the power. The data acquisition is synchronized by means of a small pre-trigger of duration 196 ms. The synchronization of the measurement of the system response is important for accurate computation of the relative velocity by eliminating any phase mismatch between the measurements. Figure 5.7 pictures the set-up for energy harvesting measurements.

The time series data are then post-processed: low-pass filters are used to attenuate the noise in the raw signals and acceleration measurement is numerically integrated to obtain absolute velocity of the linear oscillator. A high-pass filter with cut-off frequency of 3 Hz is applied to this velocity in order to remove the low-frequency contamination [93]. The wavelet spectra are computed during post-processing from the velocity time series data.

5.2 Design and system identification

Aiming mainly at validating the numerical evidence of Chapter 4 rather than maximizing the energy harvesting capability of the bistable device, the experimental campaign was carried out starting from an existing experimental apparatus. The main goal of the experimental tests was, in fact, to validate the theoretical model in its capacity as a predictive design tool for bistable energy harvesters. This resulted in some restrictions and feasibility limits and conditioned the concept design of the coupling between primary structure and energy harvester, being the connection system between the two masses assigned. The stiffness and damping coefficients in the coupling were physically difficult to adjust; therefore, the current system as built is non-optimized; optimal parameters for best energy harvesting performance resulted from the parametric analysis of the system (3.52) carried out in Section 4.1. Operatively, given the mass m_2 of the BNEH, the mass m_1 of the hosting frame

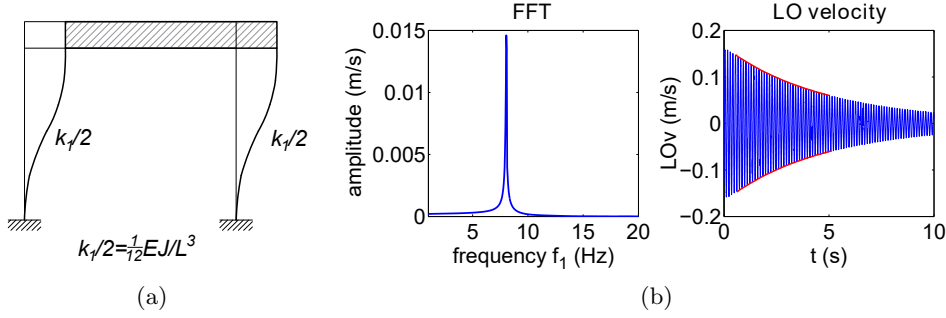


Figure 5.8: Linear oscillator design and subsequent identification.

was adjusted in order to obtain a mass ratio $m_2/m_1 \approx 4\%$, which was deemed as reasonable for practical applications. The steel vertical flexures were designed so to achieve a natural frequency for the LO of ≈ 8.2 Hz, adopting a simple shear-type model, for which the lateral stiffness is given by $2 \times 12EJ/l^3$ (Figure 5.8(a)). Once assembled, linear modal analysis was performed in order to identify the values of the coefficients b_1 and k_1 . The linear stiffness coefficient was identified by measuring the structure response under an initial non-zero displacement and zero initial velocity, and computing the frequency spectrum to extract the natural frequency. Logarithmic decrement method was used to identify the damping ratio (Figure 5.8(b)). The Restoring Force Surface (RSF) method confirmed the experimentally estimated parameters. This method has a more general applicability and is commonly adopted for nonlinear system identification purposes. It consists of measuring the time histories of the acceleration $\ddot{x}(t)$ of the one dof system and of the excitation $F(t)$, which enable to compute the time history of the (generally speaking, nonlinear) restoring function G_{RF} , defined from the one-dof system equation of motion $m\ddot{x} + G_{RF}(x, \dot{x}) = F(t)$, hence $G_{RF}(x, \dot{x}) = F(t) - m\ddot{x}$ and, ultimately, estimating the restoring force surface \tilde{G}_{RF} by an approximate function expressed (provided that non-linearity does not involve cross-product terms) as the summation of two orthogonal polynomials $g(x)$ and $h(\dot{x})$ ($\tilde{G}_{RF} = g(x) + h(\dot{x})$). For linear oscillator, the RFS is a plane in the space x, \dot{x}, G_{RF} (Figure 5.9) the latter functions simply result in $g = k_1x$ and $h = b_1\dot{x}$ (Figures 5.10(a) and 5.10(b)).

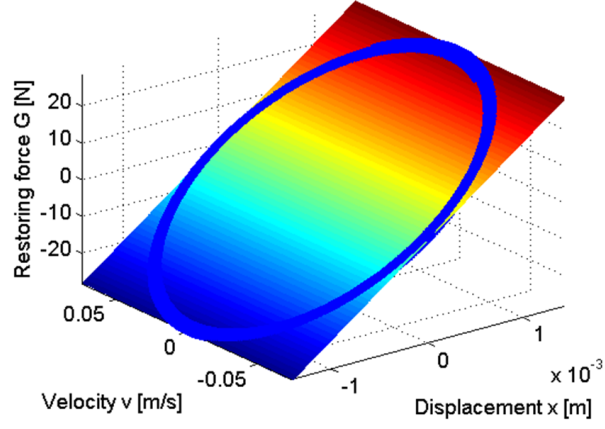


Figure 5.9: RFS approximation \tilde{G}_{RF} to the experimental data (blue dots) for the linear system.

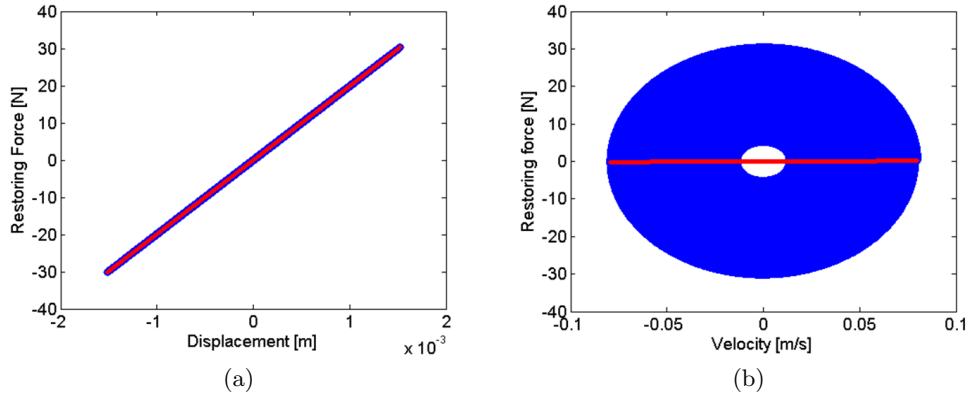


Figure 5.10: State-variable plot for the linear system. Blue line: experimental data, red line: computed restoring force.

respectively). The curve fitting is here performed using the Least Square method. The identified LO damping b_1 revealed higher than the optimal one (cfr. Table 4.2); nevertheless, the variation of this parameter has no significant effect on the overall response and energy harvesting performance of the system.

With regard to the energy harvesting device, the objective was to attain a linear stiffness coefficient k_3 such that $k_3 m_1 / (k_1 m_2) = -0.6$, hence $k_3 \approx -513$ N/m. The dimensional one-dof analytical model from Section 3.2.2 was used for the pre-dimensioning of the beam. For a beam with dimensions 165×15.8 mm and 0.2 mm thick with an initial deflection at the midspan of 0.55 mm, the parameters computed

as in (3.33) result: $m = 1.52 \times 10^{-3}$ kg, $k_2 = 1.70 \times 10^9$ N/m³, $k_3 = -515$ N/m. Once designed the beam with its support (see drawings of Figure 5.11) and fabricated and assembled the whole system, the identification of the BNEH stiffness and damping coefficients has been refined by fitting experimental acceleration and velocity time histories and corresponding FFTs with the same output of the numerical model (3.52), as, for example, in Figure 5.12. Practical limitations were encountered in adjusting the initial deflection of the beam: a small axial load yields the beam to snap to the buckled configuration with a rise at the midspan of 2.5 mm. Hence, the development of a finite element model (FEM) of the thin beam was deemed to be necessary to either confirm or adjust the parameters experimentally identified. The FEM was developed in Abaqus environment and a multiple-step nonlinear static analysis carried out to characterize the mechanical behaviour in the transverse direction and extract the force-displacement nonlinear relationship. Operationally, the finite element analysis (FEA) involved two subsequent steps. First, the buckled configuration is obtained by applying to the initially straight beam a compressive axial load of maximum magnitude greater than the first critical buckling load; a small initial imperfection has been introduced to initiate the instability. The second step applies to the buckled beam at the desired configuration (here, in particular, when the span deflection is of 2.5 mm, which is the deflection set in the experiment) and consists of applying a transverse load at the midspan section, causing the snap-through instability to occur and the other stable position to be reached. Consistently, the starting point for the second step was the deformed state at the end of the first step, as in Figure 5.13. Figure 5.14 locates the starting point of the second step on the buckling curve relative to the imperfect beam. The theoretical critical load is 3.05 N.

Because of the unstable nature of the snap-through problem (the tangent stiffness from the load-displacement response curve changes signs when system changes its stability status), the classical Newton's method performs poorly in this situation because the corrections for approaching equilibrium solutions during iterations

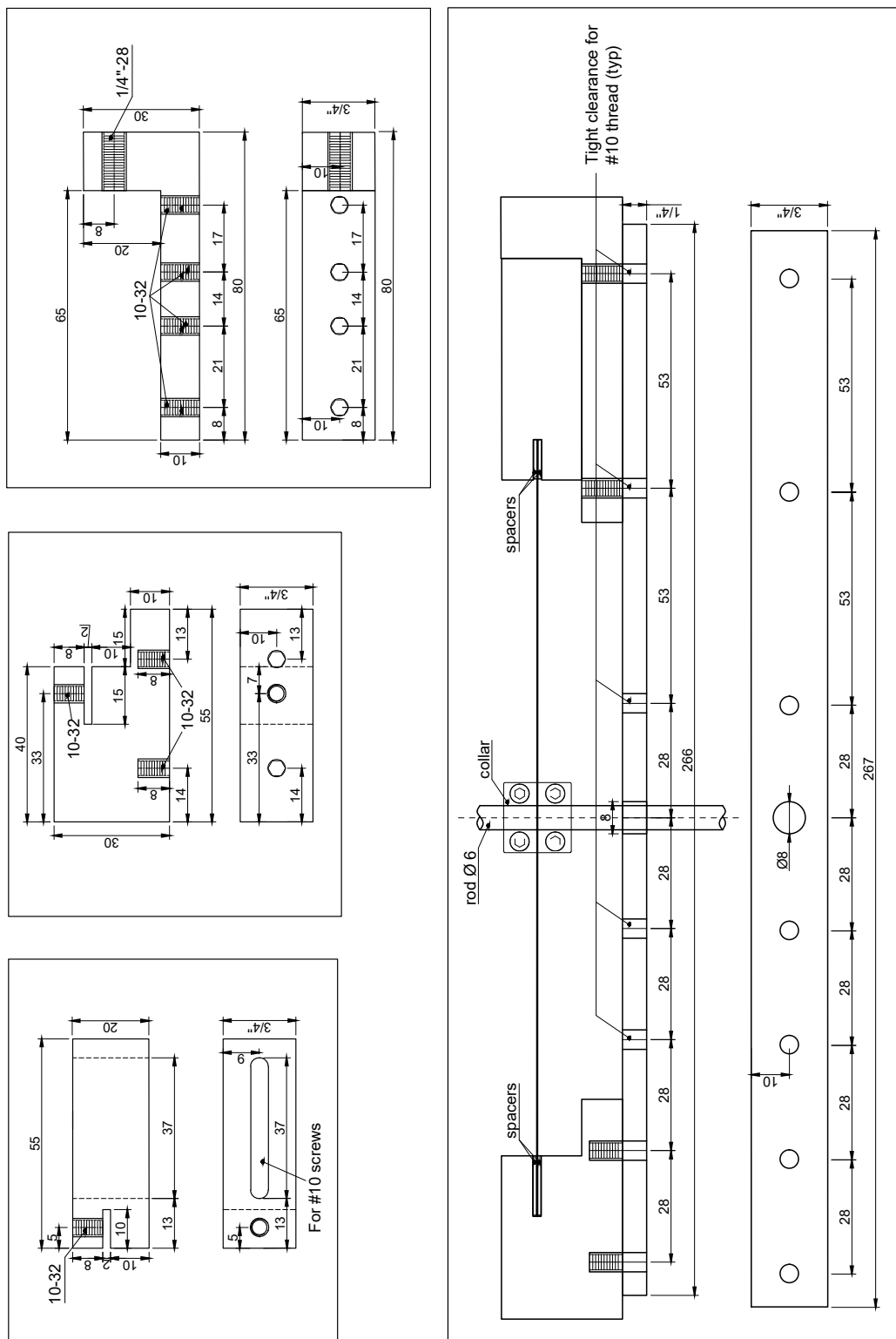


Figure 5.11: Technical drawing of the support.

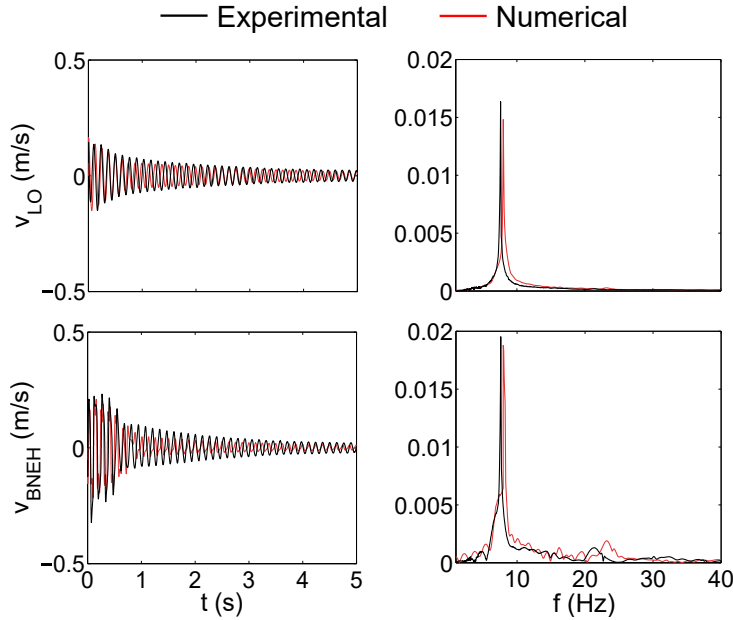


Figure 5.12: Fitting of experimental response time-histories and corresponding FFTs. Black line: experiment, red line: numerical model

may become difficult to determine when the tangent to the equilibrium path becomes horizontal (i.e. at the limit point). There are different approaches to solve such problems, as switching to dynamic analysis or using displacement controlled static analysis. Alternatively, static equilibrium states during the unstable phase of the response can be found by using the modified Riks method (or, arch-length method), which is implemented in Abaqus. The basic Riks algorithm is essentially Newton's method with load magnitude as an additional unknown to solve simultaneously for loads and displacements (the solution is viewed as the discovery of a single equilibrium path in a space defined by the nodal variables and the loading parameter), thus, can provide solutions even in cases of complex and unstable response. The displacement of the midspan of the beam is plotted as a function of the reaction force at that point in Figure 5.15). This plot shows the negative force that develops during snap-through. A series of deformed configurations are also depicted in Figure 5.16. The negative linear and cubic coefficients of

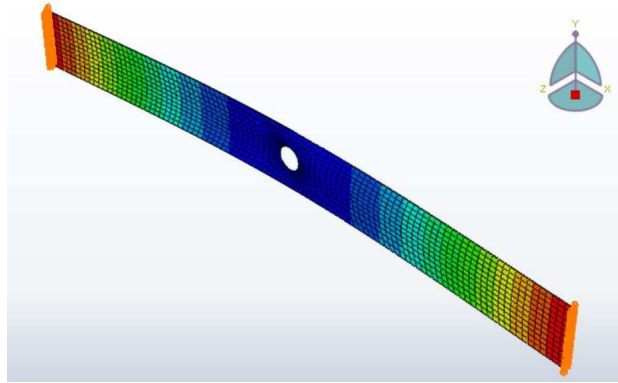


Figure 5.13: Configuration of the beam at the end of the first step (i.e. second step starting configuration).

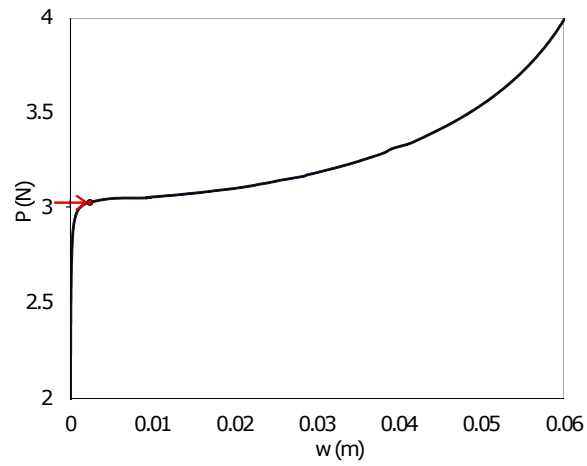


Figure 5.14: Bifurcation curve for the beam with imperfection.

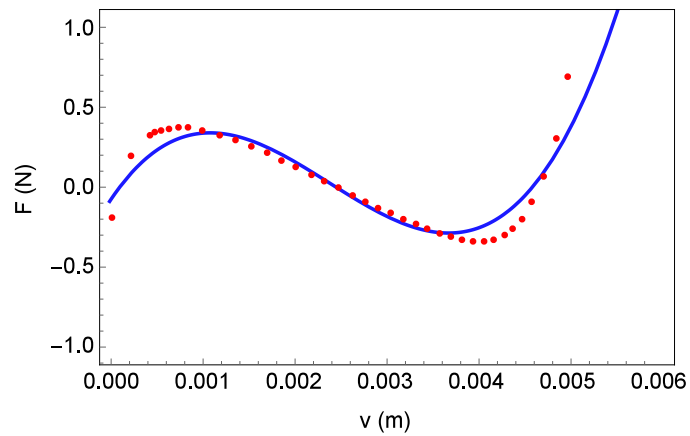
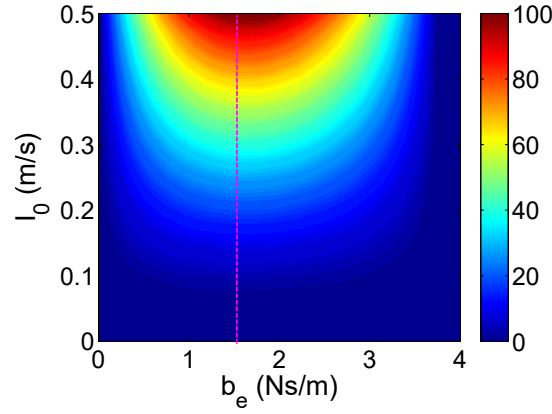


Figure 5.15: Polynomial fitting (blue line) of the force-displacement curve (red dotted line) of the buckled beam (Abaqus)



Figure 5.16: Series of deformed shapes during snap-through

Figure 5.17: Total energy harvested as a function of the electro-mechanically induced damping, with $k_e = 11 \text{ T m}$ and $R_c = 32.1 \Omega$.

the restoring force are detected by fitting the load-displacement curve. For the beam with aforesaid dimensions and post-buckling displacement at the midspan of 2.5 mm, the identified cubic coefficient k_2 matches with the one experimentally identified; the linear stiffness coefficient k_3 is found to be slightly smaller than the one predicted with the FEA. In fact, the FEA has some limitations, including the strong dependence of the results on the initial imperfection assigned. The final values are reported in Table 5.1.

The identification of the coil parameters is provided in [68]. Keeping fixed the transduction factor and once measured the coil resistance R_c , the load resistance has been chosen in order to maximize the power output (cfr. Figure 5.17). The inherent

Description, symbol	Value
LO mass, m_1	7.81 kg
LO natural frequency, f_1	8.2464 Hz
LO linear stiffness, k_1	2.097×10^4 N/m
LO damping factor, ζ	0.25%
LO linear viscous damping, b_1	2.05 Ns/m
BNEH mass, m_2	0.2845 kg
BNEH cubic stiffness, k_2	1.29×10^8 N/m ³
BNEH linear stiffness, k_3	-819 N/m
BNEH linear viscous damping, b_2	5 Ns/m

Table 5.1: Mechanical parameters

Description, symbol	Value
Load resistance, R_L	47 Ω
Coil resistance, R_c	32.1 Ω
Transduction factor, k_e	11 T m
Electromechanical damping coefficient, b_e	1.53 Ns/m

Table 5.2: Electromagnetic parameters

damping coefficient b_2 is found to be rather high and only partly controllable due to physical and experimental limitations. It is important to highlight that the BNEH damping plays a crucial role in the dynamics of the coupled system, thus on the energy harvesting performance. As expected, very weak damping in the coupling is desirable in order to optimize the performance of the harvester. The causes of high damping in the coupling may include a non perfect alignment between ball bearings and shaft, friction at the bearing-rod interface, damping of the lubrication film within the contact zone between the rolling elements and the shaft.

In conclusion, the measured and experimentally identified parameters for the physical apparatus are summarized in Tables 5.1 and 5.2.

5.3 Results

A series of experimental trials were conducted over a wide range of excitation magnitudes, corresponding to a range of initial velocities spanning (0.05 – 0.4) m/s, and, for the repeated impulses case, over various frequencies of application of the

pulse train. The configuration of the system is such that the midspan deflection of the buckled beam is 2.5 mm.

System (3.52) was solved numerically and compared to the experimental results. To explore the case of single impulsive forcing excitation, the numerical simulation has been carried out using the forcing data of the experimental trials for single impulse and checked the validity of the Dirac forcing assumption, according to which an impulsive force $F(t) = X\delta(t)$, with $\delta(t)$ the Dirac delta function and X the magnitude of the impulse, applied to the system at rest at $t = 0^-$, can be equivalently expressed as an initial velocity X/m_1 and no external forcing. Denoting by $I_0 = X/m_1$ the initial velocity of the primary system directly following the applied impulse, the following initial conditions can be set:

$$y_1(0^+) = 0, \quad \dot{y}_1(0^+) = I_0, \quad z(0^+) = 0, \quad \dot{z}(0^+) = -I_0, \quad Q(0^+) = 0 \quad (5.1)$$

letting $F(t) = 0$. Multiple impacts are, instead, modelled as in 3.59.

5.3.1 Single impulse scenario

For the single impulse forcing scenario, the energy harvesting capacity of the investigated system is represented in the graph of Figure 5.18(a), where the total amount of energy harvested E_h is plotted as a function of the magnitude of the impulse imparted to the primary mass up to the time instant when the system dynamics completely damps out. As shown by the solid line in the same plot, the numerical results are in good agreement with the experimental measurements, suggesting that the modeling captures the main features of the dynamics of the system. Up to ≈ 80 mJ can be experimentally extracted over a duration of ≈ 2 s in the range of impulse magnitudes studied, providing an average output power of ≈ 40 mW and ≈ 40 mA for the selected load.

Damping in the coupling is the most uncertain parameter of the experimental fixture. Although the main source of damping is related to squeezing the oil film

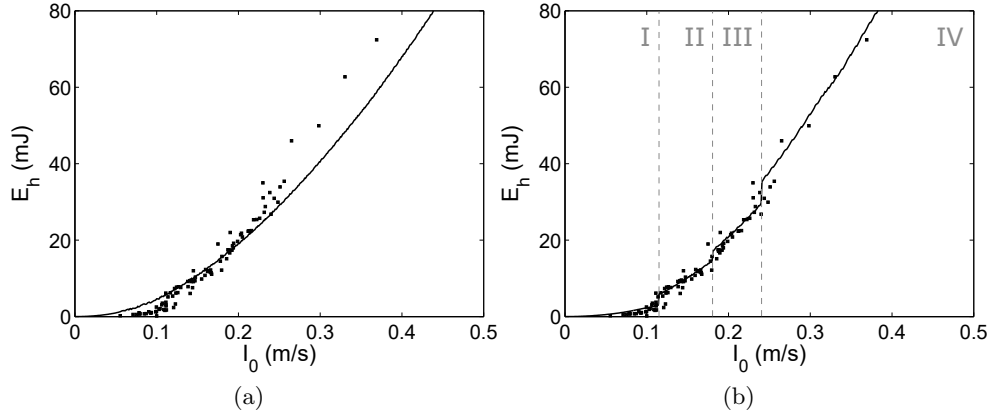


Figure 5.18: Total energy harvested by single impulse as a function of the input energy magnitude (solid line: numerical simulation, markers: experiments), a) modeling with b_2 as from Table 5.1; b) b_2 varying according to the energy level: I) $b_2 = 11$ Ns/m for $I_0 < 0.12$ m/s, II) $b_2 = 5.4$ Ns/m for $I_0 \in [0.12, 0.18)$ m/s, III) $b_2 = 4.4$ Ns/m for $I_0 \in [0.18, 0.24)$ m/s, IV) $b_2 = 3.4$ Ns/m for $I_0 > 0.24$ m/s

at the lubricated ball-shaft contacts, which provides a linear damping, additional sources of damping may be present, as, for example, a misalignment effect, which may cause the film thickness to decrease and some friction to arise. The distribution of the points in the graph 5.18(a) suggests the possibility to refine the choice of the parameters of the numerical model according to the initial energy level. In fact, four regions of different ranges of input energy can be distinguished- very low (I), low (II), intermediate (III) and high (IV) energy regions- to each of which can be associated a different damping factor, as shown in Figure 5.18(b).

The observed effective passive energy transfer mechanism from the LO to the nonlinear attachment observed is given by cross-well oscillations of the BNEH, with high frequency dynamic instability triggered by sufficiently high input energy, occurring at the first cycles of oscillation following the impact for a duration that depends on the energy level initially imparted to the LO. However, as the instantaneous energy in the system gradually reduces due to damping dissipation, the dynamic regime changes to in-well oscillations and no significant energy is harvested. Only acceleration and velocities are accounted for the comparison of the experimental results with the numerical model, the reason being that the high-pass filter applied to the displacement time history, derived from numerical integration

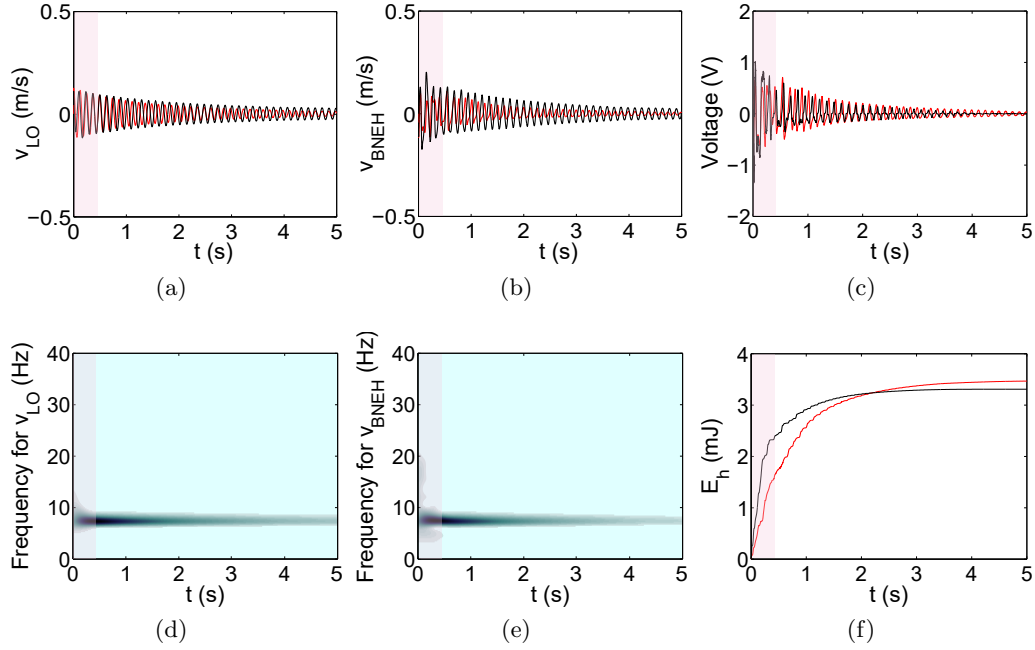


Figure 5.19: Dynamics of the two-DOF system for the very low input energy level ($I_0 = 0.10$ m/s): time histories of the LO velocity (a) and BNEH relative velocity (b); (d) and (e) corresponding wavelet transform spectra; (c) measured voltage; (f) total energy harvested by the BNEH. — experimental trial, — corresponding numerical simulation.

of the velocity signal, distorts the output, preventing the depiction of transition between the two potential wells (arising due to bistability) in the early, highly energetic regime of the response. This issue arises because of the low frequency associated with such a transition.

The typical dynamics exploited for energy harvesting is shown in Figures 5.19–5.20 and 5.21, for three different energy levels.

Figure 5.22 shows the comparison of the energy harvesting capability of the BNEH under exam with its monostable counterpart, achieved with the straight (unbuckled) configuration of the thin beam, and with its linear counterpart ($k_2 = 0$) with optimized positive linear stiffness $k_3 > 0$. Also, bistable and cubic harvester systems with optimal stiffness and damping parameters are shown in the same graph. The nonlinear stiffness coefficients for the straight beam were computed analytically and verified through a nonlinear static analysis of the FEM of the beam,

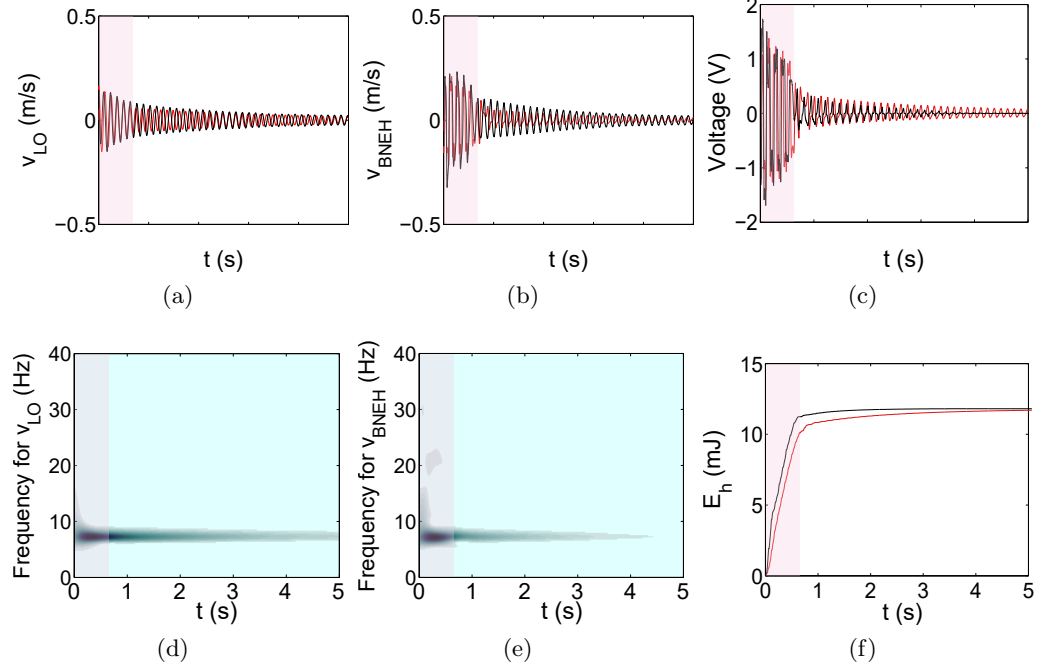


Figure 5.20: Dynamics of the two-DOF system for the low input energy level ($I_0 = 0.14 \text{ m/s}$): time histories of the LO velocity (a) and BNEH relative velocity (b); (d) and (e) corresponding wavelet transform spectra; (c) measured voltage; (f) total energy harvested by the BNEH. — experimental trial, — corresponding numerical simulation.

similarly to that described in Section 5.2 for the buckled beam. The computed stiffness coefficients, complemented with further considerations, are provided in Appendix A.

Due to the small thickness of the beam cross-section and the absence of any pretension, the (positive) linear component in the coupling stiffness is very small ($k_3 = 90.65 \text{ N/m}$) compared to the cubic component; thus, it does not affect significantly the strongly nonlinear dynamical response of the system, which, in essence, behaves as purely cubic. The performance comparison demonstrates that exploiting the bistability of the post-buckling beam leads to a significant enhancement of the energy harvesting capability with respect to its monostable counterpart. It is known, in fact, that a bistable device can overcome the deficiency of a cubic strongly nonlinear or essentially cubic harvesting system at low magnitude excitations.

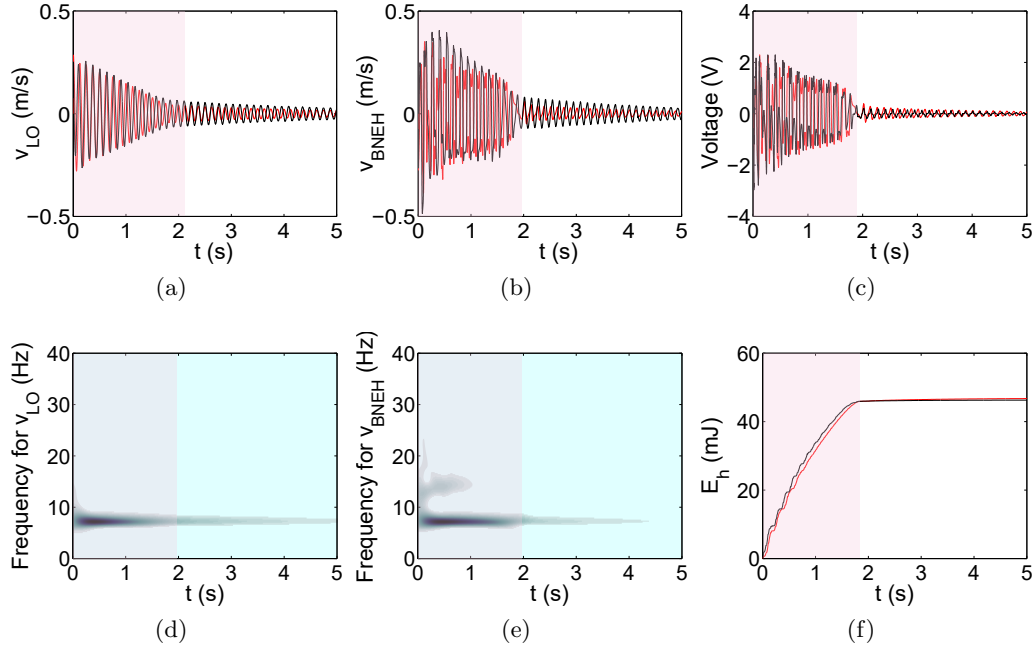


Figure 5.21: Dynamics of the two-DOF system for the high input energy level ($I_0 = 0.25$ m/s): time histories of the LO velocity (a) and BNEH relative velocity (b); (d) and (e) corresponding wavelet transform spectra; (c) measured voltage; (f) total energy harvested by the BNEH. — experimental trial, — corresponding numerical simulation.

The linear energy harvester, if optimized in terms of optimal stiffness, performs similarly to the BNEH, although the main disadvantage of this type of coupling is observed in case of periodic or multi-impact excitations, for which it works optimally only when the natural frequency of the system is tuned to the excitation frequency. Operating far from the fundamental frequency causes its energy harvesting performance to decay. Moreover, energy harvesting performance of the (theoretical) optimized system is depicted in Figure 5.22 to highlight the appreciable gain expected through an improvement of the physical apparatus. At last, it can be seen the increase of energy harvested by the optimal BNEH, for low excitation levels, even if compared to the optimal cubic EH.

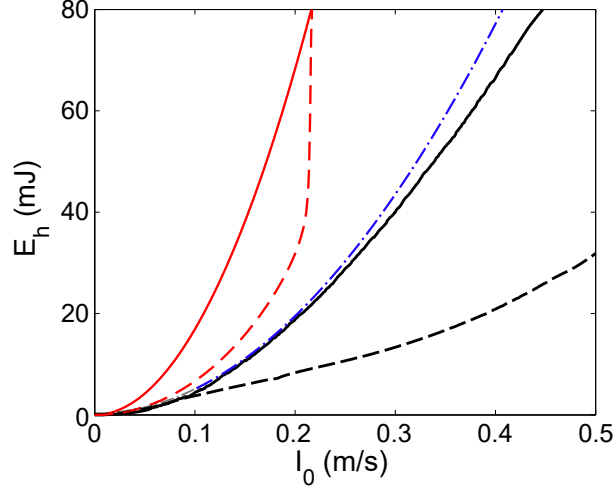


Figure 5.22: Comparison of the total energy harvested by single impulse by different types of Energy Harvesters (EH): — current bistable EH, - - - current monostable EH, — optimal bistable EH, - - - optimal cubic EH, - · - linear EH with optimal linear stiffness coefficient.

5.3.2 Repeated impulses scenario

For the second excitation scenario considered, which contemplates periodically repeated impacts, data have been collected, for various forcing magnitudes, by varying the inter-arrival time of the pulses t_p . As discussed in Section 3.1, the interval between the application of two consecutive pulses t_p is here normalized by the LO fundamental period T_1 , so that the impulse period is defined as $\mu_T = t_p/T_1$, with $T_1 = 0.1213$ s. For the experimental trials, μ_T spans the range $[2.5 - 15]$, where the lower bound is related to physical limitations encountered while attempting to excite the system at a higher frequency, and the upper bound is due to the fact that at lower forcing frequencies the impacts can be regarded as isolated, since the system goes to rest before that the next pulse is applied. Performance contour plots for the system (3.52) are developed numerically (Dirac forcing) using energy harvesting measure (3.61). The contour plot of Figure 5.23 shows the typical numerical finding [94, 69] of discrete “ribs” of higher performance occurring at discrete ranges of impulse periods, nearly multiples of the primary system fundamental period, indicating strong dependence upon the dynamic state of the primary system when excited. On the high performance ribs energy peaks

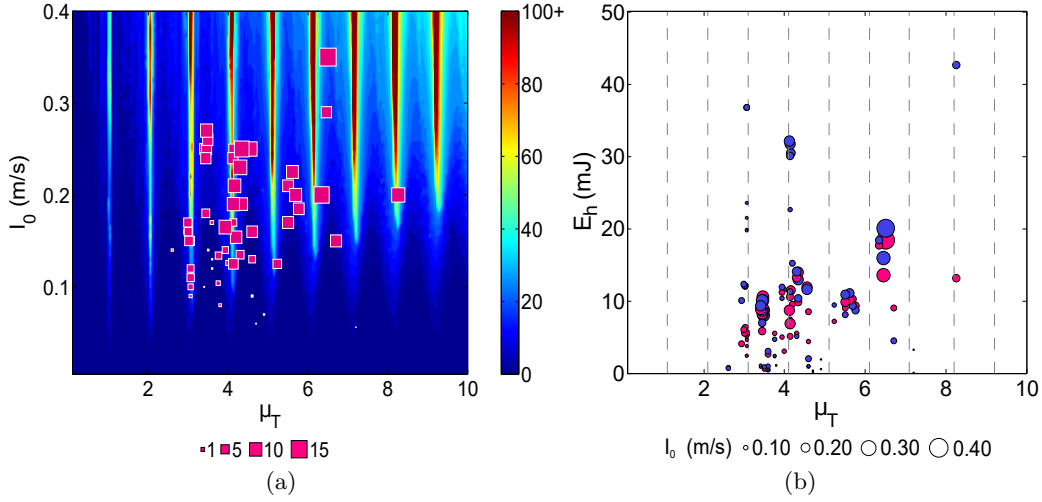


Figure 5.23: Total energy harvested after 15 impulses as a function of the input magnitude and period of application of the pulse train: a) contour plot: numerical model, markers: experiments; b) red markers: numerical simulation, blue markers: experimental trials (the vertical dashed lines recall the position of the high-performance ribs).

of 280 mJ are attained. The inspection of the system response time histories and corresponding wavelet spectra confirms a change of the dynamics in those regions, where a high-frequency dynamic instability in the harvester response can be observed, as shown in the plots of Figure B.1 and discussed in Appendix B. By the superposition of the discrete experimental points on the plots of Figure 5.23, it becomes apparent that this promising result is not replicated experimentally. The numerical model is able to recover the whole dynamics of the experimental fixture, despite the strong approximation of it (1 d-o-f), when outside the high-performance ribs (cfr., for example, Figures B.4 and B.5), but differs for input periods that approach multiples of the primary system fundamental period. Unlike the numerical simulation, in fact, the primary system response grows to a bounded size rather than continually increasing for the whole observed response duration (cfr. Figures B.3 and B.1).

In investigating the causes of the loss of adherence to the real case, the first aspect to consider is that, generally, the forces applied to the linear oscillator are not of the same magnitude and are only nearly periodic. The instant at which the stinger

of the shaker strikes the linear frame and the magnitude of the force depend on the ratio between the period of the shaker excitation and the eigenperiod of the linear oscillator. To explore the effect of non perfect periodicity and of the non-uniform amplitude of excitation, and to exclude this aspect from the possible reasons of numerical and experimental mismatch, pseudo-experimental tests have been carried out, by inputting the real forcing signal into the numerical model; these confirmed that those aspects do not appreciably affect the numerical outcome as seen, for example, in Figures B.1, B.2 and B.3. The discrepancy so far discussed can be sought either in the lack of higher modes in the current single-dof numerical model of the beam, or in the difficulty of tuning the frequency of the impulses when the dynamics is considered in the neighborhood of the frequency ranges of interest. The one-dof modeling of the harvester, in fact, does not account for the possible nonlinear scattering of energy from the fundamental mode to higher modes of the beam – in other words, the redistribution of the energy in the modal space when impulsive energy is scattered to higher frequencies. This energy scattering would reduce the overall amplitude of the transient response, with the final effect of decreasing the amount of energy harvested. To this aim, a more accurate multi-modal model is being set up. On the other end, further experimental tests may still confirm the presence of the narrow high-performance regions.

The inability of the single-dof model to capture accurately energy harvesting by repetitive impulses in the high-performance regime can also be attributed to phasing issues. That is, in the experimental beam many modes are excited during the application of each impulse, and the relative phase between the input force and a particular mode plays a critical role in the energy transferred from the shaker to that mode by the applied impulse. Hence, certain beam modes are excited more efficiently than others, depending on their relative phase with the excitation at the time instant of application of each impulse. The numerical single-dof model clearly cannot capture this effect since it takes into account only one (the fundamental) beam mode and ignores the others. For the case of a single impulse phasing is not

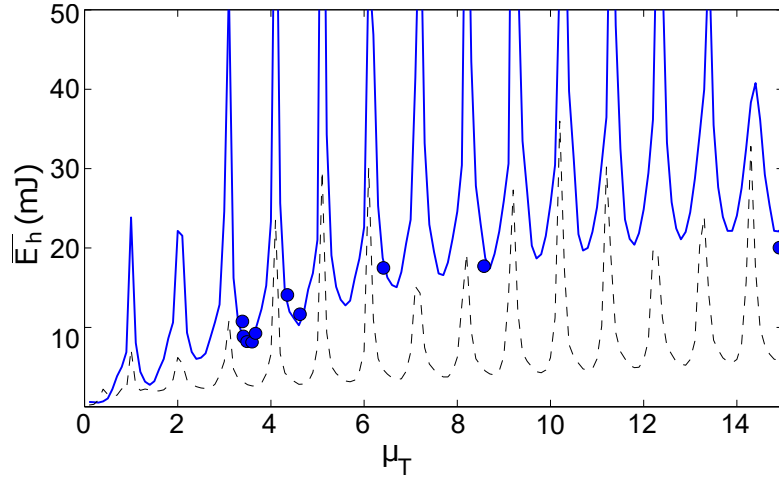


Figure 5.24: Numerical mean energy harvested over 100 impulses, $I_0 = 0.25$ m/s: — bistable EH, --- monostable EH, • experimental trials.

important and there is good agreement between the model and the experimental results. In the high-performance energy harvesting regimes the issue of how much energy is absorbed by the beam modes from the applied impulses is critical, and the single-dof model is not suitable anymore.

However, up to ≈ 20 mJ have been experimentally harvested, which results in an average harvested power of 20 mW within the range of energy level considered. Having proved that the numerical model predicts with reasonable accuracy the experimental results, except for the case discussed above, it has been used to prove the enhancement in energy harvesting capacity of the bistable attachment with respect to its monostable counterpart. The comparison reveals a gain of above 4 times of total energy harvested outside the high-performance ribs, as illustrated in the graph of Figure 5.24, reporting the mean energy harvested over 100 pulses for the energy level $I_0 = 0.25$ m/s.

Chapter 6

Conclusion

The main results obtained in the present research work and possible future developments are summarized in this concluding chapter.

6.1 Research summary and concluding remarks

The research documented in this work presents a computational and experimental study of the impulsive dynamics of a electromagnetic bistable energy harvesting system (BNEH) coupled to a directly excited, weakly damped linear primary system (LO). The coupling is realized by means of a cubic stiffness nonlinearity and negative linear stiffness, that makes the harvesting system to be bistable. The strong nonlinearity results from the transverse displacement of a linearly elastic beam (nonlinear effects appear due to midplane stretching of the elastic beam), whereas the bistability arises from the post-buckling configuration of the beam itself.

A parametric analysis is performed numerically in order to study the effect of sensitive parameters on the energy harvesting capability of the system. Special attention is devoted to the case of low energy level impulses, below the inefficiency threshold characterizing the purely cubic NEH. Mass ratio, negative stiffness and

damping in the coupling, which is provided by both the mechanical inherent damping of the BNEH and the electromechanical coupling, are found to be the key parameters governing the energy harvesting performance. Under a single impulse, by decreasing the energy level, three different mechanisms are exploited to attain a fast energy capture and harvesting: periodic cross-well oscillations, a chaotic regime of aperiodic cross- and in-well oscillations, and nonlinear beats in a fully in-well oscillation. By comparing the energy harvesting capabilities of the system with and without the negative linear coupling stiffness, a significant enhancement in terms of both energy harvesting efficiency and total energy harvested due to the addition of the bistability is observed. For the considered set of parameters, the nonlinear device is found to be able to absorb and harvest above 40 mJ at the highest energy level, 90% of which is harvested in the first 0.4 seconds, whereas energy of the order of mJ can still be harvested at very low input energy regimes. The numerical study conducted on the same system subjected to periodically repeated impulses reveals that greater robustness is achieved by the bistable configuration, resulting from a lesser dependence upon the inter-arrival time of the impulses when compared to the monostable configuration, for which narrow, high-performance ranges of impulse period exist. Energy harvesting capability greater than 400 mJ per applied impulse is theoretically achievable for the high-energy inputs and for optimal impulse periods.

Also the scenario of stochastic impulsive excitation has been explored and it revealed that a random distribution of the impulse amplitude provides for a considerable gain of energy harvested by the bistable device compared to the monostable case, in the low energy regime and, also, for an enhancement of the energy harvesting capability if compared to the periodic impulses scenario, regardless the particular configuration (bi- or mono-stable) of the coupling. If random interarrival time of the impulses are considered instead, a deterioration of the harvester performance and less robustness and reliability can be observed, although the bistable system still performs better than the cubic one.

It followed the experimental study of the integrated system. The experimental fixture and set-up is described. The mechanical coupling between the hosting system and the nonlinear attachment is realized by means of a steel beam axially compressed until the post-buckling configuration is reached, in order to provide a negative linear stiffness component to the coupling. The apparatus design was based on the previous numerical study of the system, which led to the detection of optimal parameters for best energy harvesting performance, although the physical system is still not optimized, due to physical/operational limitations.

Under isolated impulse scenario, the snap-through instability of the buckled beam, with high-frequency transient resonance captures, enables efficient energy harvesting during the first cycles of motion: the nonlinear device is found to be able to absorb and harvest up to 80 mJ of energy, with average power of 40 mW for the excitation level range considered (0.05 - 0.45) m/s. Such a behaviour is confirmed by the numerical model. The comparison with the monostable configuration of the same system, that is a cubic nonlinear configuration with negligible linear stiffness component, reveals the advantage offered by the bistable device in harvesting energy at the low excitation levels considered. On the other hand, an improvement of the physical apparatus towards the optimization would lead to a considerable gain in term of energy harvesting performance.

Under periodically repeated pulses, the engagement in high-frequency dynamic instability allows the bistable attachment to harvest tens of millijoule, attaining up to 40 mW of mean power experimentally extracted in the energy level range considered. On the other hand, promising numerical findings report a magnification of the energy harvesting performance, achievable by virtue of sustained high-frequency resonance captures occurring for periods of the pulse train multiple of the LO fundamental period. Energy peaks of 280 mJ are attained on the high-performance ribs numerically obtained. However, the numerical model agrees with the physical system only when outside the higher-performance ribs. It differs, in fact, for input periods that approach multiples of the LO fundamental period.

6.2 Novel contributions

- Unlike the case of vibration control, where the linear (tuned mass damper, TMD) or nonlinear (the so-called nonlinear energy sink, NES) device which is entrusted with the task of mitigation is generally studied in coupling with the host structure, it is common practice in the energy harvesting field to investigate the behaviour of the auxiliary device by itself, testing it under base excitation. In the first case, of course, the reason relies in the necessity of monitoring the effect of adding the auxiliary mass on the motion of the primary system, in order to establish the efficiency in reducing/controlling the vibration of the main structure. In the second case, however, the coupling of the energy harvesting device to the main system is all but irrelevant: in fact, the external excitation is, more realistically, filtered by the primary system and interesting dynamics can arise depending on the nonlinear characteristics of the coupling. Hence, coupling the energy harvesting system to a primary, hosting, system represents the main novelty of this work, allowing the analysis of the dynamic interaction and energy exchange between the two sub-systems. This approach turns out to be more realistic, howbeit, it increases the complexity of the mathematical problem, because of the addition of one degree of freedom to the global system.
- The system has been investigated contemplating typically non-stationary response regimes resulting from single or periodically and randomly repeated impulsive excitation, contrary to the common approach that consists of applying typically a harmonic or, in some cases, random, base excitation to the (one-degree-of-freedom modeled) harvester.
- The resort to the particular coupling, which adds bistability to the more traditional cubic one, was previously studied only for vibration suppression purpose. Its application to the energy harvesting represents a point of novelty, that leads to the increase of the dimension of the problem, since the

mathematical model contains the equation that describes the circuit part and, in particular, governs the electromagnetic interaction.

- The experimental realization of the combined physical system, aiming to explore experimentally its energy harvesting performance, required the optimization of the electromagnetic components, the design of the supports and connection systems between the two masses, the identification of the mechanical and electro-mechanical parameters and detection of the optimal procedures for the correct execution of the experimental tests.
- Another original contribution consisted in the design and realization of the element responsible for the desired nonlinearity and bistability and its integration in the global system. These steps presupposed the evaluation of reasonable and accessible solutions, then required the modeling of the chosen solution (the post-buckling beam) for the characterization of the mechanical parameters of the bistable element.

6.3 Future research

Since the numerical findings, for the case of repeated impulses, have been only partly confirmed experimentally, ongoing research activity is aiming to explore the cause of the mismatch between experimental findings and numerical computation. Future work will seek to comprehend whether further experimental trials will succeed in achieving it or interaction of higher modes not accounted in the numerical model prevents it to physically realise.

Experimental tests under stochastic impulsive excitation are, also, intended to be performed in order to assess the efficacy of the proposed energy harvesting device over a broad variety of excitations, including the more realistic scenario of random pulse-like vibrations. The optimal experimental apparatus is also intended to be realized, to maximize energy harvesting performance.

Furthermore, having ascertained the benefit produced by the energy harvesting

device on the mitigation of the primary system oscillations, future research activity is intended to investigate the double role of vibration suppression and energy harvesting for some relevant cases of engineering interest, as for slender pedestrian bridges, which easily violate the comfort criterion because of the excessive oscillations (either in the vertical or lateral directions) caused by the vicinity of their natural frequencies to that of the dynamic loads typical of human activity. One of the main features of the dynamic loading of pedestrian is, in fact, its low intensity. Applied to very stiff and massive structures, this load could hardly make them vibrate significantly. However, aesthetic, technical and technological developments lead to ever more slender and flexible structures, which, as a consequence, more frequently suffer excessive vibration problem.

Appendix A

Static analysis of the straight beam

The characterisation of the mechanical parameters of the straight beam (with no prestress) is here addressed, being necessary in order to establish a comparison between the energy harvesting capability of the harvester with and without the buckled configuration of the beam.

The effective structural stiffness of the clamped-clamped (linear elastic) straight beam supporting a concentrated load at the midspan, which is the critical point, is $K_{st} = 192EJ/L^3 = 90.45 \text{ N/m}$. This is confirmed by the numerical evaluation by means of modal analysis. The computed mode shapes has been normalized relative to the maximum displacement. If the single-mode Galerkin discretization method is used, the linear stiffness coefficient k_3 is given by the expression in (3.33), with $P = 0$:

$$K_{l,m} \approx \tilde{k}_1 = 91.10 \text{ N/m}$$

The linear natural frequency of the beam is $f_1 = 38.86 \text{ Hz}$. $K_{l,m}$ can be refined using a multi-mode discretization. The static stiffness can be expressed as the inverse of the maximum displacement induced by a unit force. If the static

equilibrium is written referred to the modal coordinates q_i , i.e. $[\tilde{K}]\{\tilde{q}\} = \{\tilde{p}\}$, with $[\tilde{K}]$ the modal stiffness matrix and $\{\tilde{p}\}$ the generalized load vector, it is $\tilde{k}_i q_i = \tilde{p}_i = p_i \phi_i(L/2)$. For $p_i = 1$, $q_i = \phi_i(L/2)/\tilde{k}_i$. The structural response at the critical point and in the load direction is $w(L/2) = \sum_{i=1}^n \phi_i(L/2) q_i$, thus $1/K_{l,m} = w(L/2) = \sum_{i=1}^n \phi_i(L/2) \phi_i(L/2)/\tilde{k}_i = \sum_{i=1}^n \phi_i(L/2)^2/\tilde{k}_i$, thus

$$\frac{1}{K_{st}} \approx \sum_{i=1}^n \frac{\phi_i(L/2)^2}{\tilde{k}_i} \quad (\text{A.1})$$

Equation (A.1) provides the relationship between the static stiffness and the modal stiffness of a structure. The symbol of approximation is due to the fact that the sum is truncated to a finite number of modes. $K_{l,m}$ calculated including 5 modes is equal to 90.65 N/m, which is slightly greater than K_{st} . In fact,

$$\frac{1}{K_{st}} > \frac{\phi_1(L/2)^2}{\tilde{k}_1} + \frac{\phi_3(L/2)^2}{\tilde{k}_3} + \frac{\phi_5(L/2)^2}{\tilde{k}_5}$$

since the series is truncated, thus

$$K_{st} < K_{l,m}$$

The ratio $K_{l,m}/K_{st}$ is 1.002, thus the modal and static stiffness are in very good agreement [95].

The coefficient of the cubic term of the equation (3.32) related to the first mode of vibration is:

$$K_{c,1} = 1.70 \times 10^9 \text{ N/m}^3$$

A nonlinear static analysis has been carried out for the steel beam subjected to a point load in the center of the beam. The force-displacement curve is obtained by assigning a ramped load and measuring the total deformation resulting at each load increment $\Delta F = 0.01N$. The best fit of the data points of the force-displacement curve within the range 0–0.001 mm of rise at the midspan, using a cubic polynomial

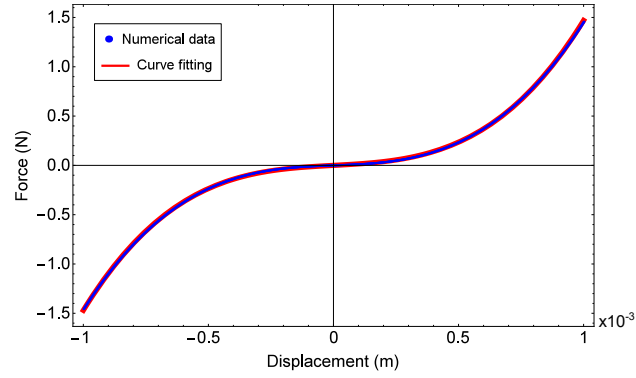


Figure A.1: Polynomial fitting of the force-displacement curve of the straight beam (red dotted line).

of the form $f(w) = k_{l,s}w + k_{c,s}w^3$, provides the following coefficients:

$$k_{l,s} = 92 \text{ N/m}, \quad k_{c,s} = 1.40 \times 10^9 \text{ N/m}^3$$

Appendix B

System response under repeated impacts

Case 1: upon one of the high-performance ribs

The system response found numerically operates in the 2:1 frequency regime, since a 2:1 resonance capture is maintained for the duration of the response between two consecutive impulses. The BNEH oscillates faster than the primary mass, which increases the energy harvesting capability of the system, and the response continually grows with each consecutive impulse. The transient response of the BNEH occurring for the first impulses initially engages in 3:1 or 2:1 resonance captures at the beginning of each applied impulse but it does not maintain this regime until the next impulse is applied. In fact, it transitions to 1:1 internal resonance capture, where energy is harvested at a slower rate (Figures B.2 and B.1). The experimental response grows slightly with each consecutive impulse and does not engage in any high-frequency dynamics (Figure B.3).

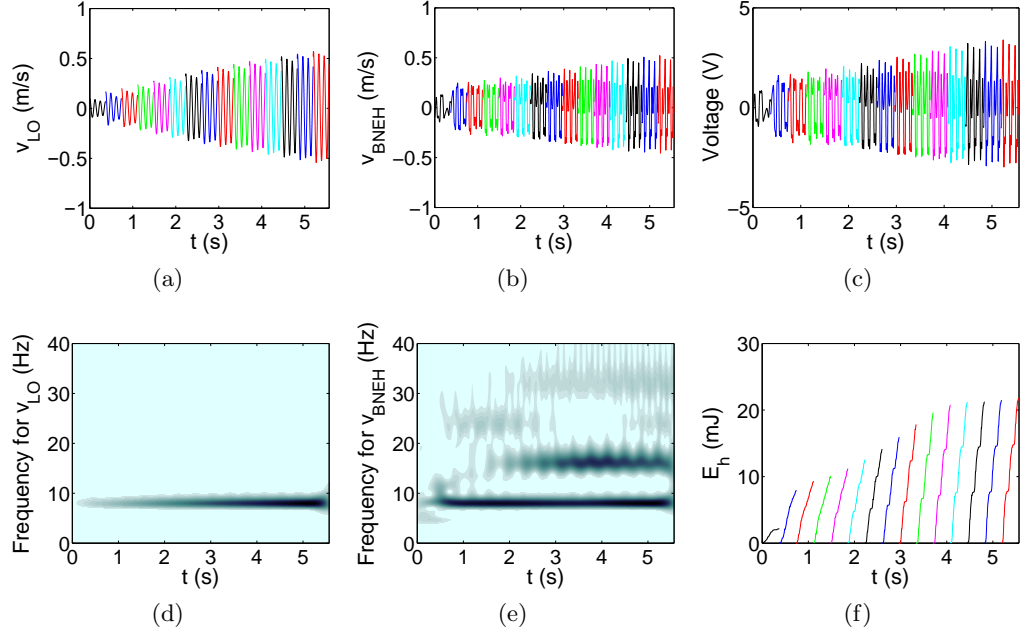


Figure B.1: Numerical system response for $I_0 = 0.1$ m/s and $\mu_T = 3.06$ (on a rib): velocity time history of LO (a) and BNEH (b); (d) and (e) corresponding wavelet transform spectra; (c) measured voltage; (f) total energy harvested by the BNEH

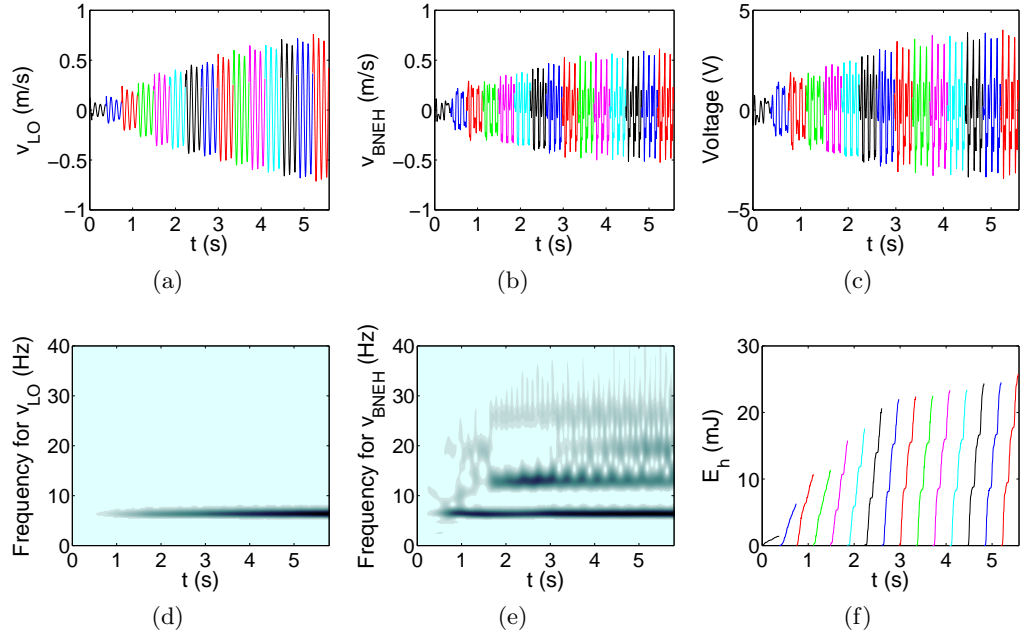


Figure B.2: Pseudo-experimental system response for $I_0 = 0.1$ m/s and $\mu_T = 3.06$ (on a rib): velocity time history of LO (a) and BNEH (b); (d) and (e) corresponding wavelet transform spectra; (c) measured voltage; (f) total energy harvested by the BNEH

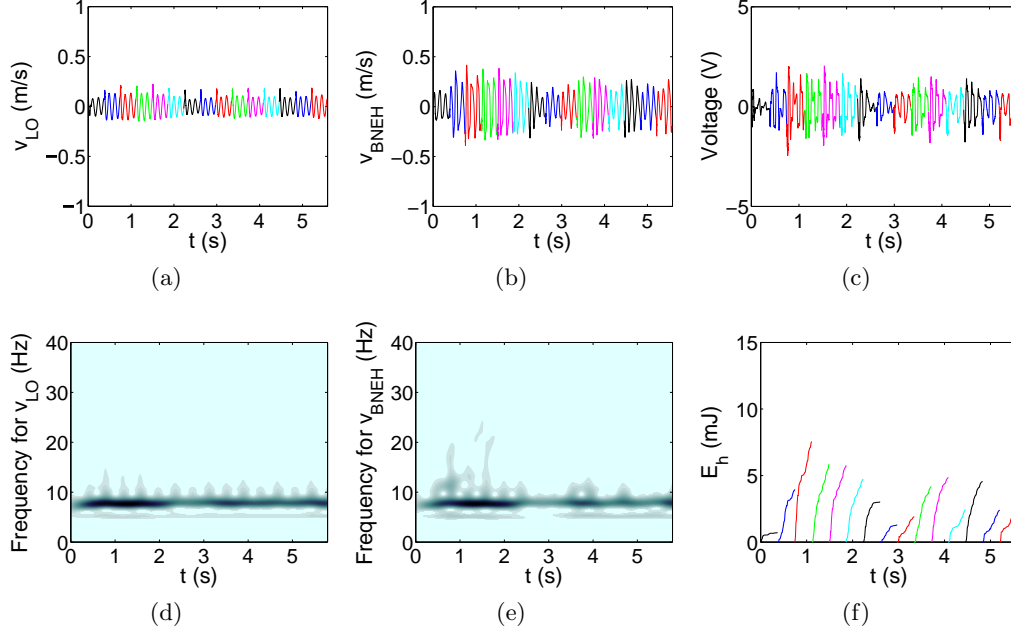


Figure B.3: Experimental system response for $I_0 = 0.1$ m/s and $\mu_T = 3.06$ (on a rib): velocity time history of LO (a) and BNEH (b); (d) and (e) corresponding wavelet transform spectra; (c) measured voltage; (f) total energy harvested by the BNEH

Case 2: outside the high-performance ribs

Both in numerical and experimental results, high frequency harmonics can be observed in the initial phase of the relative response for each impulse, in particular the transient response of the BNEH initially engages 2:1 and 3:1 internal resonance captures in the numerical simulation and 2:1 for the experimental trial, for each applied impulse. Frequency transitions above the primary system fundamental frequency correspond to oscillations of the BNEH faster than the primary system, which increases the energy harvesting capability of the system. As energy is dissipated and harvested by the system, the dynamics transitions to 1:1 internal resonance capture, where energy is still harvested, but at a slower rate. The initial energy input in the primary system is enough to excite the high-frequency dynamic instabilities, but not maintain them for long, meaning that no high-frequency sustained resonance capture are observed and the system operates in the 1:1 frequency regime (Figures B.4 and B.4).

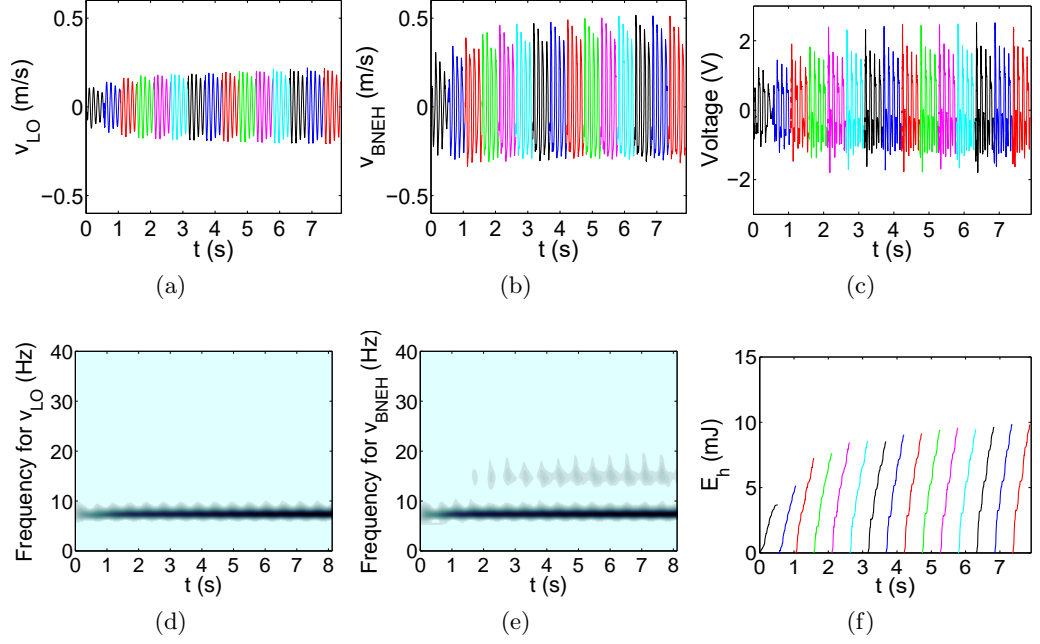


Figure B.4: Experimental system response for $I_0 = 0.19$ m/s and $\mu_T = 4.34$ (outside the ribs): velocity time history of LO (a) and BNEH (b); (d) and (e) corresponding wavelet transform spectra; (c) measured voltage; (f) total energy harvested by the BNEH

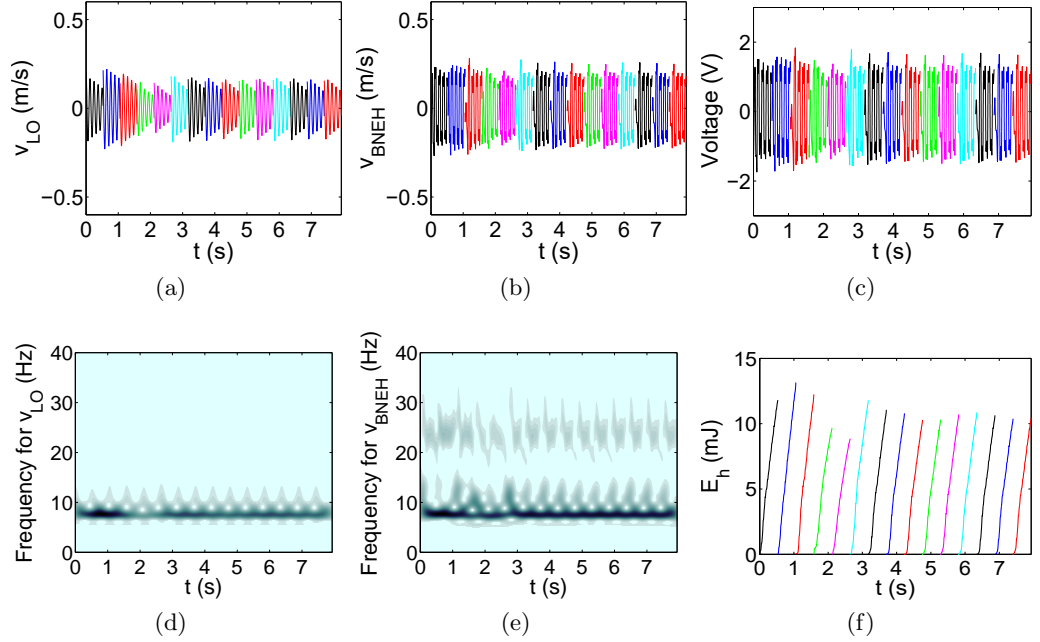


Figure B.5: Numerical system response for $I_0 = 0.19$ m/s and $\mu_T = 4.34$ (outside the ribs): velocity time history of LO (a) and BNEH (b); (d) and (e) corresponding wavelet transform spectra; (c) measured voltage; (f) total energy harvested by the BNEH

Bibliography

- [1] R.J.M. Vullers, R. van Schaijk, I. Doms, C. Van Hoof, and R. Mertens. Micropower energy harvesting. *Solid-State Electronics*, 53(7):684–693, 2009.
- [2] L. Gammaitoni, H. Vocca, I. Neri, F. Travasso, and F. Orfei. *Vibration energy harvesting: Linear and nonlinear oscillator approaches*. InTech, 2011.
- [3] B. Godderidge, S.R. Turnock, and M. Tan. Evaluation of a rapid method for the simulation of sloshing in rectangular and octagonal containers at intermediate filling levels. *Comput. Fluids*, 57:1–24, 2012.
- [4] D. Liu and B. Davis. Walking vibration response of high-frequency floors supporting sensitive equipment. *J. Struct. Eng.*, 141(8):04014199, 2014.
- [5] X. Zhang, X. Li, H. Hao, D. Wang, and Y. Li. A case study of interior low-frequency noise from box-shaped bridge girders induced by running trains: Its mechanism, prediction and countermeasures. *J. Sound Vib.*, 367:129–144, 2016.
- [6] L. Ma, D.J. Zhou, and W.S. Han. A study on the impact coefficient of traffic flows on a large cable-stayed bridge in a windy environment. *Shock and Vib.*, 2014, 2014.
- [7] T. Lin, J. Wang, and L. Zuo. Energy harvesting from rail track for transportation safety and monitoring. Technical report, Stony Brook, State University of New York, 2014.

-
- [8] B.P. Mann and N.D. Sims. Energy harvesting from the nonlinear oscillations of magnetic levitation. *J. Sound Vib.*, 319:515–530, 2009.
 - [9] S.C. Stanton, C.C. McGehee, and B.P. Mann. Reversible hysteresis for broadband magnetopiezoelectric energy harvesting. *Appl. Phys. Lett.*, 95(17):174103, 2009.
 - [10] R.L. Harne and K.W. Wang. A review of the recent research on vibration energy harvesting via bistable systems. *Smart Mater. Struct.*, 22(2):023001, 2013.
 - [11] W. Deng and Y. Wang. Systematic parameter study of a nonlinear electromagnetic energy harvester with matched magnetic orientation: Numerical simulation and experimental investigation. *Mech. Syst. Signal Process.*, 85:591–600, 2017.
 - [12] S. Lee, A.F. Vakakis, L.A. Bergman, D.M. McFarland, G. Kerschen, F. Nucera, S. Tsakirtzis, and P.N. Panagopoulos. Passive non-linear targeted energy transfer and its applications to vibration absorption: a review. *Proc. IMechE Part K: J. Multi-body Dynamics*, 222(2):77–134, 2008.
 - [13] A.F. Vakakis, O. Gendelman, L.A. Bergman, D.M. McFarland, G. Kerschen, and Y.S. Lee. *Passive Nonlinear Targeted Energy Transfer in Mechanical and Structural Systems: I and II*. Springer Verlag, 4^a edition, 2008.
 - [14] F. Romeo, G. Sigalov, L.A. Bergman, and A.F. Vakakis. Dynamics of a linear oscillator coupled to a bistable light attachment: Numerical study. *J. Comput. Nonlin. Dyn.*, 10:011007, 2015.
 - [15] I. Patel. Ceramic based intelligent piezoelectric energy harvesting device. In *Advances in Ceramics - Electric and Magnetic Ceramics, Bioceramics, Ceramics and Environment*, chapter 08. InTech, 2011.

- [16] W. Wang, J. Cao, C.R. Bowen, S. Zhou, and J. Lin. Optimum resistance analysis and experimental verification of nonlinear piezoelectric energy harvesting from human motions. *Energy*, 118:221–230, 2017.
- [17] K.H. Mak, S. McWilliam, and A.A. Popov. Piezoelectric energy harvesting for tyre pressure measurement applications. *Proceedings of the Institution of Mechanical Engineers, Part D: Journal of Automobile Engineering*, 227(6):842–852, 2013.
- [18] T. Seuaciuc-Osorio and M.F. Daqaq. Energy harvesting under excitations of time-varying frequency. *J. Sound Vib.*, 329:2497–2515, 2010.
- [19] D. Pan, B. Ma, and F. Dai. Experimental investigation of broadband energy harvesting of a bi-stable composite piezoelectric plate. *Smart Mater. Struct.*, 26:035045 (14pp), 2017.
- [20] D. Zhu. Vibration energy harvesting: Machinery vibration, human movement and flow induced vibration. In Dr. Yen Kheng Tan (Ed.), editor, *Sustainable Energy Harvesting Technologies- Past, Present and Future*. InTech, 2011.
- [21] S.D. Moss, O.R. Payne, G.A. Hart, and C. Ung. Scaling and power density metrics of electromagnetic vibration energy harvesting devices. *Smart Mater. Struct.*, 24(2):023001, 2015.
- [22] B.P. Mann and B.A. Owens. Investigations of a nonlinear energy harvester with a bistable potential well. *J. Sound Vib.*, 329:1215–1226, 2010.
- [23] T. Ma and H. Zhang. Enhancing mechanical energy harvesting with dynamics escaped from potential well. *Appl. Phys. Lett.*, 100(11):114107, 2012.
- [24] H.J. Jung, I.H. Kim, and J. Park. Experimental validation of energy harvesting device for civil engineering applications. In *Sensors and Smart Structures Technologies for Civil, Mechanical and Aerospace Systems in Proc. of SPIE*, volume 8345, pages 83451C–1, 2012.

- [25] T. Nagayama and B. F. Spencer Jr. Structural health monitoring using smart sensors. Technical report, Newmark Structural Engineering Laboratory Report Series, No. 001, 2007.
- [26] K. Gkoumas, F. Petrini, and F. Bontempi. Energy harvesting for the life-cycle of structures and infrastructures: State of art, recent trends and future developments. *in Life-Cycle and Sustainability of Civil Infrastructure Systems - Proceedings of the 3rd International Symposium on Life-Cycle Civil Engineering, IALCCE*, pages 2102–2109, 2012.
- [27] A. Moschitta and I. Neri. Power consumption assessment in wireless sensor networks. *ICT - Energy - Concepts Towards Zero - Power Information and Communication Technology, Dr. Giorgos Fagas (Ed.), InTech*, 2014.
- [28] O. Landsiedel, K. Wehrle, and S. Götz. Accurate prediction of power consumption in sensor networks. *in Proceedings of the Second IEEE Workshop on Embedded Networked Sensors (EmNetS-II)*, 2005.
- [29] L.A.F. Santos, M. de Oliveira Marques, and I.S. Bonatti. Power-aware model for wireless sensor nodes. 2008.
- [30] S. Chen, J. Yao, and Y. Wu. Analysis of the power consumption for wireless sensor network node based on zigbee. *International Workshop on Information and Electronics Engineering (IWIEE)*, 2012.
- [31] U.A. Perez. Low power wifi: A study on power consumption for internet of things. Master’s thesis, Universitat Politecnica de Catalunya (UPC) - BarcelonaTech, 2015.
- [32] G.A. Hassaan. Optimal design of a vibration absorber-harvester dynamic system. *Int. J. Res. Eng. Technol.*, 3(6):325–329, 2014.
- [33] N.S. Shenck and J.A. Paradiso. Energy scavenging with shoe-mounted piezoelectrics. *IEEE micro*, 21(3):30–42, 2001.

- [34] R. Guigon, J. Chaillout, T. Jager, and G. Despesse. Harvesting raindrop energy: experimental study. *Smart Mater. Struct.*, 17:015039 (6pp), 2008.
- [35] F. Viola, P. Romano, R. Miceli, and G. Acciari. Harvesting rainfall energy by means of piezoelectric transducer. In *Proceedings of International Conference on Clean Electrical Power*, 2013.
- [36] R. Amirtharajah and A.P. Chandrakasan. Self-powered signal processing using vibration-based power generation. *IEEE J. Solid-State Circuits*, 33(5):687–695, 1998.
- [37] M. El-Hami, P. Glynne-Jones, N.M. White, M. Hill, and E. and Brown A.D. and Ross J.N. Beeby, S. and James. Design and fabrication of a new vibration-based electromechanical power generator. *Sens. Actuators A Phys.*, 92(1):335–342, 2001.
- [38] S. Roundy, P.K. Wright, and J. Rabaey. A study of low level vibrations as a power source for wireless sensor nodes. *Comput. Commun.*, 26(11):1131–1144, 2003.
- [39] C.B. Williams and R.B. Yates. Analysis of a micro-electric generator for microsystems. *Sensors and Actuators A: Physical*, 52(1-3):8–11, 1996.
- [40] S. Roundy and Y. Zhang. Toward self-tuning adaptive vibration-based micro-generators. In *Smart Materials, Nano-, and Micro-Smart Systems*, pages 373–384. International Society for Optics and Photonics, 2005.
- [41] D. Zhu, M. J. Tudor, and S. P. Beeby. Strategies for increasing the operating frequency range of vibration energy harvesters: a review. *Meas. Sci. Technol.*, 21(2):022001, 2010.
- [42] L. Tang, Y. Yang, and C.K. Soh. Toward broadband vibration-based energy harvesting. *J. Intel. Mat. Syst. Str.*, 21:1867–97, 2010.

- [43] S.M. Shahruz. Design of mechanical band-pass filters for energy scavenging. *J. Sound Vib.*, 292:987–998, 2006.
- [44] R.S. Langley. A general mass law for broadband energy harvesting. *J. Sound Vib.*, 333(3):927–936, 2014.
- [45] Y. Hu, H. Xue, J. Yang, and Q. Jiang. Nonlinear behavior of a piezoelectric power harvester near resonance. *IEEE Trans. Ultrason., Ferroelect., Freq. Contr.*, 53(7):1387–1391, 2006.
- [46] D.A.W. Barton, S.G. Burrow, and L.R. Clare. Energy harvesting from vibrations with a nonlinear oscillator. *J. Vib. Acoust.*, 132(2):021009, 2010.
- [47] M.F. Daqaq, R. Masana, A. Erturk, and D.D. Quinn. On the role of nonlinearities in vibratory energy harvesting: a critical review and discussion. *Appl. Mech. Rev.*, 66(4):040801, 2014.
- [48] P. Li, S. Gao, H. Cai, and L. Wu. Theoretical analysis and experimental study for nonlinear hybrid piezoelectric and electromagnetic energy harvester. *Microsystem Technologies*, 22(4):727–739, 2016.
- [49] M.F. Daqaq. Response of uni-modal duffing-type harvesters to random forced excitations. *J. Sound Vib.*, 329(18):3621–3631, 2010.
- [50] P. Harris, C.R. Bowen, H.A. Kim, and G. Litak. Dynamics of a vibrational energy harvester with a bistable beam: voltage response identification by multiscale entropy and “0-1” test. *EPJ Plus*, 131(4):1–12, 2016.
- [51] D. Geiyer and J.L. Kauffman. Control between coexistent attractors for optimal performance of a bistable piezoelectric vibration energy harvester. In *SPIE Smart Structures/NDE*, pages 97990I–97990I. International Society for Optics and Photonics, 2016.
- [52] L. Ren, R. Chen, H. Xia, and X. Zhang. Energy harvesting performance of a broadband electromagnetic vibration energy harvester for powering industrial

- wireless sensor networks. In *SPIE Smart Structures/NDE*, pages 97993P–97993P. International Society for Optics and Photonics, 2016.
- [53] A. Erturk, J. Hoffmann, and D.J. Inman. A piezomagnetoelastic structure for broadband vibration energy harvesting. *Appl. Phys. Lett.*, 94(25):254102, 2009.
- [54] L. Gammaitoni, I. Neri, and H. Vocca. Nonlinear oscillators for vibration energy harvesting. *Appl. Phys. Lett.*, 94(16):164102, 2009.
- [55] F. Cottone, L. Gammaitoni, H. Vocca, M. Ferrari, and V. Ferrari. Piezoelectric buckled beams for random vibration energy harvesting. *Smart Mater. Struct.*, 21:035021 (11pp), 2012.
- [56] D. Zhu and S.P. Beeby. A coupled bistable structure for broadband vibration energy harvesting. In *2013 Transducers & Eurosensors XXVII: The 17th International Conference on Solid-State Sensors, Actuators and Microsystems*, pages 446–449. IEEE, 2013.
- [57] A.H. Hosseinloo and K. Turitsyn. Non-resonant energy harvesting via an adaptive bistable potential. *Smart Mater. Struct.*, 25(1):015010, 2015.
- [58] K. Aravind Kumar, S.F. Ali, and A. Arockiarajan. Piezomagnetoelastic broadband energy harvester: Nonlinear modeling and characterization. *Eur. Phys. J. Spec. Top.*, 224(14):2803–2822, 2015.
- [59] K. Ylli, D. Hoffmann, A. Willmann, P. Becker, B. Folkmer, and Y. Manoli. Energy harvesting from human motion: exploiting swing and shock excitations. *Smart Mater. Struct.*, 24(2):025029, 2015.
- [60] S.M. Jung and K.S. Yun. Energy-harvesting device with mechanical frequency-up conversion mechanism for increased power efficiency and wideband operation. *Appl. Phys. Lett.*, 96(11):111906, 2010.

- [61] M.A. Karami and D.J. Inman. Controlled buckling of piezoelectric beams for direct energy harvesting from passing vehicles. In *ASME 2012 IDETC/CIE*, pages 1231–1236. American Society of Mechanical Engineers, 2012.
- [62] R.L. Harne, C. Zhang, B. Li, and K. Wang. An analytical approach for predicting the energy capture and conversion by impulsively-excited bistable vibration energy harvesters. *J. Sound Vib.*, 373:205–222, 2016.
- [63] O. Gendelman, L.I. Manevitch, A.F. Vakakis, and R. M’closkey. Energy pumping in nonlinear mechanical oscillators: part i- dynamics of the underlying hamiltonian systems. *J. Appl. Mech.*, 68(1):34–41, 2001.
- [64] A.F. Vakakis and O. Gendelman. Energy pumping in nonlinear mechanical oscillators: part ii- resonance capture. *J. Appl. Mech.*, 68(1):42–48, 2001.
- [65] A.F. Vakakis, L.I. Manevitch, O. Gendelman, and L. Bergman. Dynamics of linear discrete systems connected to local, essentially non-linear attachments. *J. Sound Vib.*, 264(3):559–577, 2003.
- [66] F. Georgiades and A.F. Vakakis. Dynamics of a linear beam with an attached local nonlinear energy sink. *Commun. Nonlinear Sci. Numer. Simul.*, 12(5):643–651, 2007.
- [67] D. Kremer and K. Liu. A nonlinear energy sink with an energy harvester: transient responses. *J. Sound Vib.*, 333(20):4859–4880, 2014.
- [68] K. Remick, D.D. Quinn, D.M. McFarland, L. Bergman, and A. Vakakis. High-frequency vibration energy harvesting from impulsive excitation utilizing intentional dynamic instability caused by strong nonlinearity. *J. Sound Vib.*, 370:259 – 279, 2016.
- [69] K. Remick, D.D. Quinn, D.M. McFarland, L. Bergman, and A. Vakakis. High-frequency vibration energy harvesting from repeated impulsive forcing utilizing

- intentional dynamic instability caused by strong nonlinearity. *J. Intell. Mater. Syst. Struct.*, page 1045389X16649699, 2016.
- [70] L.I. Manevitch, G. Sigalov, F. Romeo, L.A. Bergman, and A.F. Vakakis. Dynamics of a linear oscillator coupled to a bistable light attachment: Analytical study. *J. Appl. Mech.*, 81(4):041011, 2013.
- [71] M.A. AL-Shudeifat. Highly efficient nonlinear energy sink. *Nonlinear Dyn.*, 76(4):1905–1920, 2014.
- [72] F. Romeo, L.I. Manevitch, L.A. Bergman, and A.F. Vakakis. Transient and chaotic low-energy transfers in a system with bistable nonlinearity. *Chaos*, 25:053109, 2015.
- [73] L. Manevitch, A. Kovaleva, and Y. Starosvetsky. Limiting phase trajectories: a new paradigm for the study of highly non-stationary processes in nonlinear physics. *arXiv preprint arXiv:1605.09264*, 2016.
- [74] N.E. Dutoit, B.L. Wardle, and S.G. Kim. Design considerations for mems-scale piezoelectric mechanical vibration energy harvesters. *Integrated Ferroelectrics*, 71(1):121–160, 2005.
- [75] D. Vatansever, E. Siores, and T. Shah. Alternative resources for renewable energy: Piezoelectric and photovoltaic smart structures. In Bharat Raj Singh, editor, *Global Warming - Impacts and Future Perspective*, chapter 10. InTech, Rijeka, 2012.
- [76] H. Vocca and F. Cottone. Kinetic energy harvesting. In G. Fagas, L. Gammaitoni, D. Paul, and G. A. Berini, editors, *ICT - Energy - Concepts Towards Zero - Power Information and Communication Technology*, chapter 03. InTech, Rijeka, 2014.

- [77] C.F. Hung, T.K. Chung, P.C. Yeh, C.C. Chen, C.M. Wang, and S.H. Lin. A miniature mechanical-piezoelectric-configured three-axis vibrational energy harvester. *IEEE Sensors J.*, 15, n.10, 2015.
- [78] S.P. Beeby, R.N. Torah, M.J. Tudor, P. Glynne-Jones, T. O'Donnell, C.R. Saha, and S. Roy. A micro electromagnetic generator for vibration energy harvesting. *J. Micromech. Microeng.*, 17:1257–1265, 2007.
- [79] I.L. Cassidy, J.T. Scruggs, and S. Behrens. Design of electromagnetic energy harvesters for large-scale structural vibration applications. In *SPIE Smart Structures and Materials+ Nondestructive Evaluation and Health Monitoring*, pages 79770P–79770P. International Society for Optics and Photonics, 2011.
- [80] S. Beeby, M. Tudor, R. Torah, S. Roberts, T. O'Donnell, and S. Roy. Experimental comparison of macro and micro scale electromagnetic vibration powered generators. *Microsystem Technologies*, Vol.13, No.12-13:1647–1653, 2007.
- [81] S.P. Beeby and T. O'Donnell. Electromagnetic energy harvesting. In *Energy Harvesting Technologies*. Springer, 2009.
- [82] W. Lacarbonara. *Nonlinear Structural Mechanics. Theory, dynamical phenomena and modeling*. Springer US, 1^a edition, 2013.
- [83] S.P. Timoshenko and J.M. Gere. *Theory of Elastic Stability*. McGraw-Hill, 2^a edition, 1961.
- [84] A.H. Nayfeh and S.A. Emam. Exact solution and stability of postbuckling configurations of beams. *Nonlinear Dyn.*, 54:395–408, 2008.
- [85] W. Kreider and A.H. Nayfeh. Experimental investigation of single-mode reponses in a fixed-fixed buckled beam. *Nonlinear Dyn.*, 15(2):155–177, 1998.

- [86] A.H. Nayfeh and W. Lacarbonara. On the discretization of distributed-parameter systems with quadratic and cubic nonlinearities. *Nonlinear Dyn.*, 13(3):203–220, 1997.
- [87] W. Lacarbonara, A.H. Nayfeh, and W. Kreider. Experimental validation of reduction methods for nonlinear vibrations of distributed-parameter systems: analysis of a buckled beam. *Nonlinear Dyn.*, 17(2):95–117, 1998.
- [88] W. Lacarbonara, A. H Nayfeh, and W. Kreider. Nonlinear response of a buckled beam to a harmonic excitation. *AIAA Paper*, (97-1276), 1997.
- [89] P.O. Mattei, R. Ponçot, M. Pachebat, and R. Côte. Nonlinear targeted energy transfer of two coupled cantilever beams coupled to a bistable light attachment. *J. Sound Vib.*, 373:29–51, 2016.
- [90] H. Wheeler. Simple inductance formulas for radio coils. *Proceedings of the Institute of Radio Engineers*, 16(2):1398–1400, 1928.
- [91] R. Gallager. *6.262 Discrete Stochastic Processes, Spring 2011*. Massachusetts Institute of Technology: MIT OpenCourseWare, <https://ocw.mit.edu>.
- [92] F. Wardle. *Ultra-precision bearings*. Woodhead Publishing, 1st edition, 2015.
- [93] K. Worden. Data processing and experiment design for the restoring force surface method, part i: integration and differentiation of measured time data. *Mech Syst Signal Process.*, 4(4):295 – 319, 1990.
- [94] S. Chiacchiari, F. Romeo, D.M. McFarland, L.A. Bergman, and A.F. Vakakis. Vibration energy harvesting from impulsive excitations via a bistable nonlinear attachment. *Int. J. Non-Linear Mech.*, 94:84–97, 2017.
- [95] E. Wahyuni and T. Ji. Relationship between static stiffness and modal stiffness of structures. *IPTEK, The Journal for Technology and Science*, 21, n.2, 2010.